REPORT DOCUMENTATION PAGE

Form Approved
OMB No. 0704-0188

PLEASE DO NOT RETURN YOUR FORM TO THE A8OVE ADDRESS.

1. REPORT DATE *(DD-MM-YYYY)*	2. REPORT TYPE	3. DATES COVERED *(From - To)*
25-03-2009	Final Technical Report	Feb 2005 - Feb 2008

4. TITLE AND SUBTITLE

Gas Transport Through Channels

5a. CONTRACT NUMBER

5b. GRANT NUMBER

N00014-05-1-0345

5c. PROGRAM ELEMENT NUM8ER

0601153N

6. AUTHOR(S)

Walter F. Boron

5d. PROJECT NUMBER

06PR00230-01

5e. TASK NUMBER

5f. WORK UNIT NUMBER

7. PERFORMING ORGANIZATION NAME(S) AND ADDRESS(ES)

Yale University School of Medicine, Department of Cellular and Molecular
333 Cedar St., P.O. Box 208026
New Haven, CT 06520-8026

8. PERFORMING ORGANIZATION REPORT NUMBER

1032095.1.K00137.704003

9. SPONSORING/MONITORING AGENCY NAME(S) AND ADDRESS(ES)

Office of Naval Research
ONR Code 342
875 North Randolph Street
Arlington, VA 22203

10. SPONSOR/MONITOR'S ACRONYM(S)

ONR

11. SPONSOR/MONITOR'S REPORT NUMBER(S)

N00014-05-1-0345

12. DISTRIBUTION/AVAILABILITY STATEMENT

Distribution Statement A/Approved for public rele

13. SUPPLEMENTARY NOTES

14. ABSTRACT

The aforementioned grant supports all work related to Gas Channels in Walter Boron's laboratory. He and his colleagues published four papers that were supported by ONR funds awarded to Yale University during the above period. For the two papers published in 2009, the work was completed at Case Western Reserve University, supported by funds for the subsequent period of support.

15. SUBJECT TERMS

Gas channels, aquaporins, Rh proteins, red blood cells, mass spectroscopy, molecular dynamics, carbon dioxide (CO2), ammonia (NH3), surface-pH measurements, Xenopus oocytes

16. SECURITY CLASSIFICATION OF:			17. LIMITATION OF ABSTRACT	18. NUMBER OF PAGES	19a. NAME OF RESPONSIBLE PERSON
a. REPORT	b. ABSTRACT	c. THIS PAGE			Joseph D. DePonte
U	U	U	UU	43	19b. TELEPHONE NUMBER *(Include area code)* 203-785-2395

The FASEB Journal • Research Communication

Evidence that aquaporin 1 is a major pathway for CO_2 transport across the human erythrocyte membrane

V. Endeward, R. Musa-Aziz,* G. J. Cooper,*,[1] L.-M. Chen,* M. F. Pelletier,* L. V. Virkki,*,[2] C. T. Supuran,[†] L. S. King,[‡] W. F. Boron,* and G. Gros[3]

Zentrum Physiologie, Abt. Vegetative Physiologie, Medizinische Hochschule Hannover, Hannover, Germany; *Department of Cellular and Molecular Physiology, Yale School of Medicine, New Haven, Connecticut, USA; [†]Dipartimento di Chimica, Laboratorio di Chimica Bioinorganica, University of Florence, Sesto Fiorentino, Firenze, Italy; and [‡]Department of Medicine, The Johns Hopkins University, Baltimore, Maryland, USA

ABSTRACT **We report here the application of a previously described method to directly determine the CO_2 permeability (P_{CO2}) of the cell membranes of normal human red blood cells (RBCs) *vs.* those deficient in aquaporin 1 (AQP1), as well as AQP1-expressing *Xenopus laevis* oocytes. This method measures the exchange of ^{18}O between CO_2, HCO_3^-, and H_2O in cell suspensions. In addition, we measure the alkaline surface pH (pH_S) transients caused by the dominant effect of entry of CO_2 *vs.* HCO_3^- into oocytes exposed to step increases in $[CO_2]$. We report that *1)* AQP1 constitutes the major pathway for molecular CO_2 in human RBCs; lack of AQP1 reduces P_{CO2} from the normal value of 0.15 ± 0.08 (SD; n=85) cm/s by 60% to 0.06 cm/s. Expression of AQP1 in oocytes increases P_{CO2} 2-fold and doubles the alkaline pH_S gradient. *2)* pCMBS, an inhibitor of the AQP1 water channel, reduces P_{CO2} of RBCs solely by action on AQP1 as it has no effect in AQP1-deficient RBCs. *3)* P_{CO2} determinations of RBCs and pH_S measurements of oocytes indicate that DIDS inhibits the CO_2 pathway of AQP1 by half. *4)* RBCs have at least one other DIDS-sensitive pathway for CO_2. We conclude that AQP1 is responsible for 60% of the high P_{CO2} of red cells and that another, so far unidentified, CO_2 pathway is present in this membrane that may account for at least 30% of total P_{CO2}.—Endeward, V., Musa-Aziz, R., Cooper, G. J., Chen, L., Pelletier, M. F., Virkki, L. V., Supuran, C. T., King, L. S., Boron, W. F., Gros, G. Evidence that aquaporin 1 is a major pathway for CO_2 transport across the human erythrocyte membrane. *FASEB J.* 20, 1974–1981 (2006)**

Key Words: human red cell membrane · CO_2 permeability · pCMBS · DIDS

ONE OF THE most widely held assumptions in biology has been that virtually all gases rapidly cross all cell membranes, and do so simply by dissolving in membrane lipids. The first major challenge to this dogma was the observation that the apical membranes of gastric gland cells have no demonstrable permeability to NH_3 or CO_2 (1). The second was the observation that the water channel aquaporin-1 (AQP1) appears to serve as a conduit for CO_2 (2–4), at least in artificial systems. The third was the finding that DIDS markedly reduces CO_2 permeability of the red blood cell (RBC) membrane (5, 6). The first evidence for the physiological relevance of gas channels was the demonstration that AQP1 plays a key role in CO_2 uptake during photosynthesis by tobacco plants (7).

To determine the CO_2 permeability of red cells and oocytes, we used a previously developed method of quantitating the CO_2 permeability of cells in suspension by the mass spectrometric ^{18}O exchange technique (8–10), which is especially suitable to detect rather high CO_2 permeabilities that are difficult to measure by stopped-flow techniques. We also developed a new technique to visualize increases in CO_2 permeation across membranes by measuring alkaline surface pH transients associated with augmented transfer of molecular CO_2 from the extra- to the intracellular space of *Xenopus laevis* oocytes. From experiments in which we compare red blood cells from normal and Colton null ($AQP1^{-/-}$) humans, we report that AQP1 appears to be responsible for 60% of the CO_2 permeability, a finding confirmed by studies of CO_2 permeability and alkaline surface pH transients in AQP1-expressing oocytes.

MATERIALS AND METHODS

Red cells

Human red cells were taken from several members of our laboratory and used for mass spectrometric experiments on the same and the following day. AQP1-deficient (Rh-positive)

[1] Present address: Department of Biomedical Science, Alfred Denny Building, University of Sheffield, Western Bank, Sheffield, South Yorkshire, S10 2TN, UK.

[2] Present address: Physiologisches Institut der Universität Zürich, Winterthurerstr. 190, CH-8057 Zürich, Switzerland.

[3] Correspondence: Zentrum Physiologie, Abt. Vegetative Physiologie, Medizinische Hochschule Hannover, 30625 Hannover, Germany. E-mail: gros.gerolf@mh-hannover.de

doi: 10.1096/fj.04-3300com

0892-6638/06/0020-1974 © FASEB

red cells were taken from two individuals with the Colton null phenotype (of only seven kindreds identified in the world) (11, 12). All red cells were washed three times in physiological saline before being used in the mass spectrometric experiments and were controlled for hemolysis. Hematocrit and blood cell count were taken to determine mean corpuscular volumes. Informed consent was sought and given in accordance with the Declaration of Helsinki. Blood samples were shipped chilled and red cells were used within 2–4 days after the samples were taken. It was ascertained by control experiment that this prolonged time interval between blood withdrawal and determination of permeability does not affect CO_2 permeability values (P_{CO2}): red cells from normal blood investigated on the day of withdrawal showed P_{CO2} of 0.16 ± 0.06 cm/s (n=35), while another group of normal red cell samples, after having traveled for several days, yielded P_{CO2} of 0.16 ± 0.07 cm/s (n=20).

Inhibitors

Most mass spectrometric experiments with intact red cells were carried out in the presence of the extracellular carbonic anhydrase (CA) sulfonamide inhibitor 1-[5-sulfamoyl-1,3,4-thiadiazol-2-yl-(aminosulfonyl-4-phenyl)]-2,4,6-trimethyl-pyridinium perchlorate, STAPTPP, described by Casey *et al.* (13), at a final concentration of $1 \cdot 10^{-5}$ M. The inhibitor was added in order to ensure inhibition of small amounts of CA that may be set free by hemolysis during the mass spectrometric experiment due to the continuous stirring of the red cell suspension. We demonstrated that the intracellular CA activity of red cells was not affected by 30 min preincubation of red cells with the same concentration of this inhibitor. Para-(chloromercuri)-benzenesulfonate, or pCMBS, is a known inhibitor of the water as well as CO_2 permeability of AQP1 (3, 12, 14). 4,4′-Diisothiocyanato-2,2′-stilbenedisulfonate (DIDS) was used as an established inhibitor of the red cell Cl^--HCO_3^- exchanger AE1 (band 3) and other ion transporters, which we have previously shown to also inhibit red cell CO_2 permeability (5).

AQP1 expression in *Xenopus laevis* oocytes

Oocyte isolation was performed according to established procedures (15). Briefly, female *Xenopus laevis* were anesthetized using 0.2% MS-222 (ethyl 3-aminobenzoate methanesulfonate; Sigma, St. Louis, MO, USA). Ovarian lobes were removed and placed in 0 Ca solution (98 mM NaCl, 2 mM KCl, 1 mM $MgCl_2$, 5 mM HEPES, pH 7.5). Enzymatic dissociation and defolliculation of oocytes were performed using 2 mg/ml type 1A collagenase (Sigma) in 0 Ca solution. Stage V-VI oocytes were selected and kept at 18°C in sterile-filtered OR3 medium containing (per 2 L) one pack of powdered Leibovitz L-15 media with L-glutamine (GIBCO-Life Technologies, Inc., Gaithersburg, MD, USA), 100 ml of 10,000 U penicillin, 10,000 U streptomycin solution (Sigma), and 5 mM HEPES, pH 7.5.

Capped cRNA was transcribed from a plasmid containing human AQP1 (kind gift from Peter Agre, Johns Hopkins University) or mouse CA II (kind gift from William S. Sly, Saint Louis University) using Message Machine kit (Ambion, Austin, TX, USA). Oocytes were injected with 50 nl 0.02 μg/μl cRNA encoding CAII or with a mixture containing cRNAs encoding CAII (0.02 μg/μl) and AQP1 (0.005 μg/μl). Experiments were performed 3–6 days after injection. Expression of AQP1 in oocytes was substantiated by determining the time from their immersion in deionized water to lysis (2). This time was >20 min in control oocytes and <1 min in AQP1-expressing oocytes. Similarly, the expression of CA was verified by determining the oocytes' CA activity by mass spectrometry, yielding an activity of ~10 U for control oocytes and of 150–200 U for CAII-expressing oocytes.

Principle of mass spectrometric measurement

We adapted the technique of Itada and Forster (16) to study the exchange of ^{18}O-labeled CO_2 and HCO_3^- between an extracellular solution and the intracellular space of cells containing CA activity, in the present study either red cells in suspension or oocytes expressing CA also suspended in fluid. Itada and Foster (16) showed that by observing the time course of the species $C^{18}O^{16}O$ (mass/charge, m/z, 46 peak height) in the suspension with a mass spectrometer, it is possible to determine the intracellular CA activity A_i and the bicarbonate permeability P_{HCO3-} of the cell membranes. The new feature of the present approach is the theoretical treatment of the process of ^{18}O exchange, which does not assume, as Itada and Forster had, that CO_2 is infinitely permeable and cannot be a limiting step in the overall exchange process (8, 10).

In normal human red cells, CO_2 permeation across the cell membrane has a detectable effect on the kinetics of ^{18}O exchange and thus it is possible to determine the membrane CO_2 permeability from measurements of ^{18}O exchange kinetics (8, 5). The set of equations describing the entire process of membrane transport of ^{18}O-labeled CO_2, HCO_3^-, and H_2O as well as the chemical reactions between them has been reported (8, 10), and is used here to estimate P_{CO2} from the kinetics of the extracellular concentration of $C^{18}O^{16}O$ in suspensions of cells. These equations were solved numerically and a fitting procedure was used to find best-fit values of membrane P_{CO2} and P_{HCO3^-}. The value of the intracellular CA activity A_i, which is required for the calculations, was determined by measuring by mass spectrometry the CA activity of red cell lysates under conditions of pH and [Cl^-] as they prevail inside cells.

Surface pH and Pf measurements in oocytes

Others (17, 18) had monitored transient changes in extracellular pH caused by the addition of CO_2/HCO^-_3 to the extracellular fluid. We monitored the surface pH (pH_S) of *Xenopus* oocytes—injected either with 50 nl of H_2O or 50 nl of a solution containing RNA (0.5 ng/nl) encoding human AQP1—using a glass microelectrode (tip diameter of ~15 μm), containing a pH-sensitive ionophore (Hydrogen Ionophore I-Cocktail B #95293, Fluka). When pH_S was relatively stable, we periodically calibrated the pH electrode by using a model MPC-200 motorized micromanipulator (Sutter Instrument Co., Novato, CA, USA) to move the tip ~300 μm away from the oocyte surface. At other times, the electrode tip pushed up against the oocyte surface ~60 μm. The pH signal was amplified by a model FD223 high-impedance electrometer (World Precision Instruments, Inc., Sarasota, FL, USA). The external reference electrode was a calomel half cell with a 3-M KCl bridge. The CO_2/HCO^-_3-free extracellular ND96 solution contained (in mM): 96 NaCl, 2 KCl, 1 $MgCl_2$, 1.8 $CaCl_2$, 5 HEPES, was titrated to pH 7.50, and had an osmolality of ~200 mosmol/kg H_2O. The CO_2/HCO^-_3 solution contained (in mM): 66 NaCl, 2 KCl, 1 $MgCl_2$, 1.8 $CaCl_2$, 5 HEPES, 33 $NaHCO_3$.

We measured water permeabilities, Pf, according to the method of Preston *et al.* (19). As described by Virkki *et al.* (20), we used a video camera to monitor the projection area of an oocyte while exposing the cell to a solution similar to CO_2/HCO^-_3-free solution, except that we reduced [NaCl] to lower the osmolality to 80 mOsm/kg. A small metal sphere next to the oocyte served as a size reference. All experiments were performed at room temperature (~22°C).

RESULTS

CO_2 permeability of the human red cell membrane

Using a large number of measurements with red cells of healthy donors, we determined a P_{CO2} of 0.15 ± 0.08 (SD) cm/s for the human red cell membrane (n=85). The median in this group of data is 0.14 cm/s. We note that the maximal P_{CO2} that can be determined with the present technique for the conditions of the human red cell is ~ 1 cm/s. The same group of 85 measurements yielded a P_{HCO3-} of $1.3 \cdot 10^{-3} \pm 0.3 \cdot 10^{-3}$ (SD) cm/s, with a median of $1.3 \cdot 10^{-3}$ cm/s.

Effect of pCMBS on CO_2 permeability

Figure 1 illustrates an experimental series studying the effects of various concentrations of pCMBS on P_{HCO3-} and P_{CO2}. pCMBS is an efficient inhibitor of the water permeability of AQP1 (14), but is also known to inhibit band 3 protein to some extent (ID_{50} for pCMBS binding to band 3 was reported to be 2.0 mM by Zhang and Solomon, ref. (21). If P_{CO2} of Colton null red cells, 0.06 cm/s (**Fig. 2**), is taken as the value to be expected with full inhibition of the AQP1 CO_2 pathway, then the data of Fig. 1 lead to an estimate of I_{50} for inhibition of this pathway of ~0.5 mM pCMBS. This is somewhat higher than the K_I estimated for inhibition of the AQP1 water pathway by pCMBS of 0.13 mM (14), but is markedly lower than the I_{50} of pCMBS for band 3. In conclusion, pCMBS inhibits the CO_2 permeability of human red cells at concentrations of ~4-fold lower than needed for inhibition of band 3 and it will be shown below that this occurs by the action of pCMBS on AQP1.

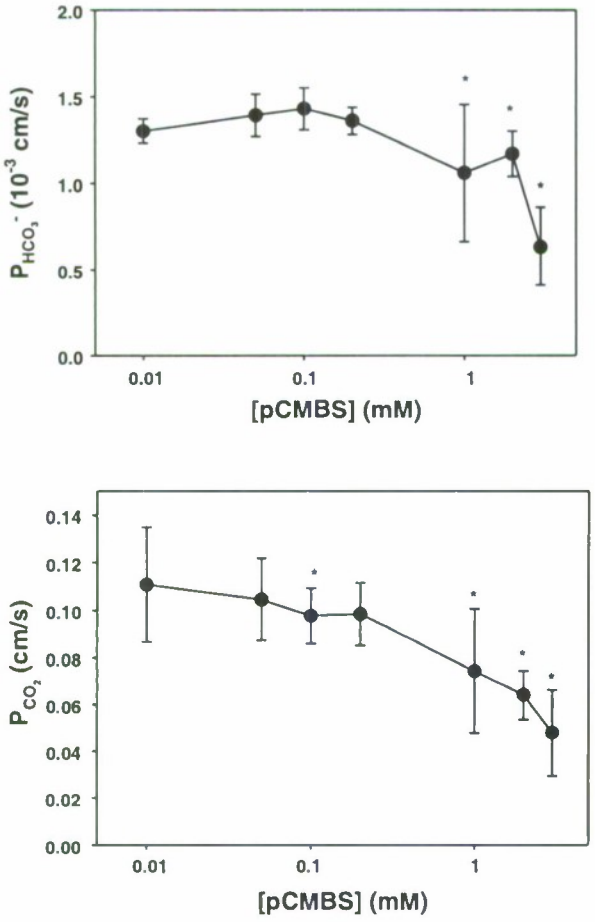

Figure 1. Semilogarithmic plot of a titration of P_{HCO3-} and P_{CO2} in human red cells by pCMBS. Intracellular CA activity in all experiments was taken to be identical to that of red cells in the absence of pCMBS. Number of experiments: 10 for control (P_{CO2}=0.12 cm/s, not shown in the graph), 3 for 0.01 mM pCMBS, 11 for 0.05 mM, 9 for 0.1 mM, 3 for 0.2 mM, 14 for 1 mM, 5 for 2 mM, and 5 for 3 mM. Bars = SD. The I_{50} of the pCMBS effect on P_{CO2} can be estimated to be ~0.5 mM. The I_{50} of the pCMBS effect on P_{HCO3-} is known from the literature to be 2 mM. *Significantly different from control value (P<0.05).

CO_2 permeability of aquaporin 1-deficient red cells

When Colton null ($AQP1^{-/-}$) red cells are compared to normal human red cells, P_{HCO3-} is identical in both types of red cells (Fig. 2*A*) but P_{CO2} is significantly (by ~60%) lower in Colton null cells than in control red cells (Fig. 2*B*), indicating that AQP1 contributes significantly to CO_2 permeation across the red cell membrane. Consistent with this, the AQP1 inhibitor pCMBS at concentrations of 1 and 2 mM has no significant effects on P_{CO2} of AQP1-deficient red cells, but it significantly reduces P_{CO2} of control cells (Fig. 2*B*). Even at the higher pCMBS concentration of 3 mM, where the inhibitory effect of pCMBS on band 3 becomes apparent by a significant reduction of P_{HCO3-} to ~1/2 both in control and Colton null red cells (Fig. 2*A*), this drug still produces no effect on P_{CO2} in Colton null red cells (Fig. 2*B*). We conclude that pCMBS at all concentrations studied is without effect on P_{CO2} of AQP1-deficient red cells, confirming that pCMBS reduces P_{CO2} solely by its action on AQP1.

We have shown that the AE1 inhibitor DIDS markedly reduces P_{CO2} as well as P_{HCO3-} in normal red cells (5). DIDS reduces P_{HCO3-} to a similar extent in Colton null and in control cells (Fig. 2*A*), as expected. On the other hand, P_{CO2}, which is reduced in Colton null cells even in the absence of DIDS, is further reduced by DIDS to ~0.012 cm/s, ~1/5th of the figure obtained in the absence of DIDS. The lowest P_{CO2} value seen in Fig. 2*B*, the value for Colton null cells treated with DIDS (0.012 cm/s), amounts to only 1/12th of the P_{CO2} found in normal red cells. In conclusion, P_{CO2} of AQP1-deficient red cells is reduced compared to control cells; it is further reduced by DIDS but is not affected by pCMBS. The inhibitory effect of DIDS lowers P_{CO2} in normal red cells by 0.10–0.11 cm/s, but lowers P_{CO2} of Colton null red cells by only 0.04–0.03 cm/s. These data suggest that part of the inhibitory effect of DIDS occurs by an action on AQP1, whereas the other part results from its action on a different DIDS-sensitive pathway.

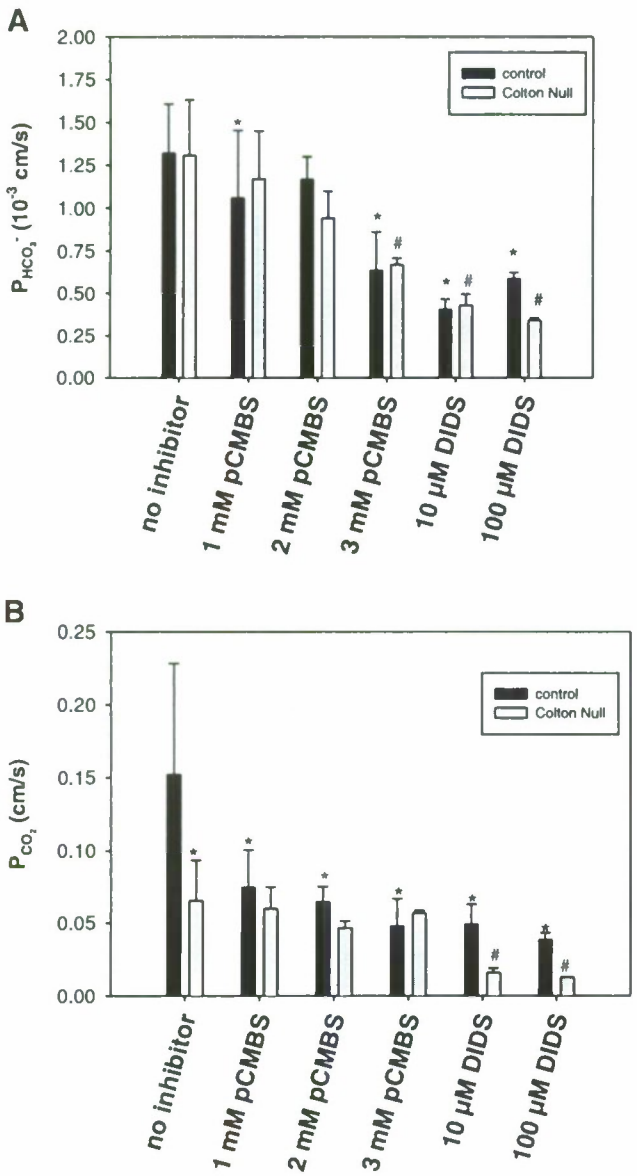

Figure 2. Comparison of the effects of DIDS and pCMBS on P_{HCO3-} and P_{CO2} of normal human red cells and on Colton null human red cells. Number of blood samples investigated was ≥ 5 for each condition; number of donors of Colton null blood was 2. It is seen that P_{CO2} is significantly reduced when aquaporin-1 is absent. DIDS reduces P_{CO2} of both normal and Colton null red cells. pCMBS reduces P_{CO2} of normal but not of Colton null red cells. *Significant differences to the leftmost black column ($P<0.05$), #Significant differences to the leftmost gray column ($P<0.05$). Error bars = SD.

Surface pH transients of AQP1-expressing oocytes and effect of DIDS

To test the hypothesis that DIDS reduces the CO_2 permeability of AQP1, we examined the effect of DIDS in oocytes either expressing human AQP1 or injected with H_2O. Preliminary experiments (not shown) indicated that 100 μM DIDS reduces the rate at which the addition of CO_2 causes intracellular pH to fall in oocytes with vitelline membrane removed. **Figure 3*A*, *B*** illustrates more sensitive experiments on oocytes (with vitelline membrane intact), in which we monitored the transient rise in extracellular surface pH caused by switching to an extracellular solution containing 5% CO_2/33 mM HCO_3^- (pH 7.50). Adding CO_2/HCO_3^- causes a rapid rise in pH_S, followed by an approximately exponential decay. This pH_S trajectory reflects the effect of CO_2 influx (less any effect of HCO_3^- influx) on the equilibrium $CO_2 + H_2O \rightleftarrows HCO_3^- + H^+$ near the cell surface. The spike height, an index of maximal CO_2 influx, was substantially less in the H_2O-injected oocyte (Fig. 3*A*) than in the AQP1-expressing oocyte (Fig. 3*B*), confirming that AQP1 increases CO_2 permeability. After removal of CO_2/HCO_3^-, we applied 100 μM DIDS and—in the continuous presence of DIDS—exposed each oocyte to CO_2/HCO_3^- a second time. DIDS had little effect on spike height in the H_2O-injected oocyte but reduced spike height in the AQP1-expressing cell.

Figure 3*C* summarizes similar paired data from a total of six experiments each on H_2O-injected and AQP1-expressing oocytes, and indicates that expression of AQP1 increases spike height by 96% and that DIDS reduces the AQP1-dependent spike height by 49%. Figure 3*D* summarizes experiments in which we found that DIDS has no effect on Pf. Thus, DIDS substantially reduces the CO_2 permeability of AQP1 without affecting H_2O permeability.

Effects of aquaporin 1 expression on CO_2 permeability of *Xenopus laevis* oocytes

Figure 4 gives the results of P_{CO2} determinations obtained with oocytes in suspension. In oocytes expressing CA II only, we measured a P_{CO2} of 0.057 cm/s, while coexpressing both CA and AQP1 raised P_{CO2} significantly to 0.11 cm/s. This agrees with the finding of Fig. 3 of a marked increase in the alkaline surface pH transient due to the expression of AQP1 in oocytes. The increase of P_{CO2} in AQP1-expressing oocytes complements the finding of a reduced P_{CO2} in aquaporin-1-deficient red cells.

DISCUSSION

The CO_2 permeability of normal human red cells

The value of 0.15 cm/s for P_{CO2} reported here may somewhat underestimate the true CO_2 permeability of the red cell membrane for two possible reasons. First, the theoretical treatment of the ^{18}O exchange process assumes perfect mixing in the intracellular space, and second, it assumes that unstirred layers around the red cells have no effect on the calculated P_{CO2}. The latter assumption is supported by our previous conclusion (10) that the present technique is highly insensitive toward unstirred layers, likely because there is a store of bicarbonate in the external solution, including the membrane surface, which can replenish CO_2 that has permeated the membrane into the cell interior. As the

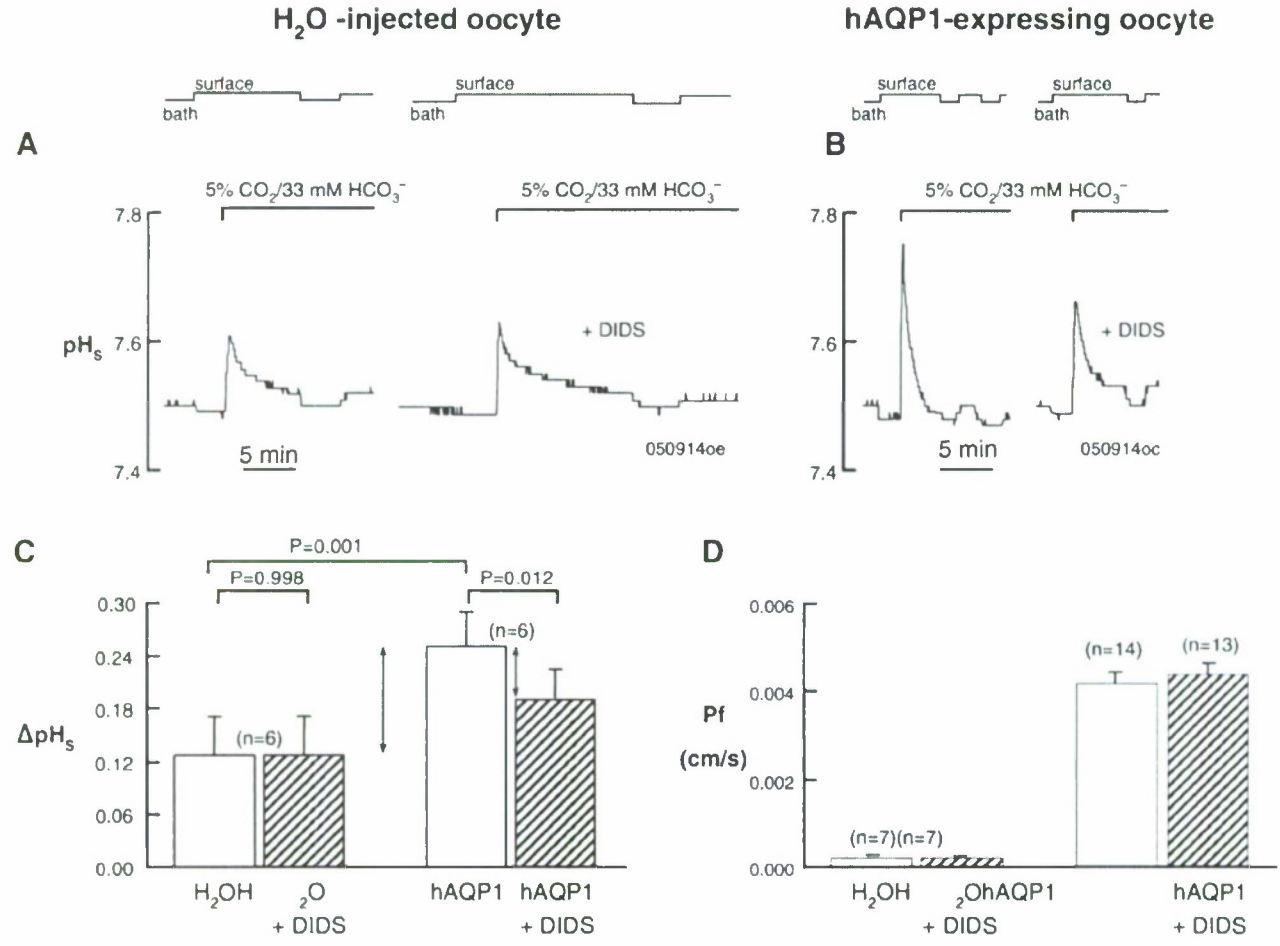

Figure 3. Surface pH and Pf measurements in *Xenopus laevis* oocytes exposed to a solution containing 5% CO_2/33 mM HCO^-_3 at pH 7.50. *A)* Time course of pH_S in a H_2O-injected oocyte. During the second pulse, 100 μM DIDS was present. The step-graph below the pH_S record indicates when the electrode was on the oocyte surface, and when it was in the bulk extracellular (pH 7.50) solution. *B)* Time course of pH_S in an AQP1-expressing oocyte. *C)* Summary of paired pH_S data. *P* values indicate the results of paired, two-tailed *t* tests. *D)* Summary of Pf data. The effect of DIDS was not significant in either H_2O-injected or AQP1-expressing oocytes. Error bars = SD.

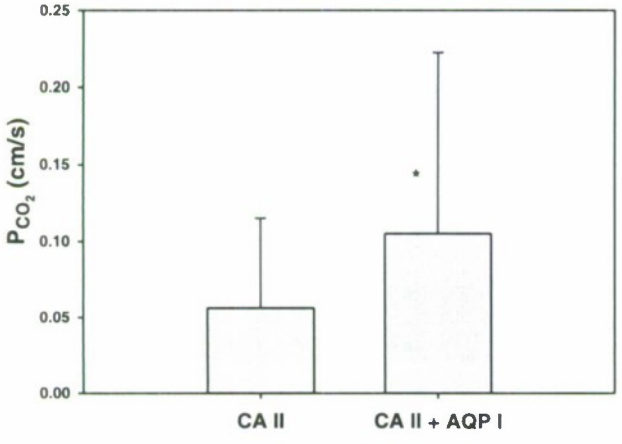

Figure 4. Effect of the expression of carbonic anhydrase II alone (CA II) and of CA II and aquaporin-1 together (CA II + AQP I) on the CO_2 permeability of *Xenopus laevis* oocytes. $n = 33$, error bar = SD, $^*P < 0.04$.

former assumption is likely not to be entirely fulfilled, the apparent P_{CO2} will tend to be an underestimate. It may be noted that from steady-state measurements of CO_2 fluxes across layers of red cells, we earlier postulated a P_{CO2} of 1–2 cm/s (22, 23).

The lipid phase of the membrane is likely to impart a "basal" CO_2 permeability to the membrane, which may be represented by the value of 0.012 cm/s observed in AQP1-deficient red cells exposed to DIDS (Fig. 2*B*). This latter value represents the lowest CO_2 permeability observed in this study and would be 30-fold lower than the CO_2 permeability of 0.3 cm/s observed by Gutknecht *et al.* (24) in artificial lipid bilayers, whose composition, however, was not representative of the lipids in the red cell membrane and which were devoid of membrane proteins. Our data indicate that AQP1 and an additional DIDS-sensitive membrane protein markedly enhance red cell P_{CO2} to the point that the resistance of the membrane for CO_2 diffusion is at least two orders of magnitude lower than that for HCO_3^-.

Bicarbonate permeabilities reported here are 1.5- to

3-fold higher than values reported in the literature, and their inhibition by DIDS appears less than has been established by other methods. This is due to some lysis that occurs by the stirring during the mass spectrometric experiment. It can be shown theoretically that the CA set free by this lysis will, before the inhibition by STAPTPP is complete, effect an apparent increase in P_{HCO3-} of up to 4-fold, but will cause an overestimation of P_{CO2} by no more than a few percent.

Aquaporin-1-mediated permeation of CO_2 across membranes

Aquaporin-1 constitutes a pathway for CO_2

The absence of AQP1 from the red cell membrane reduces CO_2 permeability from 0.15 cm/s to 0.06 cm/s (i.e., by 60%). The abundance of band 3, Glut1, the urea transporter, and spectrin are similar in AQP1-deficient and normal human red cells (12), supporting our conclusion that the decrease observed in P_{CO2} must be attributed to aquaporin-1. This conclusion is confirmed here by two other findings that were obtained by entirely different experimental approaches: *1)* the 2-fold increase in P_{CO2} of the oocyte membrane on AQP1 expression as determined by mass spectrometry, and *2)* the marked increase of the alkaline surface pH transient on AQP1-expressing oocytes. Our findings for P_{CO2} in oocytes are consistent with earlier studies examining CO_2 influx into oocytes from the time course of intracellular pH (2, 3).

There has been some controversy as to whether aquaporin-1 can act as a CO_2 pore. Yang *et al.* (25) observed the intraerythrocytic acidification on mixing of red cells with a CO_2 solution in a rapid reaction, stopped-flow spectrophotometer and obtained similar P_{CO2} values for red cells from wild-type (WT) mice (0.012 cm/s) and for red cells from AQP1-deficient mice (0.011 cm/s). Similarly, they found identical P_{CO2} values of 10^{-3} cm/s in liposomes with and without reconstitution of AQP1 using stopped-flow. They concluded that aquaporin 1 does not act as a CO_2 channel. Of note, P_{CO2} of 10^{-3} cm/s for liposomes is 100-fold lower that the value reported by Gutknecht *et al.* (24), and the P_{CO2} value observed for red cells is > 10-fold lower than the figures reported here. These differences could be due to considerable unstirred layers around the cells or, more likely, to inadequate mixing in the stopped-flow chamber that caused an apparently low CO_2 permeability; therefore, the contribution of AQP1 was not evident. Our findings are in line with those of Prasad *et al.* (4), who used stopped-flow spectrophotometry to demonstrate a CO_2 permeability in liposomes of 0.5 cm/s and in AQP1 reconstituted proteoliposomes of 1.9 cm/s, a nearly 4-fold increase that was inhibited by the aquaporin inhibitor $HgCl_2$.

pCMBS inhibits the CO_2 permeability via AQP1 only

The present data confirm previous reports that pCMBS inhibits a pathway for molecular CO_2 across aquaporin 1-expressing oocyte membranes (3) and across normal human red cell membranes (6). The data of the present paper show that in red cells this pathway is constituted by AQP1: pCMBS, an established inhibitor of the water permeability of AQP1 (14), at concentrations between 2 and 3 mM reduces P_{CO2} of normal red cells by 50–70% (Figs. 1, 2) but has no effect on P_{CO2} of Colton null red cells.

DIDS inhibits partially the CO_2 pathway via AQP1

In normal human red cells DIDS reduces P_{CO2} from 0.15 cm/s to 0.05–0.04 cm/s, producing a ΔP_{CO2} of ~0.1 cm/s, whereas in Colton null red blood cells it reduces P_{CO2} from 0.06 cm/s to 0.012 cm/s, causing a ΔP_{CO2} of ~0.05 cm/s (Fig. 2*B*). This is most simply interpreted to indicate that one-half of the DIDS effect is due to inhibition of AQP1 by DIDS, causing a ΔP_{CO2} of 0.05 cm/s, and that the other half of the DIDS effect is due to an effect other than that on AQP1. This is most clearly substantiated by the inhibitory effect of DIDS on the surface pH transient observed in aquaporin-expressing oocytes (Fig. 3).

DIDS inhibits in addition a CO_2 pathway that is not linked to AQP1

The effect of DIDS on P_{CO2} seen in AQP1-deficient red cells (Fig. 2*B*) shows clearly there is another pathway for CO_2 in the red cell membrane that *1)* is inhibitable by DIDS, *2)* is independent of AQP1, and *3)* probably is not inhibited by pCMBS. Although it cannot be excluded that this pathway is constituted by the lipid bilayer and DIDS acts in an unknown manner on its lipid phase, as speculated by Forster *et al.* (5), it should be noted that DIDS has no effect in oocytes that do not express AQP1 (Fig. 3), and thus it appears more likely that this CO_2 pathway is provided by another DIDS-inhibitable membrane protein of the red cell, such as AE1 (band 3), the Cl^--HCO_3^- exchanger. The identity of this protein has yet to be determined. From the numbers given above, its contribution may make up 32% of normal CO_2 permeability, while the basal permeability due to the membrane lipids may be responsible for 8%.

Pathway of CO_2 across the AQP1 molecule

What is the pathway in the aquaporin 1 homotetramer through which the CO_2 molecule passes? It is well established that within the AQP1 tetramer each monomer possesses a water channel. Some have proposed that, in addition, AQP1 exhibits a nonselective cation conductance mediated by the single central pore of the homotetramer (26). Each AQP1 monomer possesses a curvilinear water channel, which exhibits wide openings on the extracellular and the cytoplasmic sides, and within the membrane narrows down to a size-selective pore in the center of the bilayer. This channel is ~2.8–4 Å at its minimal diameter and has a length of

18–20 Å (27–29). Half of the channel surface is hydrophilic and the other half hydrophobic. Water with its size of 2.8 Å is thought to strip its waters of hydration via several water binding regions along the pore, thus allowing passage of a single water molecule through the pore. Ions are excluded on the basis of their charge and, in the hydrated form, their size (29). The channel does not conduct protons. The region around the 4-fold symmetry axis of the tetramer has been proposed to constitute the cation pore of aquaporin (26). It exhibits the narrowest constriction close to the external side of the pore; with an ~3 Å diameter, its interior is largely hydrophobic. It possesses a large central cavity near the membrane midpoint and has many similarities with K^+ channels (26–28). The cation channel appears to be cGMP-gated. Carbon dioxide with a MW of 44 is larger than water with its MW of 18, but has an effective molecular diameter between 2.8 and 3.4 Å, which is only slightly greater than the diameter of water of 2.8 Å (30, 31).

Because CO_2 is a linear molecule with a smaller transversal than longitudinal diameter, it may be expected to be able to permeate either of the two types of pores, each of which has a constriction site of ~3 Å. CO_2 is a quadrapole, that is, each of the two C-O bonds has a small charge separation. This may explain the observation that CO_2, which is highly soluble in water and even more soluble in nonpolar solvents such as benzene, toluene, and heptane, exhibits its highest solubility in solvents such as acetone or ethanol, which contain both hydrophobic and strongly polar groups (32). In view of these properties, it is reasonable to propose that CO_2 can transit the water channel of AQP1 with its mixed hydrophobic-hydrophilic surface. This conclusion would be in line with the observation by Cooper and Boron (3), who reported that pCMBS, though significantly reducing the rate of CO_2 uptake and intracellular acidification rate in AQP1 expressing oocytes, does not affect CO_2 permeation in the AQP1 mutant with serine replacing the mercury-sensitive cysteine (C189S) (33). Since C189 is close to the inner surface of the water channel of the AQP1 monomer (28) and inhibits the water channel when mercury binds (33), this observation suggests that CO_2 and H_2O pass through the same channel. On the other hand, the data in Fig. 3—showing that DIDS blocks half of the AQP1-dependent, CO_2-induced pH_S transient in oocytes but has no effect on water permeability—suggests that half of the CO_2 passes through AQP1's central pore and half passes through the four water pores. The absence of an effect of DIDS on water permeability in the present study is consistent with the earlier observation that DIDS does not inhibit the water permeability of red cells (34, 35).

The apparent incongruity of the pCMBS and DIDS data in oocytes could have two explanations that are not mutually exclusive. First, because the earlier intracellular pH measurements (3) are less sensitive than the current pH_S measurements, it is possible that the earlier work could not distinguish a 50% inhibition by pCMBS of CO_2 permeability from full blockade. Second, it is possible that the interaction of the large pCMBS molecule with C189 in the mouth of the water pore causes a conformational change that lowers the CO_2 permeability of the central pore. We add that, from the molecular dimensions of O_2 (effective diameter 2.3–2.9 Å; ref. 30), it is conceivable that this gas can also pass through the same channel(s), but so far this has not been tested.

Physiologieal role of the AQP1 pathway for CO_2

Recently, Uehlein *et al.* (7) have shown that aquaporin of the tobacco plant acts as a CO_2 pore and that this pore plays a physiological role in the plant's uptake of CO_2 and growth. The present work is the first demonstration of the physiological role of AQP1 as a channel for a dissolved gas in an intact animal cell. For normal individuals at rest, the O_2 and CO_2 in pulmonary capillary blood is believed to equilibrate with alveolar air within the first 200 ms of the capillary transit time of 700 ms. To estimate the role of the gas diffusion resistance of the red cell membrane, we have done a simple model calculation in which the intracellular diffusion resistance is estimated by treating the red cell as a plane sheet of 1.6 μm thickness and using the known intracellular CO_2 diffusion coefficient (22, 36); to this the inverse of the membrane permeability is added as a second diffusion resistance for CO_2. The chemical reaction inside the red cell is assumed to be infinitely fast, which allows one to describe the diffusion and reaction process by replacing the solubility α in the diffusion equation by β, a value defined as the change in total intracellular CO_2 concentration (CO_2 + HCO_3^-) per CO_2 partial pressure difference, i.e., the slope of the CO_2 binding curve of red cells (37). The time required by Cl^--HCO_3^- exchange is neglected in this model. We have calculated in this manner the time necessary for CO_2 release by a red cell to reach 95% completion ($t_{95\%}$), using the CO_2 permeabilities reported here. Because P_{CO2} values may be somewhat underestimated due to the assumption of perfect intracellular mixing in the calculations of P_{CO2}, the 95% times given in the following may be somewhat overestimated, but this does not severely affect the comparisons made. With a normal P_{CO2} of 0.15 cm/s, $t_{95\%}$ is 110 ms, and is increased to 200 ms when P_{CO2} assumes a value of 0.06 cm/s in the absence of AQP1. In view of the capillary transit time of 700 ms under resting conditions, it is not expected that AQP1 deficiency causes an impairment of CO_2 exchange in the capillary, not even with the reduced transit time that prevails during exercise. However, when the AQP1-independent, DIDS-sensitive pathway for CO_2 is also inhibited and P_{CO2} falls to 0.01 cm/s, one obtains $t_{95\%}$ = 990 ms. Thus, if both pathways for molecular CO_2 are absent and P_{CO2} assumes its "basal" value, possibly representing CO_2 diffusion across the lipids of the membrane, CO_2 release in resting individuals may be less than complete by the end of the pulmonary capillary. Under

conditions of exercise, when capillary transit time in the lung is reduced, CO_2 release may be subject to a marked diffusion limitation. FJ

We are indebted to Dr. Jean-Pierre Cartron, Paris, for providing part of the samples of Colton null blood. We thank Dr. Robert E. Forster for a large number of most helpful discussions and lucid comments. We are grateful to Ms. S. Bauer for expert technical assistance. This work was supported by DFG grant Gr 489/19.

REFERENCES

1. Waisbren, S. J., Geibel, J. P., Modlin, I. M., and Boron, W. F. (1994) Unusual permeability properties of gastric gland cells. *Nature* **368,** 332–5
2. Nakhoul, N. L., Davis B. A., Romero, M. F., and Boron, W. F. (1998) Effect of expressing the water channel aquaporin-1 on the CO_2 permeability of *Xenopus* oocytes. *Am. J. Physiol.* **274,** C543–C548
3. Cooper, G. J., and Boron, W. F. (1998) Effect of PCMBS on CO_2 permeability of *Xenopus* oocytes expressing aquaporin I or its C189S mutant. *Am. J. Physiol.* **275,** C1481–C1586
4. Prasad, G. V., Coury, L. A., Fin, F., and Zeidel, M. L. (1998) Reconstituted aquaporin I water channels transport CO_2 across membranes. *J. Biol. Chem.* **273,** 33123–33126
5. Forster, R. E., Gros, G., Lin. L., Ono, Y., and Wunder, M. (1998) The effect of 4,4′-diisothiocyanato-stilbene-2,2′-disulfonate on CO_2 permeability of the red blood cell membrane. *Proc. Natl. Acad. Sci. U. S. A.* **95,** 15815–15820
6. Blank, M. E., and Ehmke, H. (2003) Aquaporin-1 and HCO_3^--Cl^- transporter-mediated transport of CO_2 across the human erythrocyte membrane. *J. Physiol.* **550,** 419–429
7. Uehlein, N., Lovisolo, C., Seifritz, F., and Kaldenhoff, R. (2003) The tobacco aquaporin NtAQP1 is a membrane CO_2 pore with physiological functions. *Nature* **425,** 734–737
8. Wunder, M., Böllert, P., and Gros, G. (1997) Mathematical modelling of the role of intra- and extracellular activity of carbonic anhydrase and membrane permeabilities of HCO_3^-, H_2O and CO_2 in ^{18}O exchange. *Isotopes Environ. Health Stud.* **33,** 197–205
9. Wunder, M. A., and Gros, G. (1998) 18O exchange in suspensions of red blood cells: determination of parameters of mass spectrometer inlet system. *Isotopes Environ. Health Stud.* **34,** 303–310
10. Endeward, V., and Gros, G. (2005) Low carbon dioxide permeability of the apical epithelial membrane of guinea-pig colon. *J. Physiol.* **567,** 253–265
11. Preston, G. M., Smith, B. L., Zeidel, M. L., Moulds, J. J., and Agre, P. (1994) Mutations in aquaporin 1 in phenotypically normal human without functional CHIP water channels. *Science* **265,** 1585–1587
12. Mathai, J. C., Mori, S., Smith, B. L., Preston, G. M., Mohandas, N., Collins, M., van Zijl, P. C. M., Zeidel, M. L., and Agre, P. (1996) Functional analysis of aquaporin 1-deficient red cells. The Colton null phenotype. *J. Biol. Chem.* **271,** 1309–1313
13. Casey, J. R., Morgan, P. E., Vullo, D., Scozzafava, A., Mastrolorenzo, A., and Supuran, C. T. (2004) CA inhibitors. Design of selective, membrane-impermeant inhibitors targeting the human tumor-associated isozyme IX. *J. Med. Chem.* **47,** 2337–2347
14. Tsai, S.-T., Zhang, R., and Verkman, A. S. (1991) High channel-mediated water permeability in rabbit erythrocytes: characterization in native cells and expression in *Xenopus* oocytes. *Biochemistry* **30,** 2087–2092
15. Goldin, A. L. (1992) Maintenance of *Xenopus laevis* and oocyte injection. *Methods Enzymol.* **207,** 266–279
16. Itada, N., and Forster, R. E. (1977) Carbonic anhydrase activity in intact red blood cells measured with ^{18}O exchange. *J. Biol. Chem.* **252,** 3881–3890
17. De Hemptinne, A., and Huguenin, F. (1984) The influence of muscle respiration and glycolysis on surface and intracellular pH in fibres of the rat soleus. *J. Physiol.* **347,** 581–592
18. Chesler, M. (1986) Regulation of intracellular pH in reticulospinal neurones of the lamprey, Petromyzon Marinus. *J. Physiol.* **381,** 241–261
19. Preston, G. M., Carroll, T. P., Guggino, W. B., and Agre, P. (1992) Appearance of water channels in *Xenopus* oocytes expressing red cell CHIP28 protein. *Science* **256,** 385–387
20. Virkki, L.V., Franke, C., Somieski, P., and Boron, W. F. (2002) Cloning and functional characterization of a novel aquaporin from *Xenopus laevis* ooctyes. *J. Biol. Chem.* **277,** 40610–40616
21. Zhang, Z.-H., and Solomon, A. K. (1992) Effect of pCMBS on anion transport in human red cell membranes. *Biochim. Biophys. Acta* **1106,** 31–39
22. Gros, G., and Moll, W. (1971) The diffusion of carbon dioxide in erythrocytes and hemoglobin solutions. *Pfluegers Arch.* **324,** 249–266
23. Gros, G., and Bartag, I. (1979) Permeability of the red blood cell membrane for CO_2 and O_2. *Pfluegers Arch.* **382,** R21
24. Gutknecht, J., Bisson, M. A., and Tosteson, F. C. (1977) Diffusion of carbon dioxide through lipid bilayer membranes: effects of CA, bicarbonate, and unstirred layers. *J. Gen. Physiol.* **69,** 779–794
25. Yang, B., Fukuda, N., Van Hoek, A., Matthay, M. A., Ma, T., and Verkman, A. S. (2000) Carbon dioxide permeability of aquaporin-I measured in erythrocytes and lung of aquaporin-1 null mice and in reconstituted proteoliposomes. *J. Biol. Chem.* **275,** 2686–2692
26. Yool, A. J., and Weinstein, A. M. (2002) New roles for old holes: ion channel function in aquaporin-1. *News Physiol. Sci.* **17,** 68–72
27. Murata, K., Mitsuoka, K., Hirai, T., Walz, T., Agre, P., Heymann, B., Engel, A., and Fujiyoshi, Y. (2000) Structural determinants of water permeation through aquaporin-1. *Nature* **407,** 599–605
28. Ren, G., Reddy, V. S., Cheng, A., Melnyk, P., and Mitra, A. K. (2001) Visualization of a water-selective pore by electron crystallography in vitreous ice. *Proc. Natl. Acad. Sci. U. S. A.* **98,** 1398–1403
29. Sui, H., Han, B.-G., Lee, J. K., Wallan, P., and Jap, B. K. (2001) Structural basis of water-specific transport through the AQP1 water channel. *Nature* **414,** 872–878
30. Moore, W. J. (1962) *Physical Chemistry,* 3rd Ed, Prentice-Hall Inc., New York
31. Weast, R. C., ed (1977–1978) *CRC Handbook of Chemistry and Physics,* 58th Ed, CRC Press Inc., New York
32. Edsall, J. T. (1969) Carbon dioxide, carbonic acid, and bicarbonate ion: physical properties and kinetics of interconversion. In *CO_2: Chemical, Biochemical, and Physiological Aspects* (Forster, R. E., Edsall, J. T., Otis, A. B., and Roughton, F. J. W., eds) NASA SP-188
33. Jung, J. S., Preston, G. M., Smith, B. L., Guggino, W. B., and Agre, P. (1994) Molecular structure of the water channel through aquaporin CHIP. The hourglass model. *J. Biol. Chem.* **269,** 14648–14654
34. Benga, G., Pop, V. I., Popescu, O., Ionescu, M., and Mihele, V. (1983) Water exchange through erythrocyte membranes: nuclear magnetic resonance studies on the effects of inhibitors and of chemical modifications of human membranes. *J. Membr. Biol.* **76,** 129–137
35. Benga, G., Popescu, O., Pop, V. I., Hodor, P., and Borza, T. (1992) Effects on water diffusion of inhibitors affecting various transport processes in human red blood cells. *Eur. J. Cell Biol.* **59,** 219–223
36. Forster, R. E. (1964) Rate of gas uptake by red cells. In *Handbook of Physiology, Section 3. Respiration,* Vol. I (Fenn, W. O., and Rahn, H., eds) pp. 827–837, American Physiological Society, Washington, D.C.
37. Thews, G. (1960) Ein Verfahren zur Bestimmung des O_2-Diffusionskoeffizienten, der O_2-Leitfähigkeit und des O_2-Löslichkeitskoeffizienten im Gehirngewebe. *Pfluegers Arch.* **271,** 227–244

Received for publication March 13, 2006.
Accepted for publication May 15, 2006.

J Membrane Biol (2009) 228:15–31
DOI 10.1007/s00232-009-9155-7

Concentration-Dependent Effects on Intracellular and Surface pH of Exposing *Xenopus* oocytes to Solutions Containing NH_3/NH_4^+

Raif Musa-Aziz · Lihong Jiang · Li-Ming Chen · Kevin L. Behar · Walter F. Boron

Received: 24 November 2008 / Accepted: 21 January 2009 / Published online: 26 February 2009

Abstract Others have shown that exposing oocytes to high levels of NH_3/NH_4^+ (10–20 mM) causes a paradoxical fall in intracellular pH (pH_i), whereas low levels (e.g., 0.5 mM) cause little pH_i change. Here we monitored pH_i and extracellular surface pH (pH_S) while exposing oocytes to 5 or 0.5 mM NH_3/NH_4^+. We confirm that 5 mM NH_3/NH_4^+ causes a paradoxical pH_i fall ($-\Delta pH_i \cong 0.2$), but also observe an abrupt pH_S fall ($-\Delta pH_S \cong 0.2$)—indicative of NH_3 influx—followed by a slow decay. Reducing [NH_3/NH_4^+] to 0.5 mM minimizes pH_i changes but maintains pH_S changes at a reduced magnitude. Expressing AmtB (bacterial Rh homologue) exaggerates $-\Delta pH_S$ at both NH_3/NH_4^+ levels. During removal of 0.5 or 5 mM NH_3/NH_4^+, failure of pH_S to markedly overshoot bulk extracellular pH implies little NH_3 efflux and, thus, little free cytosolic NH_3/NH_4^+. A new analysis of the effects of NH_3 vs. NH_4^+ fluxes on pH_S and pH_i indicates that (a) NH_3 rather than NH_4^+ fluxes dominate pH_i and pH_S changes and (b) oocytes dispose of most incoming NH_3. NMR studies of oocytes exposed to ^{15}N-labeled NH_3/NH_4^+ show no significant formation of glutamine but substantial NH_3/NH_4^+ accumulation in what is likely an acid intracellular compartment. In conclusion, parallel measurements of pH_i and pH_S demonstrate that NH_3 flows across the plasma membrane and provide new insights into how a protein molecule in the plasma membrane—AmtB—enhances the flux of a gas across a biological membrane.

Keywords NH_3 permeability · Surface pH measurement · *Xenopus* oocytes · AmtB

R. Musa-Aziz · L.-M. Chen · W. F. Boron
Department of Cellular and Molecular Physiology, Yale University School of Medicine, New Haven, CT 06520, USA

L. Jiang
Department of Diagnostic Radiology and Magnetic Resonance Research Center, Yale University School of Medicine, New Haven, CT 06520, USA

K. L. Behar
Department of Psychiatry and Magnetic Resonance Research Center, Yale University School of Medicine, New Haven, CT 06520, USA

R. Musa-Aziz (✉) · W. F. Boron (✉)
Department of Physiology & Biophysics, Case Western Reserve University, 10900 Euclid Avenue, Cleveland, OH 44106, USA
e-mail: raif.aziz@case.edu

W. F. Boron
e-mail: walter.boron@case.edu

The movement of NH_3 across cell membranes is important for several physiological processes, including nitrogen metabolism by the liver and acid-base transport by the kidney. In 1897, Overton—monitoring the precipitation of tannins in the algae *Spirogyra*—demonstrated that it is NH_3 rather than NH_4^+ that readily crosses the cell membrane. Later, Warburg (1922), Harvey (1911), and Jacobs (1922) reached similar conclusions working on a variety of preparations and using different approaches to show that the influx of NH_3 produces a rise in internal pH (pH_i). More recently, work with pH-sensitive microelectrodes by Boron and De Weer (1976b) on squid giant axons demonstrated that, although the influx of the weak base NH_3 causes a large and rapid increase in pH_i, the lower influx of the weak acid NH_4^+ produces a slow fall in pH_i during the "plateau phase" of the NH_3/NH_4^+ exposure. Moreover, this influx of NH_4^+ during the exposure to extracellular NH_3/NH_4^+ leads to large undershoot of the original pH_i, once the NH_3/NH_4^+ is removed from the extracellular

solution. This effect is the basis of the widely used "ammonium prepulse" technique that they introduced (Boron and De Weer 1976a, 1976b).

Aickin and Thomas (1977) subsequently showed that the uptake of NH_4^+ can be so powerful in mammalian skeletal muscle that the alkalinizing effect of NH_3 entry is barely detectable. Kikeri et al. (1989) made similar observations when introducing NH_3/NH_4^+ into the lumen of the renal thick ascending limb. Waisbren et al. (1994) were the first to definitively identify a gas-impermeable membrane, showing that neither NH_3 nor NH_4^+ (nor CO_2 nor HCO_3^-) could cross the apical membranes of gastric gland cells.

In small-diameter *Xenopus* oocytes (Keicher and Meech 1994), an exposure to 20 mM extracellular NH_3/NH_4^+ produces the classic biphasic rise in pH_i, followed by a fall. However, in large-diameter oocytes (Burckhardt and Frömter 1992; Keicher and Meech 1994), an exposure to 20 mM NH_3/NH_4^+causes a paradoxical fall in pH_i and a strong positive shift in membrane potential (V_m). To explain the above effect, Burckhardt and Frömter hypothesized that NH_4^+ enters via a nonselective cation channel, dissociates to form $NH_3 + H^+$, possibly followed by sequestration of NH_3 in lipid stores. This model calls for negligible NH_3 permeability and accounts for the then-available data. Keicher and Meech found that the NH_3/NH_4^+-induced fall in pH_i requires extracellular Cl^- and proposed that the fall in pH_i is due in part to an Na/K/Cl cotransporter that carries NH_4^+ in place of K^+. However, the acidification was only slightly inhibited by Na^+ removal or by bumetanide. Moreover, Na/NH_4/Cl cotransport would not account for the positive shift in V_m, which was not abolished by Cl^- removal. Note that, in the Keicher-Meech model, the pH_i decrease would require that the NH_4^+ influx be accompanied by an NH_3 efflux, as outlined originally by Boron and De Weer, and lead to a buildup of cytosolic NH_4^+. However, if the oocytes could mediate NH_3 efflux, then NH_3/NH_4^+ removal would lead to a rapid decrease in pH_i, which is not observed. Thus, although the Keicher-Meech model has interesting features, it cannot account for all of the then-available observations.

Later, Bakouh et al. (2006) confirmed that *Xenopus* oocytes exposed to relatively high levels of NH_3/NH_4^+ (i.e., 10 mM) exhibit the fall in pH_i noted above, but also found that oocytes exposed to only 0.5 mM NH_3/NH_4^+ exhibited no change in pH_i and no substantial induced inward current (related to net entry of positive charge, namely, NH_4^+) (Bakouh et al. 2004, 2006). The above results are consistent with the hypothesis that the NH_3/NH_4^+-induced fall in pH_i and positive shift in V_m are due to a low-affinity NH_4^+-uptake mechanism that is, to some extent, Cl^- dependent and that is largely inoperative at 0.5 mM NH_3/NH_4^+.

More recently, it has become clear that the AmtB/Rh family of membrane proteins can serve as a conduit for NH_3/NH_4^+. The crystal structures of several prokaryotic family members are consistent with the idea that NH_3 passes through pores in each of the three monomers of the homotrimer (Fabiny et al. 1991; Soupene et al. 2002; Khademi et al. 2004; Zheng et al. 2004; Andrade et al. 2005; Khademi and Stroud 2006; Conroy et al. 2007). In *Xenopus* oocytes expressing RhCG, Bakouh et al. (2004, 2006) found that an exposure to 0.5 mM NH_3/NH_4^+ produced a rapid, small, and short-lived alkalinization that was followed by a slow, small, and sustained acidification. These authors proposed that the transient pH_i increase reflects the influx of NH_3, whereas the subsequent pH_i decrease reflects NH_4^+ influx in concert with NH_3 efflux—all fluxes mediated by RhCG. However, as noted in connection with the Keicher-Meech data, if RhCG could mediate NH_3 efflux—and if appreciable NH_4^+ accumulated inside the oocyte during the preceding NH_3/NH_4^+ exposure—then NH_3/NH_4^+ removal should have led to a large and rapid pH_i decrease, which was not observed.

The purpose of the present work was to elucidate the movements of NH_3 vs. NH_4^+ across the plasma membrane—and the potential role of Amt in mediating these fluxes—using the oocyte as a model system. An ancillary goal, necessary to verify our interpretation of the data, was to explore the unusual handling of NH_3/NH_4^+ by the oocyte. Our approach was to extend to NH_3 fluxes a technique that we introduced earlier to assess CO_2 fluxes across the oocyte membrane (Endeward et al. 2006; Musa-Aziz et al. 2009). In the earlier work, we pushed a blunt pH microelectrode against the oocyte membrane and found that an exposure to CO_2/HCO_3^- causes a transient rise in surface pH (pH_S). First observed in 1984 by De Hemptinne and Huguenin (1984), who worked on rat soleus muscle, this rise in pH occurs as CO_2 uptake causes the depletion of CO_2 at the cell surface, leading to the reaction $HCO_3^- + H^+ \rightarrow CO_2 + H_2O$. In 1986, Chesler (1986) found that exposing lamprey neurons to the weak base NH_3 causes a transient decrease in extracellular pH. We hypothesized that a hitherto unseen flux of NH_3 into the oocyte would deplete NH_3 at the extracellular surface. This depletion would lead to the reaction $NH_4^+ \rightarrow NH_3 + H^+$, which would lower pH_S and also partially replenish surface NH_3 (Fig. 1). We found that exposures to both 5 and 0.5 mM elicited transient pH_S decreases, and that these decreases were augmented by the expression of AmtB. The exposure to 5 mM NH_3/NH_4^+ also caused a paradoxical fall in pH_i; thus, in this case, the pH fell on both sides of the membrane. We have developed a model that allows us to predict the direction in which fluxes of NH_3 and NH_4^+ would affect pH on both sides of the membrane. Guided by this model and our new pH_S data, we conclude that (a) earlier models of how 20 mM NH_3/NH_4^+ affects oocyte pH_i are incomplete; (b) in oocytes exposed to 5 or 0.5 mM

NH_3/NH_4^+, the influx of NH_3 produces the dominant effects on pH_S (though we cannot rule out substantial NH_4^+ fluxes); (c) oocytes metabolize or sequester incoming NH_3; and (d) AmtB enhances permeability to NH_3 more than that to NH_4^+.

Methods

Expression in *Xenopus* Oocytes

cRNA Synthesis

As described elsewhere (Musa-Aziz et al. 2009), we used AmtB that we had tagged at the C terminus with EGFP (enhanced green fluorescent protein). We then used *Not*I to linearize AmtB cDNA constructs in pGH19, purified linearized cDNA using the QIAquick PCR purification kit (Qiagen Inc., Valencia, CA), transcribed capped cRNA using the T7 mMessage mMachine kit (Ambion, Austin, TX), and, finally, purified and concentrated cRNA using the RNeasy MinElute RNA Cleanup Kit (QIAGEN). We determined the RNA concentration using ultraviolet absorbance and assessed quality using gel electrophoresis.

Xenopus Oocyte Isolation

We surgically removed ovaries from anesthetized frogs, separated the oocytes using a collagenase treatment (Romero et al. 1998; Toye et al. 2006), selected Stage V–VI oocytes, and stored them until use at 18°C in OR3 medium supplemented with 500 U of penicillin and 500 U of streptomycin.

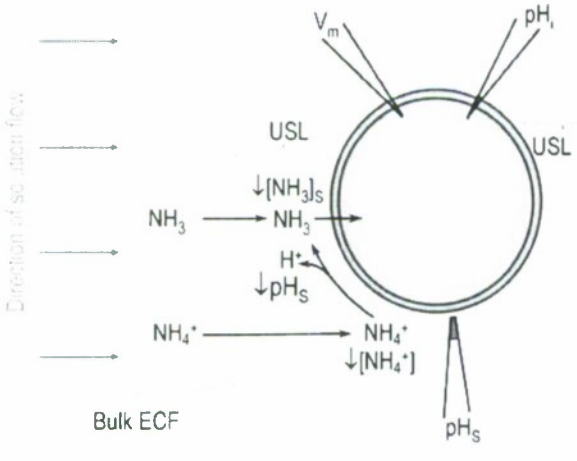

Fig. 1 Model of an oocyte exposed to NH_3/NH_4^+. The large purple arrows indicate the direction of bulk solution flow. *USL* unstirred layer; *Bulk ECF* bulk extracellular fluid

Microinjection of cRNAs

One day after isolation, we injected oocytes with either 25 ng of cRNA encoding AmtB-EGFP cRNA (50 nl of a 0.5 ng/nl cRNA solution) or 50 nl of sterile water (Ambion, Austin, TX) in the case of control ("H_2O") oocytes. We stored the oocytes 4–6 days after injection for use in experiments. We verified delivery of EGFP-tagged AmtB to a region near the plasma membrane using a 96-well plate reader (BMG Labtechnologies, Inc., Durham, NC) to assess whole-oocyte fluorescence (Toye et al. 2006).

Solutions

The nominally CO_2/HCO_3^--free ND96 solution contained (mM): 96 NaCl, 2 KCl, 1 $MgCl_2$, 1.8 $CaCl_2$, and 5 HEPES. We titrated the solution to pH 7.50 using NaOH. The osmolality of all solutions was 200 mosmol/kg H_2O. We made the solution containing 5 mM NH_3/NH_4^+ in ND96 by replacing 5 mM NaCl with 5 mM NH_4Cl. We made 0.5 mM NH_3/NH_4^+ in ND96 by diluting the 5 mM NH_3/NH_4^+ solution 1:10 with ND96 solution.

Electrophysiological Measurements

Chamber

Oocytes were placed in plastic perfusion chamber with a channel 3 mm wide × 30 mm long, and constantly superfused at a flow of 3 ml/min. Perfusing solutions were delivered from plastic syringes and Tygon tubing using syringe pumps (Harvard Apparatus, South Natick, MA). Switching between solutions was performed by pneumatically operated valves (Clippard Instrument Laboratory, Cincinnati, OH). All experiments were performed at room temperature (~22°C).

Measurement of Intracellular pH (pH_i)

Our approach was similar to that detailed previously (Toye et al. 2006; Lu et al. 2006; Parker et al. 2008). Briefly, we impaled the oocyte with two microelectrodes, one for measuring membrane potential (connected to a model 725 two-electrode oocyte voltage-clamp amplifier; Warner Instruments Corp., Hamden, CT) and the other for measuring pH_i (connected to a model FD223 high-impedance electrometer; World Precision Instruments, Sarasota, FL). Both electrodes had tip diameters of ~1 μm. The pH microelectrode was of the liquid membrane style (proton cocktail no. 95293; Fluka Chemical Corp., Ronkonkoma, NY). The analog subtraction of the V_m-electrode signal from the pH-electrode signal produced the voltage due to pH_i. We acquired and analyzed data by computer, using

software written in-house. We calibrated the pH_i/V_m in the chamber with pH standards at pH 6.0 and 8.0 (to determine the slope), followed by a single-point calibration with the standard ND96 solution (pH 7.50) in the chamber with the oocyte present, just before impalement. The mean spontaneous initial V_m in this study was -39 ± 2 mV ($n = 30$).

Measurement of Surface pH (pH_S)

The microelectrode for measuring pH_S (connected to a FD223 electrometer; World Precision Instruments) had a tip diameter of 15 μm and was of the same liquid-membrane design as the pH_i microelectrode. The external reference electrode for the V_m and pH_S measurements was a calomel half-cell (connected to a model 750 electrometer; World Precision Instruments) contacting a 3 M KCl-filled micropipette, which in turn contacted the fluid in the chamber. The analog subtraction of the calomel-electrode signal from the pH_S-electrode signal produced the signal due to pH_S. The analog subtraction of the calomel-electrode signal from the V_m-electrode signal produced the signal due to V_m. The voltage-clamp amplifier generated the virtual ground via a Ag/AgCl half cell (connected to the I_{Sense} input) contacting a second 3 M KCl-filled microelectrode, the tip of which we positioned close to the oocyte. We used an ultrafine micromanipulator (model MPC-200 system; Sutter Instrument Co., Novato, CA) to position the pH_S-electrode tip at the surface of the oocyte, and then to advance it ~40 μm further, whereupon we observed a slight dimple in the membrane. Periodically, we withdrew the electrode 300 μm from the surface of the oocyte for recalibration in the bulk extracellular fluid (pH 7.50). The fluid bathing the oocyte flowed at 3 ml/min. Relative to the flowing solution, the tip of the pH_S microelectrode was just in the "shadow" of the oocyte (Fig. 1).

Analysis of pH Data

Initial dpH_i/dt

We computed the initial rate of change of pH_i (dpH_i/dt)—produced by introducing 5 mM NH_3/NH_4^+—by determining the line of best fit to the steepest part of the pH_i vs. time record.

Maximum pH_S Spike Heights

We used the following approach to compute the maximum magnitude (i.e., "spike height" or ΔpH_S) of the pH_S transient elicited by applying 5 or 0.5 mM extracellular NH_3/NH_4^+. We determined the initial pH_S—that is, before application of NH_3/NH_4^+—by comparing the pH_S-electrode voltage signal when the electrode tip was at the oocyte surface with the voltage signal obtained when the tip was in the bulk extracellular fluid (assumed pH = 7.50). We determined the maximum pH_S during the NH_3/NH_4^+ exposure by comparing the voltage signal (at a time corresponding to the extreme pH_S value) when the electrode tip was at the oocyte surface with the voltage signal obtained a few minutes later, when the tip was in the bulk extracellular fluid (assumed pH = 7.50). The ΔpH_S was the algebraic difference between the extreme and the initial pH values, one based on a calibration in an ordinary ND96 solution and the other based on a separate calibration in the NH_3/NH_4^+-containing solution. We performed separate calibrations of the pH_S electrode in the plain and NH_3/NH_4^+-containing ND96 solutions to minimize potential errors in the event that NH_3/NH_4^+ affects the proton cocktail.

NMR Spectroscopy

Measurements of Metabolites with ^1H-[^{13}C]NMR

Twenty oocytes were incubated with 0.5 mM $^{15}NH_3/^{15}NH_4^+$, washed extensively, and homogenized with ethanol to extract water-soluble metabolites. A small quantity of [2-^{13}C]glycine (30 nmol) was added as an internal concentration reference and to control for potential sample losses during the extraction procedure. After centrifugation of the homogenate, the supernatant was lyophilized and resuspended in 10% D_2O buffer containing a small amount of 3-(trimethylsilyl)-[2,2,3,3-d_4]- propionate(Na^+) (TSP) as a chemical-shift reference. ^{1}H-[^{13}C]NMR spectra were acquired fully relaxed at 11.7 T (Patel et al. 2005), using a high-resolution Bruker Avance NMR spectrometer operating at 500.13 MHz (^{1}H) and 125.7 MHz (^{13}C). Spectral data were acquired fully relaxed with a sweep width of 6009 Hz, 8192 data points, interscan delay of 20 s, and 128 scans. Free-induction decays were zero filled, exponential filtered (LB = 0.5 Hz), and Fourier transformed. Metabolite peak intensities were measured by integration and referenced to ^{13}C-labeled glycine with correction for differences in the number of hydrogen atoms. The glycine signal was determined to be 100% enriched with ^{13}C, indicating no significant overlap with endogenous signals.

Measurements of $^{15}NH_3/^{15}NH_4^+$ with ^1H-^{15}N HSQC

Eighty oocytes were incubated with $^{15}NH_3/^{15}NH_4^+$ for 30 min, followed by extensive washing with ^{15}N-free/NH_3/NH_4^+-free buffer. The washed oocytes were cooled on ice and homogenized, yielding ~0.4 ml of supernatant after centrifugation. The medium was then acidified with 50 μl of 2.5 M HCl, 50 μl of D_2O was added for field-frequency lock, and samples were loaded into 5-mm NMR tubes.

NMR spectra were obtained at 5°C to minimize the exchange of hydrogen atoms between ammonia and water. NMR experiments were performed at 11.7 T using a high-resolution Bruker Avance NMR spectrometer operating at 500.13 MHz (^{1}H) and 50.683 MHz (^{15}N). Measurements of total $^{15}NH_3/^{15}NH_4^+$ concentrations in oocytes were determined with the Heteronuclear (^{1}H-^{15}N) Single Quantum Coherence (HSQC) NMR spectroscopy technique (Grzesiek and Bax 1993; Kanamori et al. 1995). HSQC is well suited for detection of nuclei (e.g., ^{15}N) with a low gyromagnetic ratio (γ). Because γ for ^{15}N is ~ 10 times lower than for ^{1}H, the sensitivity for ammonia-nitrogen detection is enhanced by a factor of $(\gamma_H/\gamma_N)^{5/2} \approx 306$. Water suppression was achieved using the Water Suppression by Gradient-Tailored Excitation (WATERGATE) technique (Piotto et al. 1992). ^{15}N decoupling was obtained using Waltz16 (Shaka et al. 1983). Free-induction decays were acquired with a spectral width of 6009 Hz, 8192 data points, interscan interval of 10 s, and 128 scans. All spectra were zero filled to 65,536 points. The total ammonium ($NH_3 + NH_4^+$) concentrations in oocytes were determined by comparing the integrated intensities of the ammonia ^{1}H resonance to the incubation medium containing 0.5 mM $^{15}NH_3/^{15}NH_4^+$, using the same pulse acquisition conditions, and assuming that oocytes are spheres of 1.2-mm diameter and contain 40% water by weight. ^{1}H-^{15}N HSQC spectra of oocytes and their incubation medium were acquired in a paired manner.

Statistics

We present data as mean ± SE. To compare the difference between two means, we performed a Student's *t*-test (two tails). To compare more than two means, we performed a one-way ANOVA and a Student-Newman-Keuls (SNK) multiple comparison, using KaleidaGraph (Version 4; Synergy Software). We considered $p < 0.05$ to be significant.

Results

Figure 1 summarizes how the influx of NH_3 would affect pH_S. As NH_3 enters the cell, $[NH_3]$ near the external surface of the membrane—$[NH_3]_S$—falls. The replenishment

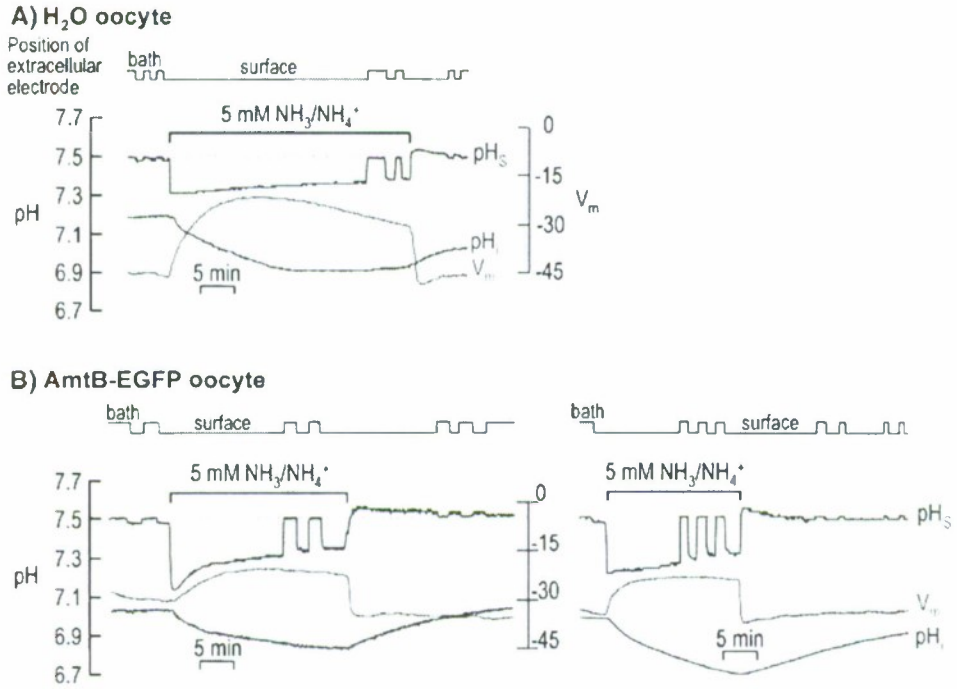

Fig. 2 Intracellular pH (pH_i) and surface (pH_S) records during application and removal of 5 mM NH_3/NH_4^+. **a** H_2O-injected oocyte. **b** AmtB EGFP-tagged expressing oocytes. At the indicated times, we switched the extracellular solution from ND96 to 5 mM NH_3/NH_4^+ and then back again. **b** shows two representative experiments: on the left, pH_S at first decays rapidly and then more slowly, whereas on the right, pH_S decays slowly throughout the NH_3/NH_4^+ exposure. In both **a** and **b**, the purple record is pH_S, the blue record is pH_i, and the brown record is V_m. The vertical gray bands represent periods during which the pH_S electrode was moved to the bulk ECF for calibration (fixed pH of 7.50). In H_2O oocytes, mean pH_i was 7.10 ± 0.04 before and 6.84 ± 0.06 during exposure to 5 mM NH_3/NH_4^+ ($n = 6$; $p = 0.005$); the comparable mean V_m values were −43 ± 2 and −25 ± 2 mV ($n = 6$; $p = 0.0002$). In AmtB oocytes, the mean pH_i was 7.14 ± 0.04 before and 6.98 ± 0.06 during exposure to 5 mM NH_3/NH_4^+ ($n = 8$; $p = 0.037$); the comparable mean V_m values were −38 ± 4 and −26 ± 2 ($n = 8$; $p = 0.010$)

of the lost NH_3 near membrane surface occurs by two routes. First, NH_3 diffuses from the bulk extracellular fluid to approach the membrane, an effect that we cannot detect. Second, NH_4^+ near the membrane dissociates to form both NH_3 as well as the H^+ that we detect as a fall in pH_S. As the concentration of NH_3 inside the cell ($[NH_3]_i$) rises, the influx of NH_3 slows, and pH_S relaxes toward the pH of the bulk extracellular fluid (pH_{Bulk}). In Fig. 1, we assume that only NH_3 enters the cell. If only NH_4^+ enters, the reverse set of events would occur and pH_S would rise. In the Discussion, we consider the situation in which both NH_3 and NH_4^+ enter.

We explored the model in Fig. 1 by exposing oocytes to 5 or 0.5 mM NH_3/NH_4^+. Figures 2 and 3 show representative experiments at these two levels of NH_3/NH_4^+, and Fig. 4 summarizes the mean values for these experiments.

Effects of 5 mM NH_3/NH_4^+

Figure 2 shows the results of representative experiments on oocytes exposed to a relatively high level of NH_3/NH_4^+, 5 mM.

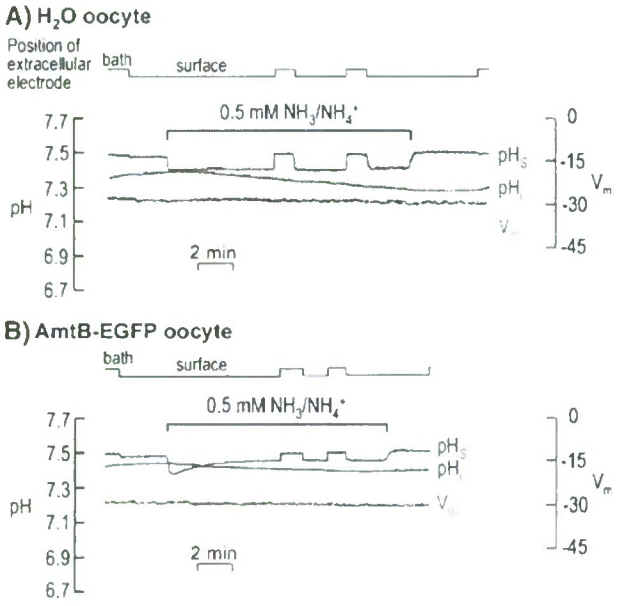

Fig. 3 Intracellular pH (pH_i) and surface (pH_S) records during application and removal of 0.5 mM NH_3/NH_4^+. **a** AmtB EGFP-tagged expressing oocyte. **b** H_2O-injected oocyte. At the indicated times, we switched the extracellular solution from ND96 to 0.5 mM NH_3/NH_4^+ and then back again. In both **a** and **b**, the purple record is pH_S, the blue record is pH_i, and the brown record is V_m. The vertical gray bands represent periods during which the pH_S electrode was moved to the bulk ECF for calibration (fixed pH of 7.50). In H_2O oocytes, the mean pH_i was 7.21 ± 0.05 before and 7.17 ± 0.05 during exposure to 0.5 mM NH_3/NH_4^+ ($n = 8$; $p = 0.61$); the comparable mean V_m values were -44 ± 2 and -40 ± 2 mV ($n = 8$; $p = 0.14$). In AmtB oocytes, the mean pH_i was 7.24 ± 0.05 before and 7.21 ± 0.05 during exposure to 0.5 mM NH_3/NH_4^+ ($n = 8$; $p = 0.52$); the comparable mean V_m values were -31 ± 4 and -30 ± 4 ($n = 8$; $p = 0.87$)

H_2O-Injected Control oocyte

Figure 2a refers to a control, H_2O-injected oocyte. Here—as previously reported by others for 20 mM NH_3/NH_4^+ (Burckhardt and Frömter 1992; Keicher and Meech 1994)—the addition of 5 mM NH_3/NH_4^+ to the extracellular fluid causes a moderately slow but sustained fall in pH_i. Simultaneously, pH_S abruptly falls by ~ 0.2 and then slowly decays (i.e., rises toward pH_{Bulk}). The initial fall in pH_S indicates that the influx of NH_3 (as opposed to NH_4^+) is dominant with respect to effects on pH_S. Note that, at a time when pH_i has reached a stable value, pH_S is still substantially lower than pH_{Bulk}, indicating that NH_3 is still entering the cell. Applying 5 mM NH_3/NH_4^+also causes a very slowly developing depolarization that reaches a peak after nearly 15 min—not the instantaneous depolarization expected of a pre-existing NH_4^+ channel—that slowly decays by nearly 9 mV.

The removal of the NH_3/NH_4^+ leads to a slow recovery of pH_i that is incomplete over the time frame of this experiment. The removal of NH_3/NH_4^+ causes pH_S to overshoot pH_{Bulk} by a small amount (0.048 ± 0.004; $n = 5$), and then to decay slowly. The presence of an overshoot implies that—regarding effects on pH_S—a small efflux of NH_3 dominates over any efflux of NH_4^+. This exiting NH_3 presumably arises from a small amount of intracellular NH_4^+ that dissociated to form H^+ (which would lower pH_i) and NH_3 (which would exit the cell). The short duration of the overshoot implies that the efflux was of short duration (i.e., that the pool of intracellular NH_4^+ was small). If intracellular NH_4^+ had accumulated to a substantial degree during the NH_3/NH_4^+exposure, then the removal of NH_3/NH_4^+ should have led to an abrupt fall in pH_i (which we did not observe) and a pH_S overshoot whose magnitude should have matched that of the initial NH_3/NH_4^+-induced fall in pH_S (i.e., ~ 0.2). Removing NH_3/NH_4^+ also causes V_m to undershoot its initial level by ~ 1 mV and then to relax to the pre-NH_3/NH_4^+ value. Note that the speed of the repolarization during NH_3/NH_4^+ removal is much faster than the depolarization during NH_3/NH_4^+ application, but still slower than the speed of the pH_S increase during NH_3/NH_4^+ removal.

Oocyte Expressing AmtB Tagged with EGFP

Figure 2b shows two experiments on oocytes expressing AmtB-EGFP. At the left, the switch to 5 mM NH_3/NH_4^+ causes a fall in pH_i, though one that is slower than for the H_2O oocyte. On the other hand, the maximal fall in surface pH (which we refer to as $-\Delta pH_S$) is substantially larger for the AmtB-EGFP oocyte than for the H_2O-injected oocyte, implying that the relative uptake of NH_3 over NH_4^+ is higher in the AmtB oocyte. In the oocyte at the left in

Fig. 2b, this shift in pH_S at first decays rapidly and then more slowly. In the oocyte at the right in Fig. 2b, the fall in pH_S decays very slowly throughout the NH_3/NH_4^+ exposure. In both AmtB oocytes—as was true for the H_2O oocyte—pH_S fails to decay fully to pH_{Bulk} during the NH_3/NH_4^+ exposure. The V_m changes induced by application and removal of NH_3/NH_4^+ are similar to, but smaller than, those for H_2O oocytes.

The removal of NH_3/NH_4^+ produces about the same effects in the AmtB oocyte as in the H_2O oocyte (mean overshoot in AmtB oocytes, 0.037 ± 0.004; $n = 6$).

Summary of AmtB-EGFP Versus H_2O

As summarized on the left side in Fig. 4 for a larger number of experiments, the effect of AmtB vs. H_2O is statistically significant for the initial rate of pH_i decrease (dpH_i/dt) elicited by NH_3/NH_4^+ (Fig. 4a). The slower fall of pH_i in the case of AmtB oocytes is consistent with the hypothesis that, regarding effects on pH_i (a) AmtB acts by predominantly enhancing NH_3 vs. NH_4^+ influx (b) the enhanced influx of NH_3 to some extent promotes the reaction $NH_3 + H^+ \rightarrow NH_4^+$ in the cytosol, and (c) the consumption of cytosolic H^+ slows the NH_3/NH_4^+-induced fall in pH_i.

The effect of expressing AmtB did not reach statistical significance regarding the NH_3/NH_4^+-induced ΔpH_i (Fig. 4b). However, AmtB oocytes had a greater $-\Delta pH_S$ (Fig. 4c), indicating a greater relative influx of NH_3 and thus supporting the hypothesis in the previous paragraph. Finally, the AmtB oocytes had a smaller ΔV_m (Fig. 4d).

Effects of 0.5 mM NH_3/NH_4^+

Figure 3 shows representative data from a pair of oocytes exposed to a relatively low level of NH_3/NH_4^+, 0.5 mM.

H_2O-Injected Control Oocyte

As shown in Fig. 3a for a H_2O-injected oocyte, the switch to 0.5 mM NH_3/NH_4^+ causes a slow and very slight fall in pH_i. Although pH_S abruptly falls, $-\Delta pH_S$ is substantially lower than for H_2O oocytes exposed to the much higher level of NH_3/NH_4^+ (i.e., 5 mM; see Fig. 2a). Nevertheless, regarding effects on pH_S, the effect of NH_3 influx (over NH_4^+ influx) is clearly dominant. The V_m changes caused by application and removal of 0.5 mM NH_3/NH_4^+ are much smaller than those in the experiments with 5 mM NH_3/NH_4^+.

The removal of NH_3/NH_4^+ evoked virtually no recovery of pH_i in Fig. 3a, although some oocytes exhibited a slight pH_i recovery. In Fig. 3a, pH_S rose to a value ~ 0.02 higher than pH_{Bulk}. The mean pH_S overshoot was 0.006 ± 0.003

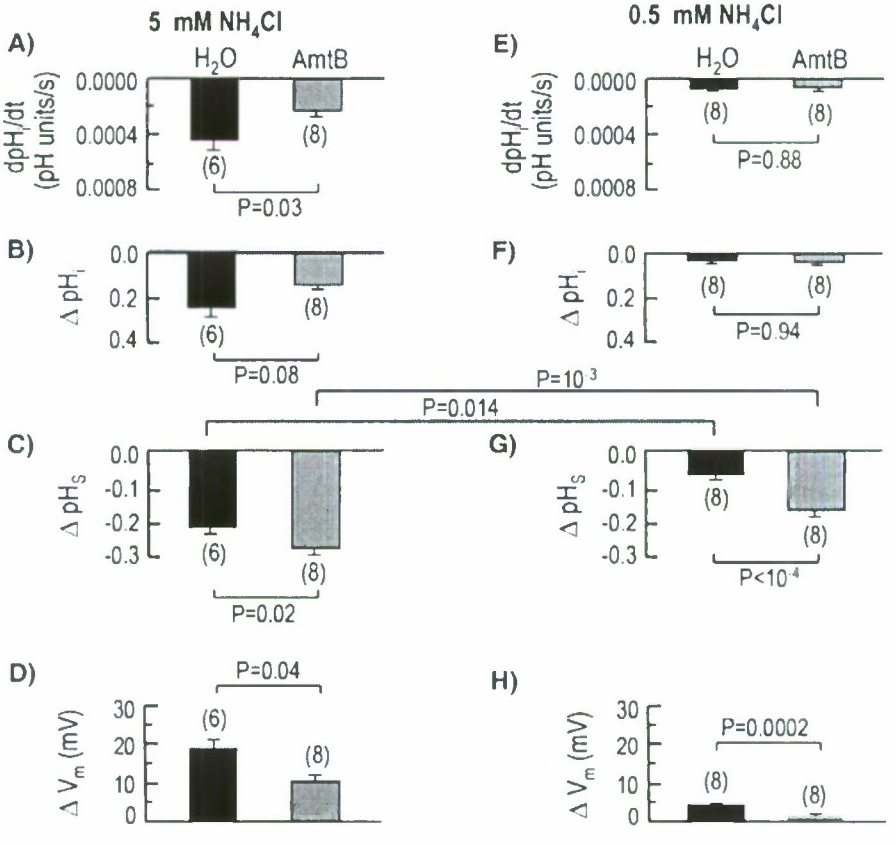

Fig. 4 Summary of the mean initial rate of pH_i decrease (dpH_i/dt) and magnitude of the NH_3-induced change in steady-state pH_i (ΔpH_i), ΔpH_S, and V_m for larger groups of experiments like those in Figs. 2 and 3

($n = 8$; 0.006 vs. 0; $p = 0.28$). These data indicate that—regarding effects on pH_S—the efflux of NH_3 is negligible relative to that of NH_4^+.

Oocyte Expressing AmtB Tagged with EGFP

Figure 3b shows that, with an oocyte expressing AmtB-EGFP, the switch to 0.5 mM NH_3/NH_4^+ causes little change in pH_i. The maximal fall in pH_S is much larger for the AmtB-EGFP oocyte than for the H_2O oocyte, though both values are much smaller than for their counterparts in exposures to 5 mM NH_3/NH_4^+. The V_m change is minimal.

The removal of NH_3/NH_4^+ from AmtB-EGFP oocytes (Fig. 3b) evoked virtually the same response as in H_2O oocytes. The mean pH_S overshoot was 0.014 ± 0.006 ($n = 8$; 0.014 vs. 0; $p = 0.30$), indicating that—regarding effects on pH_S—the efflux of NH_3 is negligible relative to that of NH_4^+.

Summary of AmtB-EGFP Versus H_2O

As summarized on the right side in Fig. 4, the effect of AmtB vs. H_2O for an exposure to 0.5 mM NH_3/NH_4^+ follows essentially the same pattern as for an exposure to 5 mM, except that the difference for AmtB vs. H_2O is not statistically significant for dpH_i/dt (Fig. 4e). The dpH_i/dt for H_2O oocytes is significantly different from zero ($p = 0.05$) but not for AmtB oocytes ($p = 0.26$). As summarized in Fig. 4f, the ΔpH_i was not different from zero for H_2O oocytes (0.038 ± 0.010; $n = 8$; $p = 0.15$) but was significantly—but not substantially different—for AmtB oocytes (0.040 ± 0.005; $n = 8$; $p = 0.01$). As was the case for the exposures to 5 mM NH_3/NH_4^+, the AmtB oocytes also had a higher $-\Delta pH_S$ (Fig. 4g), indicating a greater relative NH_3 influx. As also was the case for the 5 mM exposures, the ΔV_m was lower for the AmtB oocytes (Fig. 4h).

Comparing ΔpH_S data for 5 mM vs. 0.5 mM (Fig. 4c vs. g), we see that the difference (always higher for the experiments with 5 mM NH_3/NH_4^+) is statistically significant both for H_2O oocytes and for AmtB oocytes.

NMR Studies of Oocytes Exposed to ^{15}N-Labeled 0.5 mM NH_3/NH_4^+

A paradox in our results is that AmtB increases $-\Delta pH_S$ (Fig. 4g)—indicating that AmtB enhances the influx of NH_3—and yet has no significant effect on the initial dpH_i/dt (Fig. 4e) or ΔpH_i (Fig. 4f). Moreover, removing extracellular 0.5 mM NH_3/NH_4^+ produces little pH_S overshoot beyond pH_{Bulk} (Fig. 3a, b), indicating little efflux of NH_3. The most straightforward explanation for these data is that the oocyte somehow disposes of most incoming NH_3 by either metabolizing it to a neutral product or sequestering it. We test this hypothesis in the next two sections. Note that, a priori, we can rule out the possibility that the oocyte metabolizes or sequesters NH_4^+ (as opposed to NH_3). If the oocyte first converted the entering NH_3 to NH_4^+ ($NH_3 + H^+ \rightarrow NH_4^+$) and then metabolized that NH_4^+ to a neutral product(s), the result would be an increase in pH_i, which we would have easily observed in experiments with 0.5 mM NH_3/NH_4^+.

Assessment of Glutamine Formation

The leading candidate for the metabolism of NH_3 to a neutral product would be the conversion of glutamate to glutamine via glutamine synthetase: $Glu^- + MgATP^= + NH_3 \rightarrow Gln + MgADP^- + H_2PO_4^-$.

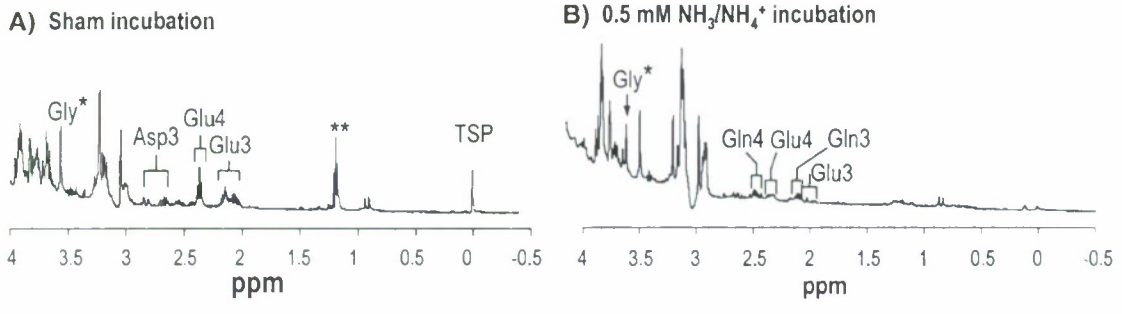

Fig. 5 ^1H-NMR spectra of ethanol extracts of oocytes. **a** Sham incubation (i.e., oocytes not exposed to NH_3/NH_4^+). **b** Oocytes incubated with 0.5 mM $^{15}NH_3/^{15}NH_4^+$ for 10 min. Each spectrum represents the extract of 20 oocytes. TSP, 3-trimethylsilyl-[2,2,3,3-d_4]-propionate(Na^+), was added as a chemical-shift reference (0.0 ppm). *Glycine was added during oocyte extraction to serve as an internal concentration standard and to control for potential metabolite losses. **Residual ethanol contaminant remaining after extraction. Estimated concentrations of metabolites in control noninjected oocytes not exposed to NH_3/NH_4^+. (A) Glutamate (Glu): 6.48 mM. Estimated metabolite concentrations after incubation with $^{15}NH_3/^{15}NH_4^+$ for 10 min: Glu: H_2O, 1.69 mM. Glutamine (Gln): 1.1 mM. Glu and Gln methylene protons (H_4 and H_3) and lactate methyl protons (H_3) are depicted. Glu H_4 and H_3 were observed in control noninjected oocytes incubated with $^{15}NH_3/^{15}NH_4^+$

To test this hypothesis, we incubated noninjected oocytes for 10 min either in ND96 alone (for sham incubation) or in ND96 plus 0.5 mM $^{15}NH_3/^{15}NH_4^+$. We then homogenized the oocytes with ethanol to extract water-soluble metabolites and subjected the extract to ^1H-[^{13}C] NMR spectroscopy (Fig. 5). The extract from oocytes incubated in $^{15}NH_3/^{15}NH_4^+$ exhibited a very low Gln signal ([Gln] $\cong$ 1.1 mM) vs. the shams (undetectable Gln). RhAG, a component of the erythrocyte Rh complex, has a higher NH_3/CO_2 permeability ratio than AmtB (Endeward et al. 2006; Musa-Aziz et al. 2009), and RhAG-expressing oocytes (like AmtB oocytes) exhibit high ΔpH_S values and very small pH_i changes when exposed to 0.5 mM NH_3/NH_4^+. However, extracts from RhAG oocytes exposed to 0.5 mM $^{15}NH_3/^{15}NH_4^+$ have undetectable Gln (not shown).

^1H-^{15}N-HSQC spectra (acquired as in Fig. 6 from a separate batch of RhAG oocytes incubated with 0.5 mM $^{15}NH_4Cl$) showed no significant ^{15}N-enrichment of amides in the metabolites, although we only examined Gln and a few other likely metabolites. Although we cannot rule out the possibility that oocytes sequester NH_3 via unknown metabolic pathways, our ^1H-[^{13}C]NMR and ^1H-^{15}N-HSQC data rule out substantial conversion of NH_3 to Gln and provide no evidence for other pathways.

NH_3/NH_4^+ *Accumulation in Oocyte Water*

To determine if oocytes accumulate NH_3/NH_4^+ per se, we incubated noninjected control oocytes or AmtB oocytes in ND96 containing 0.5 mM $^{15}NH_3/^{15}NH_4^+$ for 30 min. After the incubation, we washed the oocytes with a NH_3-free ND96 solution and, following homogenization and centrifugation, measured the total $^{15}NH_3 + ^{15}NH_4^+$ of the supernatant using ^1H-^{15}N HSQC (Fig. 6a, b). We found that $^{15}NH_3/^{15}NH_4^+$—which reflects only NH_3/NH_4^+ taken up during the incubation—was ~30% higher in AmtB oocytes (4.15 mM computed for total oocyte H_2O) than in control noninjected oocytes (3.33 mM). Because pH_i was ~7.40 in these experiments—and pH_o was 7.50 and $[NH_3/NH_4^+]_o$ was 0.5 mM—we can conclude that if NH_3 fully equilibrated across the cell membrane, cytosolic $[NH_3/NH_4^+]$ (i.e., the concentration in the water in direct contact with the inner surface of the plasma membrane) could only have been 0.5 mM $\times$ $10^{(7.50-7.40)}$ $\cong$ 0.6 mM. Note that even this

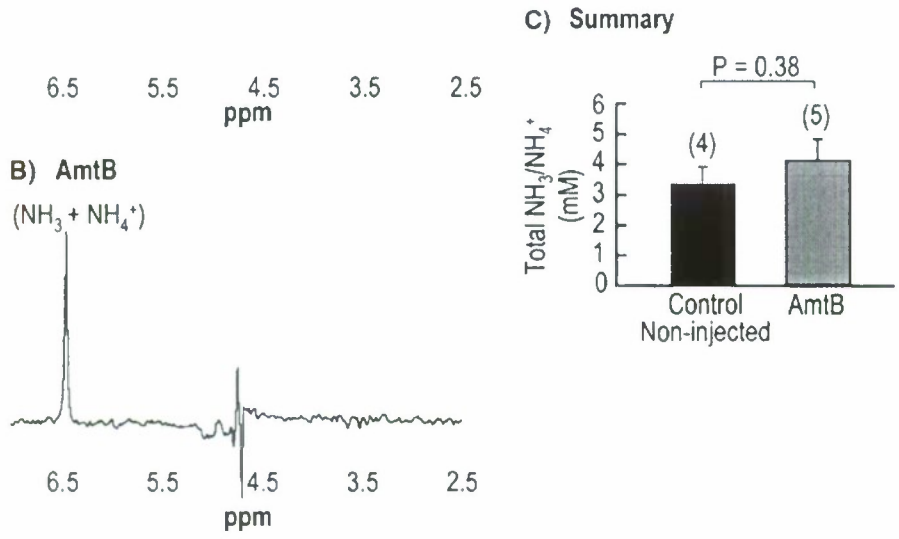

Fig. 6 Representative ^1H-^{15}N HSQC spectra of *Xenopus* oocytes incubated with $^{15}NH_3/^{15}NH_4^+$. **a** Control noninjected oocytes. **b** AmtB oocytes. Total ammonia appears as a single resonance at ~6.5 ppm (relative to water, assigned to 4.7 ppm). Spectral intensities were scaled relative to the intensity of 0.5 mM ^{15}N-ammonia in the incubation medium of each sample acquired with the same pulse parameter settings. The residual water signal artifact appears at 4.7 ppm. **c** Total ammonia ($NH_3 + NH_4^+$) concentration in control noninjected and in AmtB oocytes. Values are mean ± SE, with numbers of oocyte samples for each group in parentheses. The statistical comparisons were made using unpaired two-tailed *t*-tests. The experimental error was large due to fast evaporation of the ammonia in both the standard solution and the extracts

level of cytosolic NH_3/NH_4^+ would have led—upon the removal of extracellular NH_3/NH_4^+—to a substantial fall in pH_i and a large transient overshoot of pH_S, neither of which we observed. Thus, we conclude that cytosolic $[NH_3/NH_4^+]$ must have been substantially lower than 0.6 mM. The most straightforward explanation for the extremely high level of intracellular NH_3/NH_4^+ that we actually observed in the NMR experiments (i.e., for the $3^+ - 4^+$ mM) is that the vast majority of intracellular NH_3/NH_4^+ was, in fact, confined to an acidic intracellular compartment.

Discussion

Overview

The pH_i data in the present paper confirm the earlier observation that an exposure of a control *Xenopus* oocyte (i.e., not heterologously expressing other proteins) to a relatively high level of NH_3/NH_4^+ leads to a paradoxical intracellular acidification (Burckhardt and Frömter 1992; Keicher and Meech 1994). Earlier investigators had also found that an exposure to a relatively low level of NH_3/NH_4^+ leads to a negligible pH_i change (Bakouh et al. 2004). We now confirm both observations in H_2O oocytes (Fig. 4b and f, respectively). In addition, we make the novel observation that the expression of AmtB slows the pH_i fall elicited by an exposure to 5 mM NH_3/NH_4^+ (Fig. 4a), consistent with the hypothesis that AmtB predominantly promotes the influx of NH_3 over NH_4^+ (regarding effects on pH_i). However, we believe that the most important contributions of the present study are (a) the simultaneous application of pH_S and pH_i measurements, which provide new insights into how *Xenopus* oocytes handle exposures to NH_3/NH_4^+, and (b) novel pH_S data that show that AmtB enhances NH_3 fluxes during exposures to both 5 mM and 0.5 mM NH_3/NH_4^+.

Evidence for Unusual NH_3/NH_4^+ Handling by *Xenopus* Oocytes

Regardless of whether the concentration is 5 or 0.5 mM, exposing an oocyte to NH_3/NH_4^+ causes an initial pH_S decrease, the explanation for which is straightforward: the influx of NH_3 causes a depletion of NH_3 at the extracellular surface of the oocyte, leading to the reaction $NH_4^+ \rightarrow NH_3 + H^+$. However, five other observations indicate that the handling of NH_3 by *Xenopus* oocytes is unusual compared to that by other cells studied thus far.

First, when one exposes an oocyte to a relatively high level of NH_3/NH_4^+, pH_i paradoxically falls. Almost all other cells—the exceptions being membranes that mediate either a massive influx of NH_4^+ (Aickin and Thomas 1977; Kikeri et al. 1989) or no apparent flux of either NH_3 or NH_4^+ (Waisbren et al. 1994; Singh et al. 1995)—exhibit a rapid pH_i increase, due to the influx and protonation of NH_3 (Roos and Boron 1981). Working on oocytes, previous investigators had observed NH_3/NH_4^+-induced pH_i decreases when introducing 10–20 mM NH_3/NH_4^+ (Burckhardt and Frömter 1992; Keicher and Meech 1994; Bakouh et al. 2006). In the present paper, we observed similar, though smaller pH_i decreases—with both H_2O-injected controls and AmtB oocytes—when introducing 5 mM NH_3/NH_4^+ (Fig. 2). This paradoxical fall in pH_i implies that the rate of intracellular acid loading is higher than that of acid extrusion. We examine potential explanations below, under "Models of NH_3/NH_4^+ Handling by *Xenopus* Oocytes: 'High' $[NH_3/NH_4^+]_o$."

Second, when one exposes an oocyte to a relatively low level (e.g., 0.5 mM) of NH_3/NH_4^+, pH_i either falls very slowly, and by a small amount (Figs. 3, 4e, f; H_2O bars), or does not change significantly (Fig. 4e, f; AmtB bars). These observations on H_2O oocytes confirm earlier work (Bakouh et al. 2004, 2006).

Third, after an exposure to relatively high levels of NH_3/NH_4^+—10 to 20 mM in the case of others (Burckhardt and Frömter 1992; Keicher and Meech 1994; Bakouh et al. 2004, 2006) or 5 mM in the present work (Fig. 2)—the removal of extracellular NH_3/NH_4^+ causes pH_i to increase slowly, rather than to decrease rapidly (due to NH_3 efflux followed by the intracellular reaction $NH_4^+ \rightarrow NH_3 + H^+$), as has been observed by numerous investigators working on most other cell types.

Fourth, although introducing NH_3/NH_4^+ produces an abrupt fall in pH_S—indicative of NH_3 influx—the subsequent decay in pH_S is generally very slow, regardless of whether the oocytes are exposed to 5 or 0.5 mM NH_3/NH_4^+. In H_2O-injected oocytes (Figs. 2a, 3a), the decay is monotonic and extremely slow throughout. In AmtB oocytes, the decay in pH_S is sometimes fast at first, but then extremely slow (see Fig. 2b, left, and Fig. 3b). In some other experiments on AmtB oocytes, even this rapid phase of pH_S decay is absent (Fig. 2b, right). In neither case does pH_S return to the pH_{Bulk} value of 7.50 during the course of an NH_3/NH_4^+ exposure lasting ~15 min or more. Thus, the decay in pH_S in these experiments with NH_3 is decidedly slower than the rapid decay in pH_S in oocytes exposed to CO_2 (Endeward et al. 2006)—a decay that is complete in ~5 min. These observations are consistent with the hypothesis that—unlike CO_2 (which equilibrates across the membrane in a few minutes)—NH_3 is still far from equilibrated across the plasma membrane and continues to enter the oocyte for a prolonged period (Figs. 2, 3). A corollary is that the oocyte somehow maintains a relatively low level of NH_3 near the inner surface of the cell membrane.

Fifth, although one would expect that removing extracellular NH_3/NH_4^+ would cause pH_S to increase abruptly

and overshoot the initial pH_S (i.e., near the pH_{Bulk} of 7.50)—by an amount that approximates the magnitude of the pH_S decay during the preceding NH_3/NH_4^+ exposure—in fact we observe little or no pH_S overshoot (Figs. 2, 3). Moreover, the expression of AmtB (vs. the injection of H_2O) increases the magnitudes of the rapid pH_S changes but does not produce a larger overshoot. These results imply that the NH_3 efflux from the oocyte is small, consistent with the hypothesis that (1) the pathways for NH_3 movement across the oocyte membrane are highly rectified (i.e., favoring influx over efflux), or (2) very little NH_4^+ is present in the cytosol near the plasma membrane at the end of an NH_3/NH_4^+ exposure. Thus, upon removal of extracellular NH_3/NH_4^+, very little free, cytosolic NH_4^+ is available for the reaction $NH_4^+ \rightarrow H^+ + NH_3$. This reaction is necessary not only for the pH_i to fall, but also to generate the NH_3 that subsequently exits and produces the pH_S overshoot. Moreover, a limited cytosolic NH_4^+ would minimize the outwardly directed diffusion potential for NH_4^+, and minimize a rebound hyperpolarization upon removal of extracellular NH_3/NH_4^+. Because we know of no examples of a rectifying of a gas flux through either lipid or a protein channel, option 2 is the simplest explanation, and would account for the observations that removal of extracellular NH_3/NH_4^+ fails to cause (a) a fall in oocyte pH_i (b) a large pH_S overshoot, and (c) a rebound hyperpolarization. Instead, NH_3/NH_4^+ removal merely eliminates the processes that cause pH_S to fall and V_m to become more positive, causing these parameters simply to return to their pre-NH_3/NH_4^+ values.

Models of NH_3/NH_4^+ Handling by *Xenopus* Oocytes: "Low" $[NH_3/NH_4^+]_o$

In the section following this one, we consider potential explanations for the pH_i and pH_S data obtained with the exposure to and withdrawal of relatively high NH_3/NH_4^+ levels (e.g., 5 mM), with their attendant large and paradoxical pH_i changes. In this section, we examine experiments with relatively low NH_3/NH_4^+ levels (e.g., 0.5 mM), where the paradoxical pH_i changes—mediated by a process with a low affinity for NH_3 and/or NH_4^+—are minimal. We consider five models of NH_3 handling by *Xenopus* oocytes (Fig. 7) that could account for why an exposure to NH_3/NH_4^+ would cause virtually no change in pH_i.

Model A: Is the pH_i Effect of NH_3 Influx Perfectly Matched by the pH_i Effect of NH_4^+ Influx (Fig. 7a)?

In order for the influxes of NH_3 and NH_4^+ to cause no change in pH_i, the influx of NH_3 (J_{NH_3}) and the influx of NH_4^+ ($J_{NH_4^+}$) would have to be in the ratio $10^{(pH_i - pK_a)}$, where pH_i is the initial pH_i and pK_a refers to the intracellular equilibrium $NH_4^+ \rightleftarrows NH_3 + H^+$. To make this point more clearly, we imagine that the oocyte's cytosol contains a tiny amount of NH_3/NH_4^+ that is equilibrated at the initial pH_i. If we assume that the pK_a of this reaction is 9.2, and, for the sake of simplicity, that the pH_i is 7.2, then

$$\frac{[NH_3]_i}{[NH_4^+]_i} = 10^{pH_i - pK_a} = 10^{7.2-9.2} = \frac{1}{100} \quad (1)$$

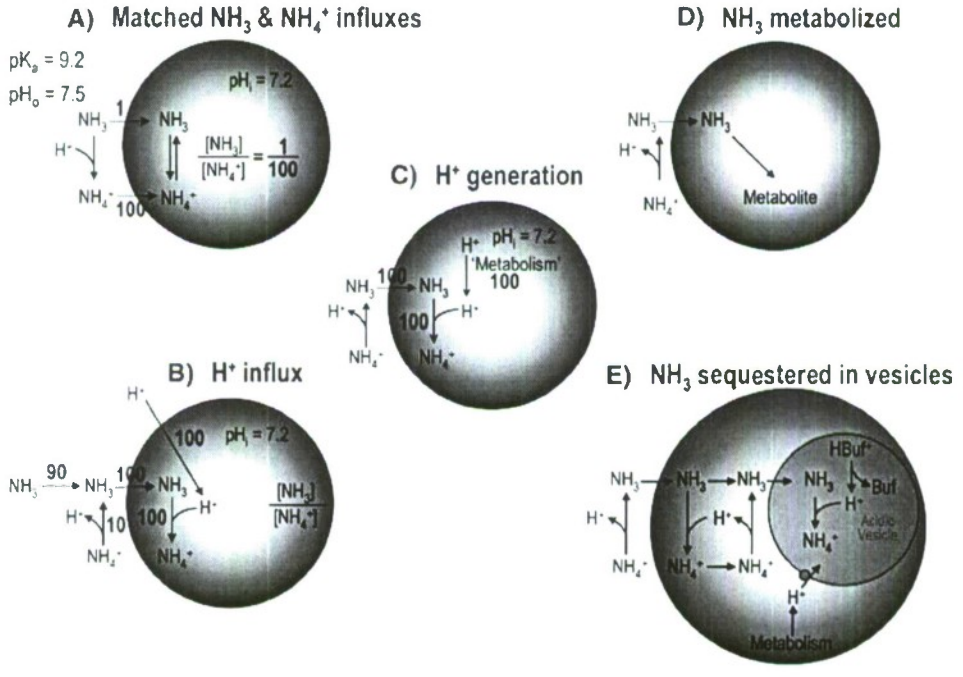

Fig. 7 Models of NH_3/NH_4^+ handling by *Xenopus* oocytes

Thus, if $J_{NH_3}/J_{NH_4^+}$ also were 1/100, then the parallel influxes of NH_3 and NH_4^+ would not disturb the ratio $[NH_3]_i/[NH_4^+]_i$ and hence would not disturb the NH_3/NH_4^+ equilibrium or pH_i. (In Fig. 7a, we assume an NH_3 influx of 100 arbitrary units.) We now define the virtual $J_{NH_3}/J_{NH_4^+}$ ratio that would produce no change in the actual pH_i:

$$\left(\frac{J_{NH_3}}{J_{NH_4^+}}\right)_{Null} \equiv \frac{[NH_3]_i}{[NH_4^+]_i} = 10^{pH_i - pK_a} \quad (2)$$

In our example $(J_{NH_3}/J_{NH_4^+})_{Null}$ is 1/100. To be more general, we can define $(J_{NH_3}/J_{NH_4^+})_{Null}$ in terms of the pH on either side of the membrane:

$$\left(\frac{J_{NH_3}}{J_{NH_4^+}}\right)_{Null} = \frac{[NH_3]_i}{[NH_4^+]_i} = 10^{pH - pK_a} \quad (3)$$

Because solutions on opposite sides of the membrane will generally have different pH values, they will also have different requirements for $(J_{NH_3}/J_{NH_4^+})_{Null}$, which—as we see below—can have interesting consequences.

We can also define the virtual value of pH that—given the actual fluxes of NH_3 and NH_4^+—would produce no pH change in the compartment under consideration. Starting with an expression analogous to Eq. 3 and solving for pH, we have

$$pH_{Null} = pK_a + \log\frac{J_{NH_3}}{J_{NH_4^+}} \quad (4)$$

This equation has the form of the familiar Henderson-Hasselbalch equation, except that here we replace concentrations with fluxes. If the $J_{NH_3}/J_{NH_4^+}$ ratio were 1/100 and pK_a were 9.2, then pH_{Null} would be

$$pH_{Null} = 9.2 + \log\frac{1}{100} = 7.2 \quad (5)$$

If the actual pH_i were 7.2 (i.e., the same as pH_{Null} in this example), the NH_3/NH_4^+ fluxes would not alter pH_i. However, because the pH of the bulk extracellular fluid is 7.5, this same $J_{NH_3}/J_{NH_4^+}$ ratio of 1/100 would necessarily alter pH_S. To determine the direction of the effect on pH_S, we return to Eq. 3. For the NH_3/NH_4^+ fluxes to produce no change in pH_S (where the initial $pH_S = pH_{Bulk} = 7.50$),

$$\left(\frac{J_{NH_3}}{J_{NH_4^+}}\right)_{Null} = 10^{(pH_{Bulk} - pK_a)} = 10^{(7.5-9.2)} = \frac{1}{50} = \frac{2}{100} \quad (6)$$

To produce the observed decrease in pH_S, as in Fig. 1, the fluxes would have to be in a ratio >1/50 (or 2/100). However, if $J_{NH_3}/J_{NH_4^+}$ were only 1/100—the value necessary to stabilize pH_i—the influx of NH_3 would be too low (or the influx of NH_4^+ would be too high) to stabilize pH_S, and the following reaction on the extracellular surface of the oocyte would replenish some of the lost NH_4^+: $NH_3 + H^+ \rightarrow NH_4^+$ (Fig. 7a). Thus, if the $J_{NH_3}/J_{NH_4^+}$ ratio were positioned to stabilize pH_i, pH_S would rise, rather than fall as actually observed. Obviously, $J_{NH_3}/J_{NH_4^+}$ cannot simultaneously be 1/100 (to explain the stability of pH_i) and >2/100 (to explain the fall in pH_S). Therefore, no combination of NH_3 influx and NH_4^+ influx—regardless of mechanism (e.g., influx through a Na/K/Cl cotransporter or a channel)—can simultaneously account, by itself, for the pH_i and pH_S data. Thus, we can rule out model A for experiments at 0.5 mM NH_3/NH_4^+. Below, we see that a similar line of reasoning rules out NH_4^+ influx as a potential mechanism for the paradoxical fall of pH_i in 5 mM NH_3/NH_4^+.

Table 1 summarizes the directions of the expected pH changes for the three possible conditions: $pH < pH_{Null}$, $pH = pH_{Null}$, and $pH > pH_{Null}$.[1] These pH vs. pH_{Null} relationships are mirrored by corresponding $J_{NH_3}/J_{NH_4^+}$ vs. $(J_{NH_3}/J_{NH_4^+})_{Null}$ relationships. Notice that, in the case of inequalities, the directions of the pH changes are opposite on the side from which the NH_3 and NH_4^+ exit vs. the side which NH_3 and NH_4^+ enter.

Note that the model that we developed here only allows us to conclude that a NH_3/NH_4^+-induced fall in pH_S in our experiments is associated with a $J_{NH_3}/J_{NH_4^+}$ that is >1/50. We cannot rule out an influx of NH_4^+. In fact, a hypothetical influx of NH_4^+ could be 49-fold greater than the influx of NH_3, and yet pH_S still would fall. On the other hand, a large absolute influx of NH_4^+ would slow the fall in pH_S and reduce the magnitude of $-pH_S$. Such kinetic issues can only be addressed by a model that computes the time course of pH_S.

Model B: Is the Influx of NH_3 Perfectly Matched by an Influx of H^+ (Fig. 7b)?

Even if NH_4^+ did not enter the oocyte, pH_i would be stable if J_{NH_3} were matched by a comparable J_{H+}. Each entering NH_3 would undergo the reaction $NH_3 + H^+ \rightarrow NH_4^+$, and the lost cytosolic H^+ would be replenished by an influx of H^+. In Fig. 7b, we assume a J_{H+} of 100 arbitrary units and a J_{NH_3} of 100, and we also assume that the NH_3 disappearing from the extracellular surface of the cell would be replenished by an NH_3 diffusion from the bulk extracellular fluid (ECF) of 90 and a contribution of 10 from the extracellular reaction $NH_4^+ \rightarrow H^+ + NH_3$. Because this model results in a net consumption of H^+ at the extracellular surface (100 – 10 = 90 in this example), pH_S would rise rather than fall as we observe. Moreover, this model would predict an enormous production of intracellular NH_4^+, which would produce cell swelling; we observe no

[1] In our analysis, we assume that NH_3 and NH_4^+ move in the same direction. If they should move in opposite directions, then pH would always fall on the side of the membrane toward which NH_4^+ moves, and would always rise on the opposite side.

Table 1 Predicted pH changes

Condition	Effect on compartment from which NH_3 and NH_3/NH_4^+ leave	Effect on compartment that NH_3 and NH_3/NH_4^+ enter
$pH < pH_{Null}$ ... that is, $J_{NH_3}/J_{NH_4^+} > (J_{NH_3}/J_{NH_4^+})_{Null}$	↓ pH	↑ pH
$pH = pH_{Null}$ ... that is, $J_{NH_3}/J_{NH_4^+} = (J_{NH_3}/J_{NH_4^+})_{Null}$	$\not\Delta$ pH	$\not\Delta$ pH
$pH > pH_{Null}$ ... that is, $J_{NH_3}/J_{NH_4^+} < (J_{NH_3}/J_{NH_4^+})_{Null}$	↑ pH	↓ pH

Note. ↓pH, decrease in pH; ↑pH, increase in pH; $\not\Delta$ pH, no pH change in this compartment

tendency for the oocyte to swell. Finally, the massive accumulation of intracellular NH_4^+ would, upon removal of extracellular NH_3/NH_4^+, lead to a substantial decline in pH_i and overshoot of pH_S (i.e., increase beyond the pH_{Bulk} value of 7.50), neither of which we observe. In this analysis, we have assumed no flux of NH_4^+. To the extent that NH_4^+ entered the oocyte, we would require less H^+ influx to produce no pH_i change. However, any substantial H^+ influx would be inconsistent with our pH_S data, and we have already seen in our analysis of model A that NH_4^+ influx cannot account for our data. It is theoretically possible that the oocyte could export NH_4^+, thereby avoiding swelling. However, the electrochemical gradient for NH_4^+ is inward, and in any case pH_S would rise (rather than fall, as we observe). Therefore, model B is incorrect.

Model C: Is the Influx of NH_3 Perfectly Matched by the Metabolic Production of H^+ (Fig. 7c)?

This analysis is similar to that for model B except that we can ignore the incorrect predictions that stem from H^+ influx across the plasma membrane. Nevertheless, we are left with the massive accumulation of intracellular NH_4^+, which would lead to cell swelling and—upon NH_3/NH_4^+ removal—a large pH_i decline and a large pH_S overshoot, neither of which we observe.

Model D: Is Virtually all Entering NH_3 Metabolized to a Neutral Product(s)? (Fig. 7d)?

If an amido-transferase reaction (e.g., the conversion of glutamate to glutamine) consumed the entering NH_3, pH_i would not change. Moreover, NH_4^+ would not accumulate inside the cell during the NH_3/NH_4^+ exposure. Thus following the withdrawal of extracellular NH_3/NH_4^+, pH_i would not fall and pH_S would not overshoot pH_{Bulk}. To test model D, we attempted to detect Gln by both ^1H-[^{13}C] (Fig. 5) and ^1H-^{15}N-HSQC NMR spectroscopy, but observed little Gln or other likely NH_3 metabolite. These data, combined with our demonstration of substantial NH_3/NH_4^+ accumulation (Fig. 6)—presumably in acidic intracellular vesicles—make it unlikely that the oocyte performs substantial conversion of NH_3 by metabolic processes.

Model E: Is Virtually all Entering NH_3 Sequestered in an Acidic Subcompartment as NH_4^+ (Fig. 7e)?

In this model, a small fraction of entering NH_3 equilibrates with H^+ to produce NH_4^+ in a cytoplasmic microenvironment immediately below the surface of the plasma membrane. Both the NH_3 and the NH_4^+ would diffuse slightly deeper into the oocyte, where NH_3 enters an acidic vesicle and becomes trapped as NH_4^+. To test this hypothesis, we used ^1H-^{15}N HSQC NMR spectroscopy to measure total intercellular NH_3/NH_4^+, finding values (Fig. 6) that were far too high to represent cytosolic NH_3/NH_4^+. Thus, we conclude that the vast majority of intracellular NH_3/NH_4^+ must be trapped as NH_4^+ in vesicles. Indeed, oocytes contain copious yolk granules or platelets (50% of oocyte volume), containing yolk proteins (80% of total cell proteins), and having a pH of ~5.6 (Fagotto and Maxfield 1994a, 1994b; Fagotto 1995). By microscopy, a layer of vesicles begins within ~10 μm of the plasma membrane (Lu et al. 2006).

We predict that—at least during brief experiments such as ours—NH_3/NH_4^+ levels would rise only modestly in the small subcompartment between the membrane and the vesicles, and relatively little of the entering NH_3 could escape the aforementioned vesicles to penetrate deeper into the oocyte. The influx of NH_3 into the vesicle would lead to a fall in $[NH_3]$ at the vesicle surface, favoring the reaction $NH_4^+ \rightarrow NH_3 + H^+$, which would minimize pH_i changes. It is possible that a high intravesicular buffering power (provided by abundant yolk proteins) could, by itself, sufficiently stabilize intravesicular pH over the course of our experiments. In addition, vesicular H^+ pumps could replenish intravesicular H^+, with cytosolic metabolism providing the necessary H^+, again tending to stabilize cytosolic pH.

The NH_4^+-trapping hypothesis would account for all key, paradoxical findings dealing with NH_3. (1) The extracellular addition of 0.5 mM NH_3/NH_4^+ produces a pH_i change of virtually nil (the conversion of incoming NH_3 to NH_4^+ occurs in a subcompartment, not in the cytosol). (2) The fall in pH_S produced by the extracellular addition of NH_3/NH_4^+ relaxes very slowly (NH_3 continues to enter the subcompartment, and perhaps deeper into the

oocyte, for many tens of minutes). (3) The extracellular removal of NH_3/NH_4^+ causes virtually no fall in pH_i (virtually no NH_4^+ is present in the cytosol). And (4) the extracellular removal of NH_3/NH_4^+ produces little or no overshoot of pH_S (because little NH_3/NH_4^+ is present free in the cytosol near the plasma membrane, the efflux of NH_3 is very low).

Models of NH_3/NH_4^+ Handling by *Xenopus* Oocytes: "High" $[NH_3/NH_4^+]_o$

Compared to the analysis of data from experiments with 0.5 mM NH_3/NH_4^+, that of data from experiments with 5 mM NH_3/NH_4^+ is complicated by the paradoxical fall in pH_i (Fig. 2), which creates the added paradox that pH falls on both sides of the membrane.

Model A: Does the Influx of NH_4^+ Cause the Paradoxical Fall in pH_i?

Previous investigators favored the hypothesis that the paradoxical fall in pH_i is due to the influx of NH_4^+—via either an Na/K/Cl cotransporter (Keicher and Meech 1994) or a nonselective cation channel (Burckhardt and Frömter 1992)—followed by the cytosolic reaction $NH_4^+ \rightarrow NH_3 + H^+$. The channel hypothesis, in particular, requires that the oocyte dispose of the newly formed NH_3—by either NH_3 efflux or intracellular NH_3 metabolism or sequestration. Our pH_S data (see Fig. 2) demonstrate a net movement of NH_3 into the cell, ruling out the first NH_3-disposal option. In the introductory section, we noted limitations of the Na/K/Cl-cotransporter hypothesis. Moreover, although we agree that a NH_4^+ conductance is a reasonable explanation for the depolarization triggered by the exposure to NH_3/NH_4^+, two arguments will lead us to conclude here that the hypothesized NH_4^+ entry via a nonselective cation channel is not a viable explanation for the paradoxical fall in pH_i. When we apply 5 mM NH_3/NH_4^+, the speed of the pH_i decrease (an index of the hypothesized NH_4^+ influx) is maximal early on and then gradually wanes as pH_i stabilizes (see Fig. 2). On the other hand, the positive shift in V_m is small early on and slowly reaches a maximal value over nearly 15 min. Thus, if the depolarization is an index of permeability to NH_4^+, we conclude that the NH_4^+ conductance develops far too slowly to account for the decrease in pH_i.[2]

Finally, using the same logic as we did for model A in the previous section (see Fig. 7a), we can conclude that it is impossible for the NH_3/NH_4^+-influx ratio to be—at the same time—low enough to cause pH_i to fall and yet high enough to cause pH_S to fall. For example, if pH_i is 7.2 and pKa is 9.2, then $(J_{NH_3}/J_{NH_4^+})_{Null}$ would be 1/100. Thus, for the influx of NH_4^+ to lower pH_i, $J_{NH_3}/J_{NH_4^+}$ would have to be <1/100. However, as we saw earlier, for the influxes of NH_3/NH_4^+ to lower pH_S $(J_{NH_3}/J_{NH_4^+})_{Null}$ would have to be >2/100. Because $(J_{NH_3}/J_{NH_4^+})_{Null}$ cannot simultaneously be <1/100 and >2/100, the influx of NH_4^+—regardless of mechanism—cannot account for the paradoxical fall in pH_i.

We might note that, at least in theory, it would be possible for the parallel influxes of NH_3 and NH_4^+ to cause both pH_i and pH_S to fall. As noted in Table 1, in the compartment that NH_3 and NH_4^+ enter, the pH would fall if $pH > pH_{Null}$. As we have just seen, a fall in pH_S from an initial value of 7.5 requires that $J_{NH_3}/J_{NH_4^+}$ be >2/100; let us assume a $J_{NH_3}/J_{NH_4^+}$ of 10/100. For this ratio, pH_{Null} would be 8.2. Thus, if the initial pH_i were >8.2, a $J_{NH_3}/J_{NH_4^+}$ of 10/100 would cause pH_i to fall along with pH_S. (Of course, because the actual initial pH_i is far less than 8.2, this explanation is not valid for our data.) Using similar logic, we could predict conditions in which the parallel influxes of NH_3 and NH_4^+ would raise both pH_i and pH_S.

Model B: Does the Influx of H^+ Causes the Paradoxical Fall in pH_i?

As noted in the previous section's model B, in our analysis of data for 0.5 mM NH_3/NH_4^+, even an H^+ influx sufficient to stabilize pH_i in the face of an NH_3 influx (see Fig. 7b) would lead to a rise—rather than the observed fall—in pH_S. Because an even greater H^+ influx would be needed to produce a net fall in pH_i—and such a greater H^+ influx would cause an even greater increase in pH_S—we can rule out the H^+-influx model.

Model C: Does the Intracellular Release or Production of H^+ Cause the Paradoxical Fall in pH_i?

As noted in the previous section's model C (see Fig. 7c), the intracellular generation of H^+—by itself—during the NH_3/NH_4^+ exposure would lead to NH_4^+ accumulation in the cytosol and thus cell swelling (not observed). During NH_3/NH_4^+ withdrawal, the accumulated NH_4^+ would dissociate to produce H^+ (we observed no fall in pH_i) and NH_3, which would exit the cell (we observed no substantial pH_S overshoot). However, if H^+ generation occurred in parallel with trapping—in acidic intracellular vesicles—of nearly all incoming NH_3, then cytosolic H^+ production would promote accumulation of NH_4^+ in vesicles rather than in the cytosol. Thus, this hybrid H^+-generation/vesicular NH_4^+-trapping model (see Fig. 7e) would account for our data with 5 mM NH_3/NH_4^+.

[2] We cannot rule out the possibility that the NH_4^+ conductance is immediately high, but that other conductances—also initially high—gradually decline to allow V_m to approach $E_{NH_4^+}$.

Model D: Does the Closing of NH_4^+-Permeable Channels Cause pH_i to Rise Following Withdrawal of High Levels of NH_3/NH_4^+?

The only explanation offered by previous investigators for the observed rise in pH_i with NH_3/NH_4^+ removal is that the sudden repolarization of the oocyte membrane would close nonselective cation channels and thus allow a slow efflux of accumulated cytosolic NH_4^+, leading to a sluggish pH_i recovery (Burckhardt and Frömter 1992). Presumably, the release of previously sequestered NH_3 would lead to the cytosolic reaction $NH_3 + H^+ \rightarrow NH_4^+$, which would lead to a slow rise in pH_i. One argument against the channel model is that, as already noted, our data[3] indicate that $[NH_4^+]$ in the cytosol near the inner surface of the plasma membrane must be very low, and thus NH_4^+ efflux could not produce a sustained pH_i increase. Consistent with this idea, following the removal of NH_3/NH_4^+, the V_m undershoot is small and short-lived (Fig. 2).[4] A much stronger argument flows from our new analysis of $(J_{NH_3}/J_{NH_4^+})_{Null}$ values. For a hypothetical efflux of NH_4^+ to cause a rise in pH_i—starting from an initial pH_i of, say, 6.9—the absolute value of $(J_{NH_3}/J_{NH_4^+})_{Null}$ would have to be $<[NH_3]_i/[NH_4^+]_i = 10^{(6.9-9.2)} = 0.5/100$ (see Eq. 3 and Table 1). On the other hand, even though pH_S does not exhibit a substantial overshoot of its initial value, the small pH_S overshoot that we do observe indicates that $|J_{NH_3}/J_{NH_4^+}|$ would have to be $>10^{(7.5-9.2)} = 2/100$ (see Table 1). Because $|J_{NH_3}/J_{NH_4^+}|$ cannot simultaneously be <0.5/100 and >2/100, we can conclude that an NH_4^+ efflux, regardless of mechanism, cannot account for the slow pH_i increase.

Model E: Might Endogenous Na–H Exchange Cause pH_i to Rise Following Withdrawal of High Levels of NH_3/NH_4^+?

After an intracellular acid load induced by exposure to CO_2 or butyric acid, *Xenopus* oocytes not heterologously expressing acid-base transporters have very low rates of acid extrusion (Romero et al. 1997; Grichtchenko et al. 2001; Piermarini et al. 2007). Thus, the pH_i recovery occurs only after removal of NH_3/NH_4^+. Furthermore, by analogy to the argument made in the previous section's point B (see Fig. 7b), the extrusion of H^+ would have produced a fall in pH_S, rather than the small overshoot that we observed (Fig. 2). Thus, acid extrusion by an endogenous transporter also cannot account for the pH_i recovery.

Model F: Might the Activation (or Inactivation) of Cytosolic H^+ Production Cause the Fall (or rise) in pH_i Caused by the Application (or Removal) of Extracellular NH_3/NH_4^+?

Although we can rule out NH_4^+ or H^+ uptake as an explanation for the paradoxical pH_i decrease caused by the application of 5 mM NH_3/NH_4^+ (and presumably higher concentrations as well)—and NH_4^+ or H^+ efflux as an explanation for the paradoxical pH_i increase caused by removal of high levels of NH_3/NH_4^+—we have no definitive explanation for either pH_i change. Others have proposed that members of the Rh family function as NH_3/NH_4^+ sensors in determining the choice of slug vs. culmination in *Dictyostelium discoideum* (Kirsten et al. 2005, 2008; Singleton et al. 2006). We propose that oocytes have a low-affinity "sensor" that responds, directly or indirectly, to extracellular NH_3/NH_4^+. This oocyte sensor could be either at the outer surface of the plasma membrane or somewhere reasonably close to the inner surface, but ultimately must act in two ways. (a) The sensor triggers the production of cytosolic H^+—perhaps by a metabolic pathway. The influx of NH_3 would temper the fall in pH_i and lead to the formation of some NH_4^+, which also would temper the depolarization by reducing the inwardly directed NH_4^+ diffusion potential. Indeed, AmtB reduces the depolarization (compare AmtB vs. H_2O bars in Fig. 4d and h). However, ultimately, the overwhelming majority of the incoming NH_3 must be trapped as NH_4^+ in a presumably acidic intracellular compartment. (b) The oocyte sensor triggers the slow activation of a channel permeable to NH_4^+. We have no data to address the issue of whether this activation requires the attendant fall in pH_i, or whether the putative increase in NH_4^+ permeability and the observed fall in pH_i are totally independent. Note that NH_4^+ need not enter in order to depolarize the cell. We suggest that removal of extracellular NH_3/NH_4^+ reverses this production, leading to consumption of H^+ and thus the recovery of pH_i. Because the pH_i recovery begins so soon after NH_3/NH_4^+ removal, we suggest that the NH_3/NH_4^+ sensor faces the extracellular fluid.

V_m Changes

As noted earlier, the slowly developing depolarization that develops in the presence of NH_3/NH_4^+ could reflect permeability to NH_4^+, as suggested by others (Burckhardt and Frömter 1992). It is interesting to note that, at 5 both mM

[3] The removal of NH_3/NH_4^+ causes neither a fall in pH_i nor a rise in pH_S that substantially overshoots the initial value.

[4] Assuming that the NH_4^+-conductive pathway remained activate and that substantial NH_4^+ were present in the cytosol, the removal of extracellular NH_4^+ would create a diffusion potential that would drive V_m to well below the pre-NH_3/NH_4^+ value. Instead, we observed a V_m minimal undershoot that decayed rapidly, presumably reflecting either NH_4^+ efflux per se, or NH_3 efflux followed by the cytosolic reaction $NH_4^+ \rightarrow NH_3 + H^+$. We have no data that bear on the decay of the presumed NH_4^+ conductance.

and 0.5 mM NH_3/NH_4^+, expression of AmtB substantially reduced the NH_3/NH_4^+-induced depolarization (Fig. 4d and h) without significantly affecting pH_i (Fig. 4b and f). We hypothesize that the additional influx of NH_3 through AmtB leads to the formation of modest amounts of NH_4^+ immediately beneath the plasma membrane, reducing the diffusion gradient for NH_4^+.

Possible Benefits of the Oocyte's Unusual Handling of NH_3/NH_4^+

An intriguing question that remains is why the oocyte should handle NH_3 in such an unusual manner. One possibility is that the oocyte's responses to extracellular NH_3/NH_4^+ are an adaptation that protects the cell—and perhaps, more importantly, its developmental program—from the appearance of NH_3 in pond water that contains decaying organic matter and thus NH_3/NH_4^+. Levels up to at least 0.5 mM NH_3/NH_4^+ cause no discernible changes in pH_i, and even much higher levels lead, at most, to modest, slow, and fully reversible pH_i changes. In a more typical response, an exposure to NH_3/NH_4^+ might mimic the rise in pH_i caused by the fertilization of a *Xenopus* oocyte (Webb and Nuccitelli 1981; Nuccitelli et al. 1981). The *Xenopus* oocyte seems to be particularly adept at avoiding NH_3/NH_4^+-induced pH_i increases.

Acknowledgments This work was supported by grants from the Office of Naval Research (1N000140810532 to W.F.B.) and the National Institutes of Health (NINDS 1 P30-NS052519 to K.L.B.). At Yale University, we thank Duncan Wong for computer support. We thank Mark D. Parker for helpful discussions, Dale Huffman for engineering assistance, and Charleen Bertolini for administrative support.

References

Aickin CC, Thomas RC (1977) An investigation of the ionic mechanism of intracellular pH regulation in mouse soleus muscle fibres. J Physiol (Lond) 273:295–316

Andrade SL, Dickmanns A, Ficner R, Einsle O (2005) Crystal structure of the archaeal ammonium transporter Amt-1 from Archaeoglobus fulgidus. Proc Natl Acad Sci USA 102:14994–14999

Bakouh N, Benjelloun F, Hulin P, Brouillard F, Edelman A, Chérif-Zahar B, Planelles G (2004) NH3 is involved in the NH4+ transport induced by the functional expression of the human Rh C glycoprotein. J Biol Chem 279:15975–15983

Bakouh N, Benjelloun F, Cherif-Zahar B, Planelles G (2006) The challenge of understanding ammonium homeostasis and the role of the Rh glycoproteins. Transfus Clin Biol 13:139–146

Boron WF, De Weer P (1976a) Active proton transport stimulated by CO_2/HCO_3^- blocked by cyanide. Nature 259:240–241

Boron WF, De Weer P (1976b) Intracellular pH transients in squid giant axons caused by CO_2, NH_3 and metabolic inhibitors. J Gen Physiol 67:91–112

Burckhardt BC, Frömter E (1992) Pathways of NH_3/NH_4^+ permeation across Xenopus laevis oocyte cell membrane. Pflügers Arch 420:83–86

Chesler M (1986) Regulation of intracellular pH in reticulospinal neurones of the lamprey, Petromyzon Marinus. J Physiol (Lond) 381:241–261

Conroy MJ, Durand A, Lupo D, Li XD, Bullough PA, Winkler FK, Merrick M (2007) The crystal structure of the Escherichia coli AmtB-GlnK complex reveals how GlnK regulates the ammonia channel. Proc Natl Acad Sci USA 104:1213–1218

De Hemptinne A, Huguenin F (1984) The influence of muscle respiration and glycolysis on surface and intracellular pH in fibres of the rat soleus. J Physiol 347:581–592

Endeward V, Musa-Aziz R, Cooper GJ, Chen L, Pelletier MF, Virkki LV, Supuran CT, King LS, Boron WF, Gros G (2006) Evidence that Aquaporin 1 is a major pathway for CO2 transport across the human erythrocyte membrane. FASEB J 20:1974–1981

Fabiny JM, Jayakumar A, Chinault AC, Barnes EM Jr (1991) Ammonium transport in Escherichia coli: localization and nucleotide sequence of the amtA gene. J Gen Microbiol 137(Pt 4): 983–989

Fagotto F (1995) Regulation of yolk degradation, or how to make sleepy lysosomes. J Cell Sci 108(Pt 12):3645–3647

Fagotto F, Maxfield FR (1994a) Changes in yolk platelet pH during *Xenopus laevis* development correlate with yolk utilization. A quantitative confocal microscopy study. J Cell Sci 107:3325–3337

Fagotto F, Maxfield FR (1994b) Yolk platelets in *Xenopus* oocytes maintain an acidic internal pH which may be essential for sodium accumulation. J Cell Biol 125:1047–1056

Grichtchenko II, Choi I, Zhong X, Bray-Ward P, Russell JM, Boron WF (2001) Cloning, characterization, and chromosomal mapping of a human electroneutral Na^+-driven Cl-HCO_3 exchanger. J Biol Chem 276:8358–8363

Grzesiek S, Bax A (1993) The importance of not saturating H_2O in protein NMR - application to sensitivity enhancement and NOE measurements. J Am Chem Soc 115:12593–12594

Harvey EN (1911) Studies on the permeability of cells. J Exp Zool 10:507–556

Jacobs MH (1922) The influence of ammonium salts on cell reaction. J Gen Physiol 5:181–188

Kanamori K, Ross BD, Tropp J (1995) Selective, in vivo observation of [5-N-15]glutamine amide protons in rat-brain by H-1-N-15 heteronuclear multiple-quantum-coherence transfer NMR. J Magnet Reson Ser B 107:107–115

Keicher E, Meech R (1994) Endogenous Na^+ -K^+ (or NH_4^+)-$2Cl^-$ cotransport in Rana oocytes; anomalous effect of external NH4 + on pHi. J Physiol 475:45–57

Khademi S, Stroud RM (2006) The Amt/MEP/Rh family: structure of AmtB and the mechanism of ammonia gas conduction. Physiology (Bethesda) 21:419–429

Khademi S, O'Connell J, Remis J, Robles-Colmenares Y, Miercke LJW, Stroud RM (2004) Mechanism of ammonia transport by Amt/MEP/Rh: Structure of AmtB at 1.35 angstrom. Science 305:1587–1594

Kikeri D, Sun A, Zeidel ML, Hebert SC (1989) Cell membranes impermeable to NH_3. Nature 339:478–480

Kirsten JH, Xiong Y, Dunbar AJ, Rai M, Singleton CK (2005) Ammonium transporter C of *Dictyostelium discoideum* is required for correct prestalk gene expression and for regulating the choice between slug migration and culmination. Dev Biol 287:146–156

Kirsten JH, Xiong Y, Davis CT, Singleton CK (2008) Subcellular localization of ammonium transporters in *Dictyostelium discoideum*. BMC Cell Biol 9:71

Lu J, Daly CM, Parker MD, Gill HS, Piermarini PM, Pelletier MF, Boron WF (2006) Effect of human carbonic anhydrase II on the activity of the human electrogenic Na/HCO_3 cotransporter NBCe1-A in Xenopus oocytes. J Biol Chem 281:19241–19250

Musa-Aziz R, Chen L, Pelletier MF, Boron WF (2009) Relative CO_2/NH_3 selectivities of AQP1, AQP4, AQP5, AmtB and RhAG. Proc Natl Acad Sci USA (in press)

Nuccitelli R, Webb DJ, Lagier ST, Matson GB (1981) ^{31}P NMR reveals increased intracellular pH after fertilization in Xenopus eggs. Proc Natl Acad Sci USA 78:4421–4425

Overton E (1897) Über die osmotischen Eigenschaften der Zelle in ihrer Bedeutung fur die Toxicologie und Pharmacologie. Z Phys Chem 22:189–209

Parker MD, Musa-Aziz R, Rojas JD, Choi I, Daly CM, Boron WF (2008) Characterization of human SLC4A10 as an electroneutral Na/HCO3 cotransporter (NBCn2) with Cl–self-exchange activity. J Biol Chem 283:12777–12788

Patel AB, de Graaf RA, Mason GF, Rothman DL, Shulman RG, Behar KL (2005) The contribution of GABA to glutamate/glutamine cycling and energy metabolism in the rat cortex in vivo. Proc Natl Acad Sci USA 102:5588–5593

Piermarini PM, Choi I, Boron WF (2007) Cloning and characterization of an electrogenic Na/HCO_3 cotransporter from the squid giant fiber lobe. Am J Physiol Cell Physiol 292:C2032–C2045

Piotto M, Saudek V, Sklenar V (1992) Gradient-tailored excitation for single-quantum NMR-spectroscopy of aqueous solutions. J Biomol NMR 2:661–665

Romero MF, Hediger MA, Boulpaep EL, Boron WF (1997) Expression cloning and characterization of a renal electrogenic Na^+/HCO_3^- cotransporter. Nature 387:409–413

Romero MF, Fong P, Berger UV, Hediger MA, Boron WF (1998) Cloning and functional expression of rNBC, an electrogenic Na^+/HCO_3^- cotransporter from rat kidney. Am J Physiol 274:F425–F432

Roos A, Boron WF (1981) Intracellular pH. Physiol Rev 61:296–434

Shaka AJ, Keeler J, Frenkiel T, Freeman R (1983) An improved sequence for broad-band decoupling—waltz-16. J Magnet Reson 52:335–338

Singh SK, Binder HJ, Geibel JP, Boron WF (1995) An apical permeability barrier to NH_3/NH_4^+ in isolated, perfused colonic crypts. Proc Natl Acad Sci USA 92:11573–11577

Singleton CK, Kirsten JH, Dinsmore CJ (2006) Function of ammonium transporter A in the initiation of culmination of development in *Dictyostelium discoideum*. Eukaryot Cell 5:991–996

Soupene E, Lee H, Kustu S (2002) Ammonium/methylammonium transport (Amt) proteins facilitate diffusion of NH_3 bidirectionally. Proc Natl Acad Sci USA 99:3926–3931

Toye AM, Parker MD, Daly CM, Lu J, Virkki LV, Pelletier MF, Boron WF (2006) The human NBCe1-A mutant R881C, associated with proximal renal tubular acidosis, retains function but is mistargeted in polarized renal epithelia. Am J Physiol Cell Physiol 291:C788–C801

Waisbren SJ, Geibel JP, Modlin IM, Boron WF (1994) Unusual permeability properties of gastric gland cells. Nature 368:332–335

Warburg EJ (1922) Studies on carbonic acid compounds and hydrogen ion activities in blood and salt solutions. A contribution to the theory of the equation of Lawrence J. Henderson and K.A. Hasselbalch. Biochem Z 16:153–340

Webb DJ, Nuccitelli R (1981) Direct measurement of intracellular pH changes in Xenopus eggs at fertilization and cleavage. J Cell Biol 91:562–567

Zheng L, Kostrewa D, Berneche S, Winkler FK, Li XD (2004) The mechanism of ammonia transport based on the crystal structure of AmtB of Escherichia coli. Proc Natl Acad Sci USA 101:17090–17095

Available online at www.sciencedirect.com
ScienceDirect
Journal of Structural Biology 157 (2007) 534–544
Journal of Structural Biology
www.elsevier.com/locate/yjsbi

Exploring gas permeability of cellular membranes and membrane channels with molecular dynamics

Yi Wang [a], Jordi Cohen [a,d], Walter F. Boron [b], Klaus Schulten [a,d], Emad Tajkhorshid [a,c,*]

[a] Theoretical and Computational Biophysics Group, Beckman Institute, University of Illinois at Urbana-Champaign, Urbana, IL 61801, USA
[b] Department of Cellular and Molecular Physiology, Yale University School of Medicine, New Haven, CT 06520, USA
[c] Department of Biochemistry, University of Illinois at Urbana-Champaign, Urbana, IL 61801, USA
[d] Department of Physics, University of Illinois at Urbana-Champaign, Urbana, IL 61801, USA

Received 12 August 2006; received in revised form 28 October 2006; accepted 3 November 2006
Available online 4 January 2007

Abstract

Aquaporins are a family of membrane proteins specialized in rapid water conduction across biological membranes. Whether these channels also conduct gas molecules and the physiological significance of this potential function have not been well understood. Here we report 140 ns of molecular dynamics simulations of membrane-embedded AQP1 and of a pure POPE bilayer addressing these questions. The permeability of AQP1 to two types of gas molecules, O_2 and CO_2, was investigated using two complementary methods, namely, explicit gas diffusion simulation and implicit ligand sampling. The simulations show that the central (tetrameric) pore of AQP1 can be readily used by either gas molecule to permeate the channel. The two approaches produced similar free energy profiles associated with gas permeation through the central pore: a −0.4 to −1.7 kcal/mol energy well in the middle, and a 3.6–4.6 kcal/mol energy barrier in the periplasmic vestibule. The barrier appears to be mainly due to a dense cluster of water molecules anchored in the periplasmic mouth of the central pore by four aspartate residues. Water pores show a very low permeability to O_2, but may contribute to the overall permeation of CO_2 due to its more hydrophilic nature. Although the central pore of AQP1 is found to be gas permeable, the pure POPE bilayer provides a much larger cross-sectional area, thus exhibiting a much lower free energy barrier for CO_2 and O_2 permeation. As such, gas conduction through AQP1 may only be physiologically relevant either in membranes of low gas permeability, or in cells where a major fraction of the cellular membrane is occupied by AQPs.

Keywords: Aquaporin; AQP1; Gas permeability; O_2; CO_2; Free energy profile; Gas channels

1. Introduction

Aquaporins (AQPs) are a family of membrane channels (Preston et al., 1992; Heymann and Engel, 1999; de Groot and Grubmüller, 2005; Agre et al., 1998; Agre, 2006; Borgnia et al., 1999; Fujiyoshi et al., 2002; Hohmann et al., 2001) that, through modulating the water permeability of biological membranes, play a significant role in water homeostasis in living cells (Agre and Kozono, 2003; Deen and van Os, 1998; Li and Verkman, 2001; King and Agre, 2004; Agre et al., 2004). AQPs organize as tetramers in the membrane, with each monomer forming a functionally independent water pore (Tajkhorshid et al., 2002; de Groot and Grubmüller, 2001). The function of a fifth pore, the "central pore", which is located at the center of the four monomers, remains unclear. Due to their structural simplicity and the approachable timescale of their basic function, e.g., water conduction, AQPs have been investigated extensively with molecular dynamics (MD) simulations (Törnroth-Horsefield et al., 2006; Tajkhorshid et al., 2002, 2003, 2005a,b; Jensen et al., 2001, 2003; Zhu et al., 2001, 2004; de Groot and Grubmüller, 2001, 2005; Grayson et al., 2003). These studies have significantly contributed to our understanding of the molecular basis of their function and selectivity. A particularly intriguing property of AQPs is their ability to block protons (Pohl et al., 2001;

* Corresponding author.
E-mail address: emad@life.uiuc.edu (E. Tajkhorshid).

1047-8477/$ - see front matter © 2006 Elsevier Inc. All rights reserved.
doi:10.1016/j.jsb.2006.11.008

Saparov et al., 2005) while allowing water to pass, a problem that has attracted much attention from theoretical studies (Burykin and Warshel, 2004; Chakrabarti et al., 2004; Tajkhorshid et al., 2002; de Groot et al., 2003; Ilan et al., 2004; de Groot and Grubmüller, 2005; Jensen et al., 2003; Burykin and Warshel, 2003).

Water permeation is by far the best characterized physiological role of AQPs, however, they also participate in other diverse cellular functions. Permeabilities of other small substrates in AQPs have been reported for glycerol (Borgnia and Agre, 2001; Grayson et al., 2003; Heller et al., 1980), urea (Borgnia et al., 1999), nitrate (Ikeda et al., 2002), arsenite (Liu et al., 2002) and even ions (Yool and Weinstein, 2002). Furthermore, some AQPs have been suspected to participate in gas conduction across cellular membranes (Hanba et al., 2004; Nakhoul et al., 1998; Herrera et al., 2006; Cooper and Boron, 1998; Endeward et al., 2006; Cooper et al., 2002; Blank and Ehmke, 2003; Terashima and Ono, 2002; Uehlein et al., 2003; Prasad et al., 1998). For instance, a recent study on tobacco aquaporin NtAQP1 has suggested that NtAQP1 not only facilitates CO_2 permeation when expressed in *Xenopus* oocytes, but also has a significant function in photosynthesis and in stomatal opening (Uehlein et al., 2003). Another study on *Xenopus* oocytes has shown that the CO_2 permeability is increased by about 40% when AQP1 is expressed (Nakhoul et al., 1998; Cooper and Boron, 1998). AQP1 reconstituted in proteoliposomes has been found to increase both water and CO_2 permeabilities markedly (Prasad et al., 1998). However, as lipid membranes are often gas-permeable, characterizing the gas permeability of AQPs is a challenging experimental problem (Verkman, 2002; Fang et al., 2002; Yang et al., 2000). Moreover, the pathway through which gas molecules might permeate AQPs cannot be identified directly through presently available experimental methods. Therefore, it is of great interest as well as importance to further explore the gas permeability of these membrane channels using computational methodologies. A recent simulation study has employed umbrella sampling to calculate the energetics associated with CO_2 permeation through AQP1 (Hub and de Groot, 2006).

To shed light on the gas permeability of AQP1 and on its physiological relevance, we performed a total of 140 ns MD simulations on a membrane-embedded AQP1 tetramer, as well as on pure POPE bilayers. Using two different methodologies, namely *explicit gas diffusion simulation* and *implicit ligand sampling* (Cohen et al., 2006), we have analyzed potential pathways for permeation of O_2 and CO_2 through AQP1, and calculated the associated energetics. In the gas diffusion simulations, 100 CO_2 or O_2 molecules were initially placed in water on both sides of the membrane and allowed to move freely. The implicit ligand sampling, on the other hand, predicts the PMF purely based on simulations of membrane-embedded AQP1 in the absence of explicit gas molecules. Although the two methods work through disparate mechanisms, they have yielded similar results. The PMFs associated with gas permeation revealed a -0.4 to -1.7 kcal/mol energy well in the middle of the AQP1 central pore, and an energy barrier of 3.6–4.6 kcal/mol in the periplasmic entrance. Our results suggest that the hydrophobic central pore of AQP1 is indeed permeable to both CO_2 and O_2. Compared with the well-characterized water pores, the central pore of AQPs is poorly understood, and it remains a long-standing question whether it has any physiological importance. Our simulations suggest that the AQP1 central pore provides a potential pathway for gas permeation, and that this pathway can play a physiological role either in membranes with low intrinsic gas permeabilities, or when a major fraction of the membrane is occupied by AQPs.

2. Methods

2.1. Explicit gas diffusion simulations

Explicit gas diffusion simulations were performed on an AQP1 tetramer embedded in a POPE bilayer, with 100 CO_2 or O_2 molecules initially placed in the water solution. Control simulations were performed on pure POPE bilayers without AQP1. Altogether, four systems, AQP1-CO_2, AQP1-O_2, POPE-CO_2 and POPE-O_2, were investigated using two types of simulations, equilibrium simulations and induced pressure simulations, as described below and summarized in Table 1. The first two systems consisted of a membrane-embedded AQP1 tetramer, while the last two were composed of pure POPE bilayers.

Table 1
The four systems investigated using explicit gas diffusion simulations

System	t_{eq}(ns)	N_{eq}	K_{lw}	D (10^{-5} cm^2/s)	t_p (ns)	N_p
POPE-CO_2	23	25	4.0 ± 0.1	1.80 ± 0.01	10	203
POPE-O_2	15	16	4.7 ± 0.2	2.14 ± 0.01	10	258
AQP1-CO_2	30	1	n/a	1.43 ± 0.09	10	80(6,4)
AQP1-O_2	26	3	n/a	2.39 ± 0.06	10	83(1,6)

n/a, not applicable.
The equilibration time (t_{eq}) and the number of permeation events during equilibrations (N_{eq}) are listed. Partition coefficients between lipids and water (K_{lw}) are shown for POPE-CO_2 and POPE-O_2. Gas diffusion coefficients (D) in water are listed for POPE-CO_2 and POPE-O_2; gas diffusion coefficients in the central pore of AQP1 (D) are shown for AQP1-CO_2 and AQP1-O_2. The simulation time for induced pressure simulations (t_p) and the number of permeation events (N_p) are also listed. Numbers in parenthesis are permeation events through the monomeric water pores and the central pore of AQP1, respectively. K_{lw} was not calculated for the AQP1/bilayer systems due to the inhomogeneity of the membrane composition.

2.1.1. Modeling

A 100×100 Å^2 POPE bilayer patch was initially built using VMD's membrane plugin (Humphrey et al., 1996). Two 20-Å layers of water were then added using the solvate plugin of VMD (Humphrey et al., 1996) to fully hydrate the system; 15 sodium and 15 chloride ions were then added using VMD's autoionize plugin (Humphrey et al., 1996), generating a 50 mM ionic concentration. After 5000 steps of minimization, the lipid tails were "melted" over the course of a 500 ps of constant temperature (310 K) simulation, in which only the lipid tails were allowed to move freely while the rest of the system was fixed. Another 500 ps simulation was then performed under constant temperature (310 K) and constant pressure (1 atm) conditions with all the atoms free to move. Using the last 100 ps of this simulation, we calculated the free volume inside lipids along the membrane normal, with VMD's volmap plugin (Humphrey et al., 1996). The equilibrated POPE bilayer was then used to build the POPE-CO_2 and POPE-O_2 systems, where 100 CO_2 or O_2 molecules were initially placed in the bulk region among water molecules on both sides of the membrane. The AQP1-CO_2 and AQP1-O_2 systems were built in a similar fashion, with the POPE-AQP1 structure taken from a 450 ps equilibration performed by Zhu et al. (2001, 2004). During the equilibration of POPE-AQP1 (Zhu et al., 2001; Zhu et al., 2004), a constraint on the H-bond between the guanidinium group and the backbone oxygen of Arg197 was used to prevent the flipping of the side chain which would block the channel (Wang et al., 2005; Jiang et al., 2006). This constraint was kept in our explicit gas diffusion simulations. The final systems: POPE-CO_2 (82,989 atoms), POPE-O_2 (82,889 atoms), AQP1-CO_2 (81,065 atoms) and AQP1-O_2 (81,052 atoms) share a similar cross-sectional area, with the membrane normal along the z-axis.

2.1.2. Equilibrium simulations

All the four systems were first minimized for 5000 steps. As shown in Table 1, POPE-CO_2 and POPE-O_2 were then equilibrated at constant temperature for 23 ns and 15 ns, respectively; AQP1-CO_2 and AQP1-O_2 were equilibrated under constant temperature and constant pressure conditions for 30 ns and 26 ns, respectively. Fig. 1 shows snapshots of the AQP1-CO_2 and POPE-CO_2 systems after 500 ps of equilibration.

2.1.3. Induced pressure simulations

After the first 10 ns of equilibrium simulation in each system, we applied a force of 20 pN on the center of mass of every gas molecule along the $-z$ direction in a 10 ns "in-

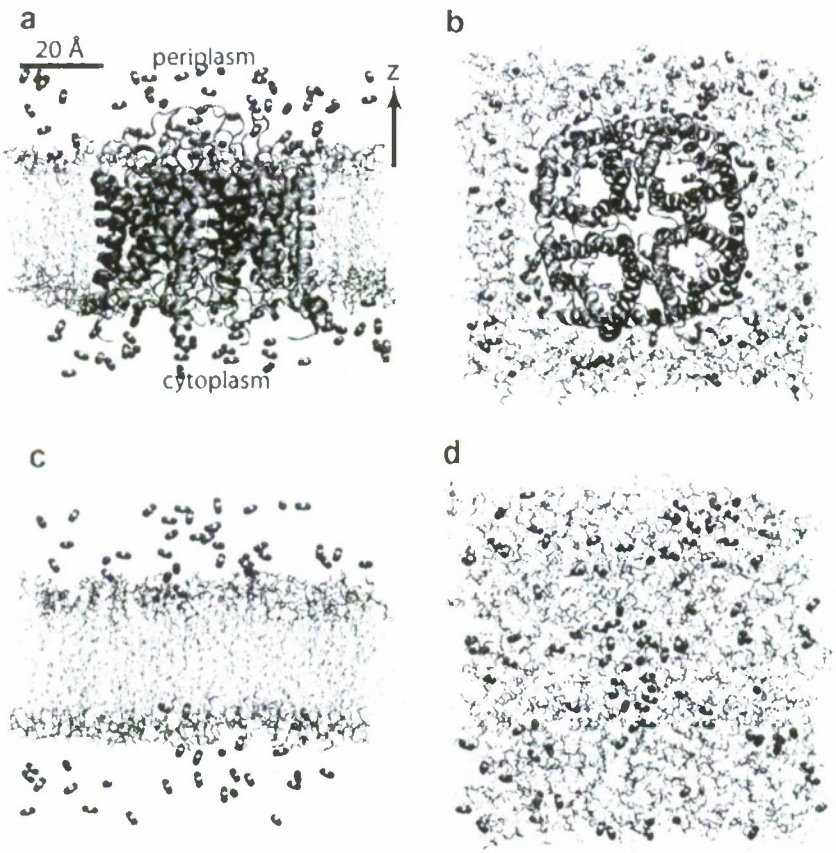

Fig. 1. Side (left panels) and top (right panels) views of the systems AQP1-CO_2 (a,b) and POPE-CO_2 (c,d) after 500 ps of equilibration. The two systems have a similar cross-sectional area, with the membrane normal along the z-axis. CO_2 molecules, initially placed in the bulk region, are drawn in vdW representation.

duced pressure" simulation (Table 1). Previous simulations (Zhu et al., 2002, 2004) had shown that such an external force can generate an effect equivalent to a concentration gradient across the membrane, favoring the diffusion of gas molecules in one direction. Using the force applied in our simulations, a pressure difference of ~20 MPa was generated across the membrane.

2.1.4. Free energy profile calculation

The free energy profile associated with gas permeation was calculated from equilibrium simulations using the relation (Marrink and Berendsen, 1994):

$$\Delta G(z) = -RT \ln \frac{C(z)}{C_{\text{bulk}}} \tag{1}$$

where R is the gas constant, T is the temperature, C_{bulk} is the concentration of gas molecules in bulk water, and $C(z)$ is the concentration of gas molecules in each 1 Å thick layer parallel to the xy plane along the z-axis. For AQP1-CO_2 and AQP1-O_2, $C(z)$ is the gas concentration inside the central pore, except in the bulk water region ($z \geqslant 29$ Å or $z \leqslant -26$ Å), where gas concentration in the entire layer was calculated and then normalized according to the area of an AQP1 tetramer (50 nm^2). This normalization ensures that our calculated PMF corresponds to a definite density of AQP1 (1 AQP1 per 50 nm^2 of bilayer). As a result, by comparing the PMFs for AQP1 and POPE, we can directly determine whether replacing a patch of lipids by AQP1 will increase or decrease the transmembrane barrier to gas permeation.

2.1.5. Diffusion coefficient calculation

The gas diffusion coefficient D was calculated from the slope of the mean square displacement against time using the relationship

$$\langle (r(t + \Delta t) - r(t))^2 \rangle = 2dD\Delta t \tag{2}$$

where r is the coordinates of gas molecules, d is the dimension, and Δt is an arbitrary time interval. As gas molecules may travel through regions with different diffusion coefficients in the chosen time interval, we are limited to small values for Δt (here $\Delta t = 5$ ps), so that D best represents the *local* gas diffusion coefficient in the region it is calculated for (Marrink and Berendsen, 1994; Shinoda et al., 2004). In determining D from the slope of the mean square displacement against time, the first 2 ps was disregarded, in order to ensure that the calculated diffusion coefficient is not contaminated by the velocity correlation of gas molecules. The time origin t was shifted to make use of the entire trajectory and improve statistics. A resolution of 2 Å was used to compute gas diffusion coefficients in lipid bilayers.

Both the free energy profile and diffusion coefficients must be calculated after the system reaches equilibrium. The gas density of the lipid bilayer becomes a natural indicator for the state of the system; since we put all 100 gas molecules in bulk water at the beginning of simulations, the system is approximately at equilibrium

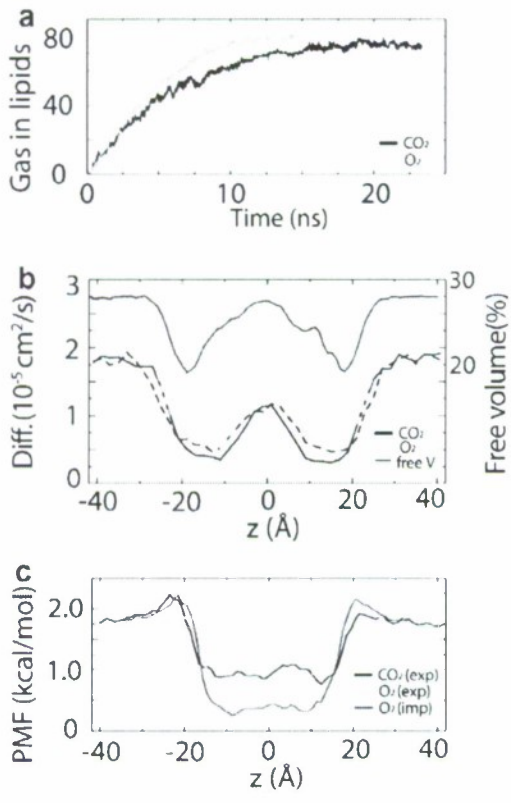

Fig. 2. Partition of gas molecules into the membrane during the explicit gas diffusion simulations. (a) Number of gas molecules inside the POPE bilayer over time (POPE-CO_2: black, POPE-O_2: green). The lipid–water interface is defined as the average position of phosphorus atoms of the POPE monolayers. (b) Lateral (solid lines) and traversal (dashed lines) diffusion coefficients of gas molecules (CO_2: black, O_2: green) in POPE. The percentage of free volume along the membrane normal in the POPE bilayer is shown in blue. Statistical errors of the diffusion coefficients are smaller than 0.2×10^{-5} cm^2/s at the lipid headgroup region, and smaller than 0.1×10^{-5} cm^2/s elsewhere. (c) Free energy profiles calculated using explicit gas diffusion simulations (exp) and implicit ligand sampling (imp). Statistical errors of the PMFs (exp) are smaller than 0.25 kcal/mol at the lipid headgroup region, and smaller than 0.18 kcal/mol elsewhere; the statistical error for PMF (imp) is smaller than 0.25 kcal/mol at all points. In both (b) and (c), $z = 0$ is defined as the mid-point of the phosphorus planes of the two POPE monolayers.

when the net flux of gas molecules across the lipid–water interfaces is zero, and the number of gas molecules inside the lipid bilayer remains constant. Using this indicator, both the POPE-CO_2 and POPE-O_2 simulations are in equilibrium during their last 5 ns of equilibration (Fig. 2a). For the AQP1-embedded membranes, we allowed for a longer equilibration time and discarded the first 10 ns of the simulation. We then investigated the convergence of the PMFs calculated using the remaining data. The PMFs calculated using the last 20, 15 and 10 ns of the simulations were rather similar for the system AQP1-CO_2 (data not shown). Therefore, we chose to use the last 20 ns for the analysis, in order to maximize our sampling. As for AQP1-O_2, we resorted to a better equilibrated system by using the last 10 ns simulation, except for the periplasmic part of the central

pore (16 Å $\leqslant z \leqslant$ 29 Å), where we used the last 16 ns due to a limited sampling in this region.

2.2. Implicit ligand sampling

Implicit ligand sampling is a method to infer the 3D PMF of a weakly interacting ligand, based purely on an equilibrium simulation of the ligand-free system. This method overcomes the problem of low sampling caused by the slow diffusion of explicit ligands exploring a protein and has proven useful in finding gas migration pathways in proteins (Cohen et al., 2005, 2006). Multiple conformations of an imaginary ligand molecule are placed at every point of a grid, on top of an equilibrium trajectory of a simulated protein system. At each time step, and for each ligand position and orientation, the protein–ligand interactions are computed. These interaction energies are then used to reconstruct the PMF of placing the ligand at any point inside the protein using a perturbative approach, as described in detail in Cohen et al. (2006).

In order to compute the PMFs, equilibrium simulations of pure POPE and membrane-embedded AQP1 in the absence of gas molecules were performed for 1 and 5 ns, respectively. The simulation protocols are identical with those used in explicit gas diffusion simulations, except that the temperature was set to 300 K, and the H-bond constraint on Arg197 was not applied. For each of the two systems, a 3D PMF map at 1 Å resolution was computed, using the volmap feature of VMD (Humphrey et al., 1996) with a chargeless model for O_2 (Table S1). For the lipid bilayer and bulk water regions, the projected PMFs along the z-axis, $F(z)$, were then calculated from the 3D PMF map, using the formula:

$$F(z) = -RT \ln \sum_{x,y=0}^{L_x,L_y} \frac{e^{-F(x,y,z)/RT}}{L_x L_y} \tag{3}$$

where $F(x,y,z)$ is the local 3D PMF computed by implicit ligand sampling, and L_x and L_y are the dimensions of the PMF map in units of Å. In the case of AQP1, the calculation is the same as in Eq. (3), except that the summations were performed over restricted cross-sectional areas, in order to isolate the targeted gas channels. The resulting PMF was then shifted by $-RT\ln(L_xL_y/A_0)$, where L_xL_y is the area of the summation, and A_0 is roughly the area occupied by an AQP1 tetramer ($A_0 = 50$ nm^2). This is done so that our absolute values of the PMF can be compared with those from explicit gas diffusion simulations. To compare our PMFs with experiments or other simulations, one would simply shift our barriers by the term $-RT\ln(A_0/A_1)$, where A_1 is the cross-sectional area of the system being used for comparison.

2.3. Error analysis

For the explicit gas diffusion simulations, the statistical errors in the calculation of a variable X were estimated by dividing the trajectory into two sub-trajectories of the same length. X was then calculated using each sub-trajectory. We used the quantity $\mathrm{std}(X)/\sqrt{2}$ as a measure of the statistical error on X in our calculation using the entire trajectory. For the implicit ligand sampling, the estimated error depends on both the measured PMF and the number of independent simulation snapshots used to compute it, and was calculated as described in Cohen et al. (2006).

2.4. MD simulation protocols

For all simulations, the program NAMD 2.6 (Phillips et al., 2005) and the CHARMM27 parameter set (Schlenkrich et al., 1996; MacKerell et al., 1998) were used. Parameters for CO_2 or O_2 were taken from the literature (Harris and Yung, 1995; Schlenkrich et al., 1996; MacKerell et al., 1998) and are listed in Supplemental material (Table S1). Assuming periodic boundary conditions, the Particle Mesh Ewald (PME) method (Darden et al., 1993) with a grid density of at least 1/Å^3 was employed for computation of long-range electrostatic forces. All simulations were performed with time steps of 1, 2, and 4 fs for bonded, non-bonded and PME calculation, respectively. A Langevin piston (Feller et al., 1995) was employed to maintain the pressure at 1 atm in constant pressure simulations. Langevin dynamics was used to keep the temperature constant at 310 K (damping coefficient 5 ps^{-1}), except in the implicit ligand sampling, where the temperature was set to 300 K. During induced pressure simulations, gas molecules were not coupled to the temperature bath, and counter forces were applied to C_α atoms of AQP1 and/or heavy atoms of the POPE bilayer to prevent net translocation of the system along the direction of external force. The total counter force on the membrane was equal to the total external force applied on gas molecules. In the AQP1-CO_2 and AQP1-O_2 systems, the counter force was distributed between the protein and the lipids according to the ratio of their areas in the membrane.

3. Results and discussion

3.1. Gas diffusion in POPE bilayer

Free energy profiles associated with gas permeation through POPE are shown in Fig. 2c. In general, the bilayer has a rather "flat" free energy profile for both CO_2 and O_2, with the largest energy barrier being 1.4 kcal/mol and 1.9 kcal/mol, respectively. Such a profile allows gas molecules to readily diffuse through the lipid bilayer, a behavior observed in our simulations and reflected in the number of permeation events during the equilibrium simulations; on the average one permeation event per nanosecond was observed for both CO_2 and O_2 (Table 1). As shown in Fig. 2c, the PMFs calculated using explicit gas diffusion simulations and implicit ligand sampling are in very good agreement. An energy well of −1.0 kcal/mol for CO_2 and −1.3 to −1.5 kcal/mol for O_2 is located at the bilayer center, while a small barrier of 0.1–0.4 kcal/mol for CO_2 and 0.1–

0.6 kcal/mol for O_2 has to be overcome at the headgroup region where gas molecules eross the lipid–water interface. Our free energy profiles calculated from explicit gas diffusion simulations are mostly symmetrical about the center of the bilayer; the slight asymmetry at the lipid headgroup region, where a 0.3 kcal/mol (for CO_2) or 0.5 kcal/mol (for O_2) energy difference between the two halves of the PMFs is observed, is most likely due to limited sampling.

It is noteworthy that the headgroup region is also the region in whieh gas moleeules exhibit the least mobility. As shown in Fig. 2b, inside the bilayer, traversal (along the z-axis) gas diffusion is almost always faster than the corresponding lateral diffusion; however, both the traversal and lateral diffusions are significantly slower in the headgroup region. Fig. 2b also shows the available free volume calculated from a 100 ps equilibration of the POPE bilayer. It can be expected that gas diffusion across a lipid bilayer is proportional to the available free spaee in the bilayer. In our simulations, the diffusion eoeffieients correlate elosely with the free volume inside the bilayer in all regions.

In our explieit gas diffusion simulations, 100 gas molecules were used in a $\sim 8 \times 10^5$ Å^3 simulation box, generating an overall eoneentration of ~200 mM. Although this eoncentration is higher than physiologieal eoneentrations, given the weak interaetion potentials and the large average distance between the gas molecules only marginal interactions between them are expeeted. As sueh, we do not expeet the results of the explicit gas diffusion simulations to be signilicantly affeeted by the high concentration of gas molecules. The calculated diffusion eoeffieients for CO_2 and O_2 in water are 1.80×10^{-5} cm^2/s and 2.14×10^{-5} cm^2/s, respectively (Table 1), whieh are smaller than the experimental values (2.93×10^{-5} cm^2/s for CO_2 at 313 K (Tamimi et al., 1994), and 3.0×10^{-5} cm^2/s for O_2 at 310 K (Subczynski et al., 1992)).

The O_2 partition coefficient calculated from our simulations is 4.7, elose to the experimentally determined value (3.9) for O_2 in liposomes (Moller et al., 2005). However, our calculated CO_2 partition coeffieient (4.0) is bigger than the experimental value for CO_2 in olive oil (1.7) (Simon and Gutknecht, 1980), which is very likely caused by the statistical error in our simulation and the force field parameters for CO_2. Therefore, it is expeeted that the depth of the free energy well of CO_2 inside the POPE bilayer (Fig. 2e) is also overestimated.

3.2. CO_2 and O_2 permeability across AQP1

For CO_2 and O_2 permeability across AQP1, we again resort to a eombined approaeh, simulating explieit diffusion of CO_2 (30 ns) and O_2 (26 ns) in AQP1, and supporting our results with an independent caleulation of the O_2 PMF using implicit ligand sampling. As was the ease for the lipid bilayers, PMFs calculated using both approaches are in a good agreement, exeept that the implieit ligand sampling deteets additional favorable areas not explored in the explicit gas diffusion simulations, which are far from the water solution

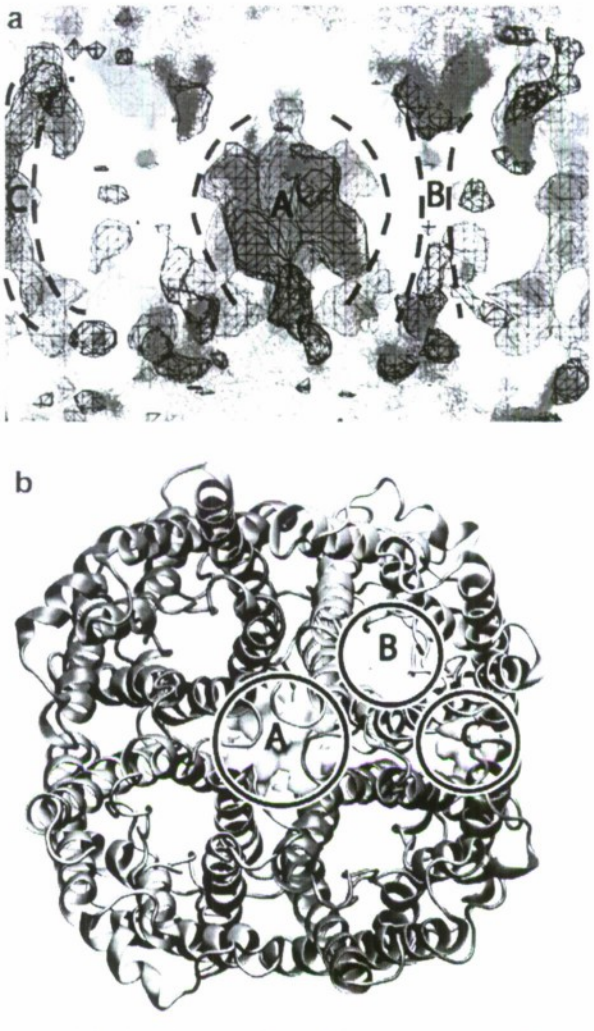

Fig. 3. (a) Side view of the simulated AQP1-O_2 system, showing areas of high O_2 occupancy predicted hy implicit ligand sampling (0.6 kcal/mol energy isosurface shown in blaek wireframe) compared with O_2 locations revealed by explicit gas diffusion simulations (in red, frames taken every 10 ps of the 26-ns simulation). The O_2 trajectories were symmetrized over the AQP1 tetramer such that each monomer shows the locations explored hy O_2 in all four monomers. (b) Top view of the AQP1 tetramer, along with the regions used to compute projected PMFs for each of AQP1's various pores: (A) the central pore, (B) the water pores, (C) the side pores. The 0 kcal/mol energy isosurface of O_2 PMF in these pores is shown in yellow.

and the bilayer. This agreement is highlighted in Fig. 3a, where favorable locations for O_2 revealed by the two approaehes are shown. In our assessment of the gas permeability of AQP1, we have divided the AQP1 tetramer into various regions of interest which we describe separately: the eentral pore, the monomerie water pores, a side pore that we propose as an additional possible gas ehannel, and the protein–lipid interface. In all of our analyses, we define these regions as shown in Fig. 3b.

3.2.1. The central pore

Two quadruplets of hydrophobie residues, Val52 and Leu172, form the outermost doorways of the AQP1 eentral pore. Water molecules can hardly pass through these

residues and were kept away from the inside of the pore during our simulations, a behavior also revealed by other MD studies (Zhu et al., 2001; Yu et al., 2006). For gas molecules, however, the purely hydrophobic, empty central pore provides an ideal reservoir. At the end of the explicit gas diffusion simulations, 8 CO_2 and 5 O_2 molecules, respectively, were found inside the central pore, as seen in Fig. 4a and b.

As shown in Fig. 5a, PMFs calculated from both the explicit gas diffusion simulations and the implicit ligand sampling suggest that the central pore is the most favorable location for both CO_2 and O_2. However, a more favorable central pore for O_2 with a −1.7 kcal/mol energy well was predicted by implicit ligand sampling, compared to a −0.4 kcal/mol energy well revealed by the explicit gas diffusion simulations. This difference is probably caused by the limited timescale of our explicit gas diffusion simulations: while the gas distribution between the water and lipid phases is well equilibrated, the gas molecules need longer time to reach an equilibrated population inside the protein. This is especially true given that the central pore is capped by areas of relatively high energy barriers, and that the flow of gas molecules across the central pore was low compared to the gas population inside the central pore during the course of the explicit gas diffusion simulations.

According to our PMFs, the major barrier of the central pore to gas permeation is about 3.6–4.6 kcal/mol, located at the periplasmic side of the central pore

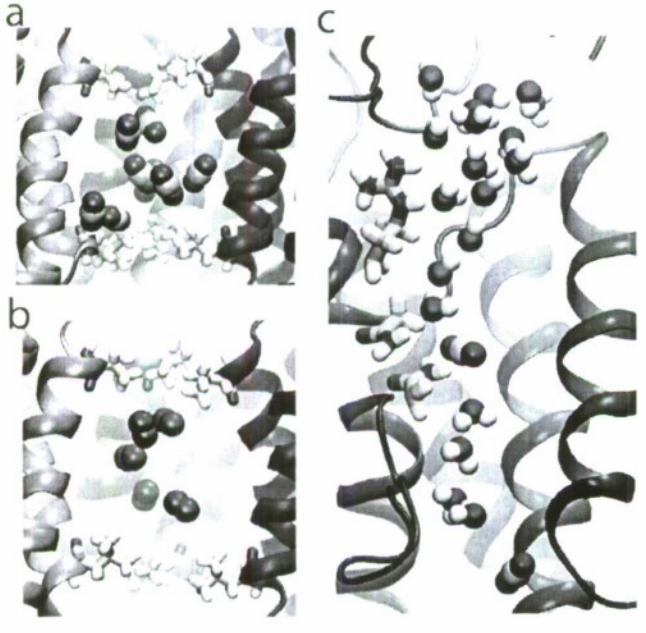

Fig. 4. (a and b) Accumulation of gas molecules inside the central pore of AQP1. At the end of the equilibrium simulations, eight CO_2 (a) and five O_2 (b) were found in the central pore, respectively. Only three AQP1 monomers are shown, with the front monomer being removed for clarity. Residues Val52 and Leu172, which form the outermost doorways of the hydrophobic central pore, are highlighted in licorice representation. (c) Snapshot showing CO_2 in one of the monomeric water pores during equilibrium simulations. Water and CO_2 molecules are shown in vdW representation. Arg197 at the SF (see text) and Asn194 and Asn78 from the NPA motifs are shown in Licorice representation.

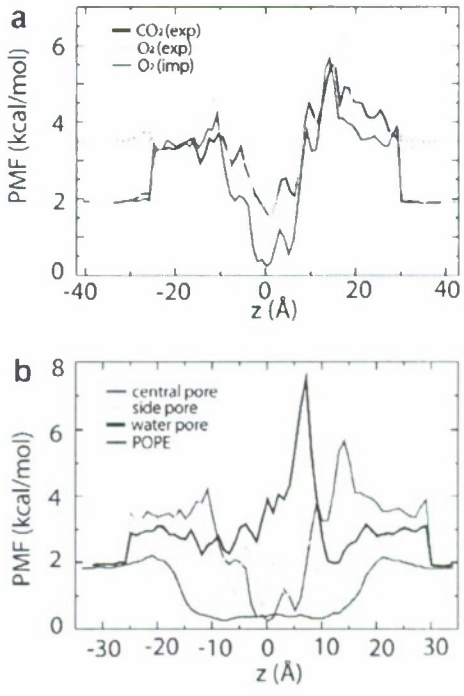

Fig. 5. (a) PMFs associated with gas permeation through the AQP1 central pore, calculated from the explicit gas diffusion simulations (exp), and implicit ligand sampling (imp). The dotted lines correspond to the PMFs of gas molecules in water of the same area as the central pore. (b) O_2 PMF calculated by implicit ligand sampling for regions shown in Fig. 3, along with the PMF in the POPE bilayer. The PMFs were computed relative to a value of 0 kcal/mol for O_2 in vacuum. In both (a) and (b) $z = 0$ is defined as the center of Asn78 and Asn194 of the NPA motifs. All PMFs were calculated assuming a density of 1 AQP1 per 50 nm^2 of bilayer, as described in Section 2. Statistical errors for CO_2 PMF (exp) and O_2 PMF (exp) are less than 0.4 kcal/mol except at the energy barriers, where due to limited sampling, the statistical errors cannot be calculated using the same formula mentioned in Section 2. The upper bound error of the PMF (imp) is +0.25 kcal/mol, the lower bound errors are −0.25, −0.6, −1.7 kcal/mol, respectively, for PMF values below 4, 6, and 8 kcal/mol (Cohen et al., 2006).

(13 Å $\leqslant z \leqslant$ 19 Å). This barrier, consistently found by both our approaches, as well as by another study (Hub and de Groot, 2006), surprisingly, does not correspond to a region that is sterically blocked directly by the protein. As shown in Fig. 6a, this barrier is located above the region of maximum protein contraction where the four hydrophobic residues Val52 reside; rather, it corresponds to a region that is populated solely by water. We have created a volumetric map of the local occupancy of water, as shown in Fig. 6b. It is clear that the barrier corresponds to a dense layer of water molecules surrounded by four aspartate (Asp50) residues (Fig. 6c). With a higher density than the bulk water, this water layer reduces the chance of gas molecules to access the central pore. If these aspartate residues will be mutated to neutral residues, e.g., alanines or asparagines, the strong electrostatic effects of the quadruplets may be eliminated and a less dense water structure could be expected, which might result in a better gas-conductive central pore of AQP1. Simulations of these mutants are currently underway.

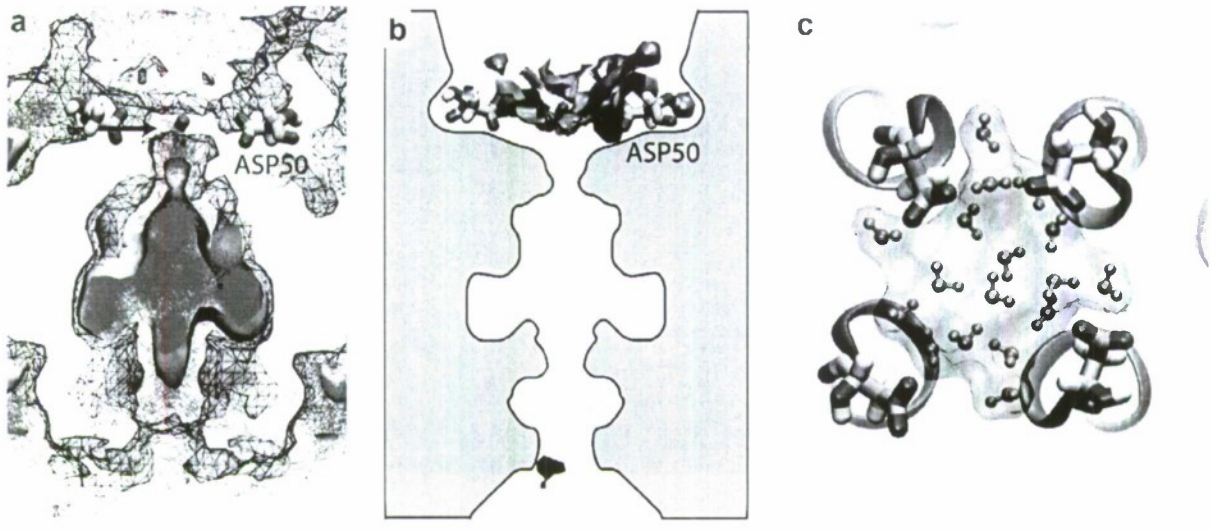

Fig. 6. (a) Close-up of the energy barrier (indicated by the black arrow) at the periplasmic mouth of the AQP1 central pore. The 0 kcal/mol (yellow) and 3 kcal/mol (black) energy isosurfaces calculated from implicit ligand sampling are shown, along with O_2 positions obtained from explicit gas diffusion simulations (red). (b) Water occupancy per $Å^3$, showing in blue the volumes occupied by water during at least 75% of the time during the 26-ns AQP1-O_2 simulation. A layer of water, denser than the bulk, is found around the Asp50 residues, corresponding to the location of the energy barrier shown in (a). Water occupancy was calculated using the volmap plugin of VMD (Humphrey et al., 1996). The profile of the central pore is shown in black lines. (c) Snapshot of water molecules around Asp50 during equilibrium simulations of AQP1-O_2. The water molecules are shown in both surface and CPK representations.

3.2.2. The water pores

Compared with the central pore, the four monomeric water pores in AQP1 were found to be less permeable to gas molecules. In our gas diffusion simulations, although both CO_2 and O_2 could enter the two vestibules of water pores and reach the NPA motifs (see Fig. 4c), no gas molecule passed through the selectivity filter (SF), *i.e.*, the narrowest part of an AQP channel. The single file of water molecules at the SF was almost always kept intact during the simulations. This may be explained by the steric barrier imposed by the protein, as well as the strong tendency of water molecules to keep their hydrogen-bonded structure; as the SF has a diameter of only ~2 Å, gas molecules could hardly pass this region without perturbing the water file, which is held strongly by hydrogen bonds between water molecules and with the protein. Using the implicit ligand sampling approach, we measured the PMF for O_2 permeation across the four water pores counted as one. As shown in Fig. 5b, the highest energy barrier is located at the SF and is found to be 5.7 kcal/mol with respect to the water solution. This is comparable with a recent study which measures a ~5.5 kcal/mol energy barrier for CO_2 permeation through the water pore of AQP1 (Hub and de Groot, 2006).

The central pore also appears to be more gas-permeable than the water pores in our induced pressure simulations. As shown in Fig. S1, the single file of water was largely disturbed when CO_2 penetrated the water pores during induced pressure simulations. In contrast, no obvious disturbance to the protein was observed when CO_2 permeated the central pore. During the induced pressure simulations, four CO_2 and six O_2 permeated the central pore, while six CO_2 and one O_2 passed through the water pores (Table 1). Given that there are four water pores, the ratio of gas permeation between the central pore and a water pore is ~3:1 for CO_2 and 24:1 for O_2. The difference between CO_2 and O_2 suggests that the water pores of AQP1 are less favorable to the more hydrophobic O_2 molecules. Indeed, in our equilibrium simulations, the probability of finding O_2 in a water pore of AQP1 is much lower than that of CO_2 (data not shown). Therefore, while CO_2 might take advantage of both the central pore and water pores to permeate AQP1, O_2 is primarily conducted through the central pore.

3.2.3. The side pores

An interesting and somewhat unexpected result of our implicit ligand sampling calculations is the identification of a favorable gas channel spanning AQP1, located between each pair of AQP1 monomers near the protein–lipid interface. These "side pores", which to our knowledge have not been considered before, have periplasmic and cytoplasmic exits which are completely enclosed inside the AQP1 tetramer. The shape of the side pores can be seen on either sides of Fig. 3a. The O_2 PMF for the four side pores (Fig. 5c) suggests that it offers low entry and exit barriers to O_2 in AQP1 along with a flat energy profile inside the pore, making it a strong candidate for a favorable gas pathway across AQP1. Furthermore, because the middle of these four pores are directly connected to the center of the lipid bilayer, the side pores can increase the rates of O_2 entry into and exit from the bilayer, further facilitating permeation across the membrane. Although no complete permeation events through the side pores were recorded in our equilibrium simulations, we observed

several half-permeation events where gas molecules entered or exited the bilayer center via these side pores.

3.2.4. Protein–lipid interface

According to both explicit gas diffusion simulations and implicit ligand sampling, the interfacial region between the AQP1 tetramer and the lipid bilayer has an increased affinity for O_2 as compared to the rest of the bilayer. Because of AQP1's uneven hydrophobic surface inside the bilayer, the packing with the lipids is not optimal, leaving plenty of room for small hydrophobic molecules. However, our 3D PMF map for O_2 indicates that the gas density in this region is localized in many disconnected pockets around the protein, and there is no single continuous pathway connecting the sides of the membrane. For this reason, while the protein–lipid interface may possibly store O_2, it does not necessarily conduct it well. As the lipids do not migrate or diffuse at the timescales probed by either of our analyses, the PMFs we observed may not be accurate and the possibility of gas permeation at the protein–lipid interface cannot be completely discounted. However, we consider high-throughput O_2 migration in this region to be unlikely on the basis of our computations.

3.2.5. AQP1 compared with POPE

Our free energy profiles revealed a higher energy barrier for gas permeation across AQP1 than a patch of POPE bilayer with the similar area. Besides the PMFs, one can compare the gas permeabilities of AQP1 and POPE in a rather straightforward way. As shown in Table 1, on average one permeation per nanosecond is observed for POPE-CO_2 and POPE-O_2 during equilibrium simulations, while few permeation events were recorded for AQP1-CO_2 and AQP1-O_2. The number of gas permeation events naturally reflects the gas permeability of the system. However, better statistics are required to meaningfully compare the AQP1-embedded membrane with the pure POPE bilayer. This was achieved by induced pressure simulations, in which gas molecules were forced to cross the membrane by an external force, and the number of gas permeation events was increased by approximately an order of magnitude, allowing us to compare the gas-permeability of the two types of membranes directly. As shown in Table 1, 203 CO_2 and 258 O_2 permeation events were observed for pure POPE bilayers, while for the AQP1-embedded membranes, the number is 80 and 83, respectively. Since all the four systems share a similar xy area, the insertion of AQP1 into the POPE bilayer has clearly reduced the total gas permeability of the membrane.

4. Conclusions

We have studied the gas permeability of AQP1 by performing MD simulations on a membrane-embedded AQP1 tetramer as well as on pure lipid bilayers. Two different approaches were used to calculate the free energy profiles associated with gas permeation through AQP1 and yielded consistent results. In general, AQP1 appears to be less gas-permeable than a patch of POPE bilayer with a similar area. However, the central pore of AQP1 is found to be permeable to both CO_2 and O_2 with a favorable energy well of -0.4 to -1.7 kcal/mol at the center and a 3.6–4.6 kcal/mol barrier on the periplasmic side. It is noteworthy that this barrier, revealed by both of our approaches, is not directly caused by the protein, but rather by a dense layer of water molecules "anchored" at the periplasmic mouth of the central pore by four aspartate residues.

Both the gas diffusion simulations and the implicit ligand sampling method suggest that the monomeric water pore of AQP1 is less gas-permeable than the central pore, likely due to the strong hydrogen bonds between the protein and water molecules inside the channel. A somewhat unexpected discovery is the identification of "side pores" located in between AQP1 monomers, which may facilitate gas conduction across the membrane. However, due to the fluctuation of the protein, these side channels might not be permanently open. It is therefore of interest and importance to further investigate the role of these side pores in gas conduction mediated by AQPs.

Our simulations suggest that aside from its conventional role as a water channel, AQP1 might provide a pathway for small, neutral gas molecules across the cellular membrane. However, compared with a patch of pure POPE bilayer with a similar area, AQP1 is less permeable to CO_2 and O_2. Therefore, gas conduction through AQP1 may be of physiological importance only in membranes with low intrinsic gas permeability or where a major fraction of the surface area of the membrane is occupied by AQPs.

Acknowledgments

The work was supported by grants from NIH (P41-RR05969, R01-GM067887). The authors gladly acknowledge supercomputer time provided by NCSA and PSC through the Large Resource Allocation Committee (MCA93S028). All molecular images are made with VMD (Humphrey et al., 1996).

Appendix A. Supplementary data

Supplementary data associated with this article can be found, in the online version, at doi:10.1016/j.jsb.2006.11.008.

References

Agre, P., 2006. The aquaporin water channels. Proc. Am. Thorac. Soc. 3, 5–13.

Agre, P., Kozono, D., 2003. Aquaporin water channels: molecular mechanisms for human diseases. FEBS Lett. 555, 72–78.

Agre, P., Bonhivers, M., Borgnia, M.J., 1998. The aquaporins, blueprints for cellular plumbing systems. J. Biol. Chem. 273, 14659–14662.

Agre, P., Nielsen, S., Ottersen, O.P., 2004. Towards a molecular understanding of water homeostasis in the brain. Neuroscience 129, 849–850.

Blank, M., Ehmke, H., 2003. Aquaporin-1 and HCO_3^-–Cl^- transporter-mediated transport of CO_2 across the human erythrocyte membrane. J. Physiol. 550, 419–429.

Borgnia, M.J., Agre, P., 2001. Reconstitution and functional comparison of purified GlpF and AqpZ, the glycerol and water channels from Escherichia coli. Proc. Natl. Acad. Sci. USA 98, 2888–2893.

Borgnia, M., Nielsen, S., Engel, A., Agre, P., 1999. Cellular and molecular biology of the aquaporin water channels. Annu. Rev. Biochem. 68, 425–458.

Burykin, A., Warshel, A., 2003. What really prevents proton transport through aquaporin? Charge self-energy versus proton wire proposals. Biophys. J. 85, 3696–3706.

Burykin, A., Warshel, A., 2004. On the origin of the electrostatic barrier for proton transport in aquaporin. FEBS Lett. 570, 41–46.

Chakrabarti, N., Tajkhorshid, E., Roux, B., Pomès, R., 2004. Molecular basis of proton blockage in aquaporins. Structure 12, 65–74.

Cohen, J., Kim, K., King, P., Seibert, M., Schulten, K., 2005. Finding gas diffusion pathways in proteins: Application to O_2 and H_2 transport in CpI [FeFe]-hydrogenase and the role of packing defects. Structure 13, 1321–1329.

Cohen, J., Arkhipov, A., Braun, R., Schulten, K., 2006. Imaging the migration pathways for O_2, CO, NO, and Xe inside myoglobin. Biophys. J. 91, 1844–1857.

Cooper, G., Boron, W., 1998. Effect of PCMBS on CO_2 permeability of Xenopus Oocytes expressing aquaporin 1 or its C189S mutant. Am. J. Physiol. 275, C1481–C1486.

Cooper, G., Zhou, Y., Bouyer, P., Grichtchenko, I., Boron, W., 2002. Transport of volatile solutes through AQP1. J. Physiol. 542, 17–29.

Darden, T., York, D., Pedersen, L., 1993. Particle mesh Ewald. An Nlog(N) method for Ewald sums in large systems. J. Chem. Phys. 98, 10089–10092.

Deen, P.M.T., van Os, C.H., 1998. Epithelial aquaporins. Curr. Opin. Cell Biol. 10, 435–442.

de Groot, B.L., Grubmüller, H., 2001. Water permeation across biological membranes: Mechanism and dynamics of aquaporin-1 and GlpF. Science 294, 2353–2357.

de Groot, B.L., Grubmüller, H., 2005. The dynamics and energetics of water permeation and proton exclusion in aquaporins. Curr. Opin. Struct. Biol. 15, 1–8.

de Groot, B.L., Frigato, T., Helms, V., Grubmüller, H., 2003. The mechanism of proton exclusion in the aquaporin-1 water channel. J. Mol. Biol. 333, 279–293.

Endeward, V., Musa-Aziz, R., Cooper, G., Chen, L., Pelletier, M., Virkki, L., Supuran, C., King, L., Boron, W., Gros, G., 2006. Evidence that Aquaporin 1 is a major pathway for CO_2 transport across the human erythrocyte membrane. FASEB J. 20, 1971–1984.

Fang, X., Yang, B., Matthay, M., Verkman, A., 2002. Evidence against aquaporin-1-dependent CO_2 permeability in lung and kidney. J. Physiol. 542, 63–69.

Feller, S.E., Zhang, Y.H., Pastor, R.W., Brooks, B.R., 1995. Constant pressure molecular dynamics simulation – the Langevin piston method. J. Chem. Phys. 103, 4613–4621.

Fujiyoshi, Y., Mitsuoka, K., de Groot, B.L., Philippsen, A., Grubmüller, H., Agre, P., Engel, A., 2002. Structure and function of water channels. Curr. Opin. Struct. Biol. 12, 509–515.

Grayson, P., Tajkhorshid, E., Schulten, K., 2003. Mechanisms of selectivity in channels and enzymes studied with interactive molecular dynamics. Biophys. J. 85, 36–48.

Hanba, Y.T., Shibasaka, M., Hayashi, Y., Hayakawa, T., Kasamo, K., Terashima, I., Katsuhara, M., 2004. Overexpression of the barley aquaporin HvPIP2;1 increases internal CO_2 conductance and CO_2 assimilation in the leaves of transgenic rice plants. Plant Cell Physiol. 45, 521–529.

Harris, J., Yung, K., 1995. Carbon dioxide's liquid-vapor coexistence curve and critical properties as predicted by a simple molecular model. J. Phys. Chem. 99, 12021–12024.

Heller, K.B., Lin, E.C., Wilson, T.H., 1980. Substrate specificity and transport properties of the glycerol facilitator of Escherichia coli. J. Bacteriol. 144, 274–278.

Herrera, M., Hong, N.J., Garvin, J.L., 2006. Aquaporin-1 transports NO across cell membranes. Hypertension 48, 157–164.

Heymann, J.B., Engel, A., 1999. Aquaporins: Phylogeny, structure, and physiology of water channels. News Physio. Sci. 14, 187–193.

Hohmann, S., Nielsen, S., Agre, P., 2001. Aquaporins. Academic Press, San Diego.

Hub, J.S., de Groot, B.L., 2006. Does CO_2 permeate through Aquaporin-1? Biophys. J. 91, 842–848.

Humphrey, W., Dalke, A., Schulten, K., 1996. VMD - Visual Molecular Dynamics. J. Mol. Graphics 14, 33–38.

Ikeda, M., Beitz, E., Kozono, D., Guggino, W.B., Agre, P., Yasui, M., 2002. Characterization of aquaporin-6 as a nitrate channel in mammalian cells. Requirement of pore-lining residue threonine 63. J. Biol. Chem. 277, 39873–39879.

Ilan, B., Tajkhorshid, E., Schulten, K., Voth, G.A., 2004. The mechanism of proton exclusion in aquaporin channels. Proteins: Struct. Funct. Bioinf. 55, 223–228.

Jensen, M.Ø., Tajkhorshid, E., Schulten, K., 2001. The mechanism of glycerol conduction in aquaglyceroporins. Structure 9, 1083–1093.

Jensen, M.Ø., Tajkhorshid, E., Schulten, K., 2003. Electrostatic tuning of permeation and selectivity in aquaporin water channels. Biophys. J. 85, 2884–2899.

Jiang, J., Daniels, B., Fu, D., 2006. Crystal structure of aqpz tetramer reveals two distinct arg-189 conformations associated with water permeation through the narrowest constriction of the water-conducting channel. J. Biol. Chem. 281, 454–460.

King, L., Agre, P., 2004. From structure to disease: The evolving tale of aquaporin biology. Nat. Rev. Mol. Cell Biol. 5, 687–698.

Li, J., Verkman, A.S., 2001. Impaired hearing in mice lacking aquaporin-4 water channels. J. Biol. Chem. 276, 31233–31237.

Liu, Z., Shen, J., Carbrey, J.M., Mukhopadhyay, R., Agre, P., Rosen, B.P., 2002. Arsenite transport by mammalian aquaglyceroporins AQP7 and AQP9. Proc. Natl. Acad. Sci. USA 99, 6053–6058.

MacKerell Jr., A.D., Bashford, D., Bellott, M., et al., 1998. All-atom empirical potential for molecular modeling and dynamics studies of proteins. J. Phys. Chem. B 102, 3586–3616.

Marrink, S., Berendsen, H., 1994. Simulation of water transport through a lipid membrane. J. Phys. Chem. 98, 4155–4168.

Moller, M., Botti, H., Batthyany, C., Rubbo, H., Radi, R., Denicola, A., 2005. Direct measurement of nitric oxide and oxygen partitioning into liposomes and low density lipoprotein. J. Biol. Chem. 280, 8850–8854.

Nakhoul, N., Davis, B., Romero, M., Boron, W., 1998. Effect of expressing the water channel aquaporin-1 on the CO_2 permeability of Xenopus oocytes. Am. J. Physiol. 274, C543–C548.

Phillips, J.C., Braun, R., Wang, W., Gumbart, J., Tajkhorshid, E., Villa, E., Chipot, C., Skeel, R.D., Kale, L., Schulten, K., 2005. Scalable molecular dynamics with NAMD. J. Comp. Chem. 26, 1781–1802.

Pohl, P., Saparov, S.M., Borgnia, M.J., Agre, P., 2001. Highly selective water channel activity measured by voltage clamp: Analysis of planar lipid bilayers reconstituted with purified AqpZ. Proc. Natl. Acad. Sci. USA 98, 9624–9629.

Prasad, G.V.T., Coury, L.A., Finn, F., Zeidel, M.L., 1998. Reconstituted aquaporin 1 water channels transport CO_2 across membranes. J. Biol. Chem. 273, 33123–33126.

Preston, G.M., Carroll, T.P., Guggino, W.B., Agre, P., 1992. Appearance of water channels in Xenopus oocytes expressing red cell CHIP28 protein. Science 256, 385–387.

Saparov, S., Tsunoda, S., Pohl, P., 2005. Proton exclusion by an aquaglyceroprotein: a voltage clamp study. Biol. Cell 97, 545–550.

Schlenkrich, M., Brickmann, J., MacKerell Jr., A.D., Karplus, M., 1996. Empirical potential energy function for phospholipids: Criteria for parameter optimization and applications. In: Merz, K.M., Roux, B. (Eds.), Biological Membranes: A Molecular Perspective from Computation and Experiment. Birkhauser, Boston, pp. 31–81.

Shinoda, W., Mikami, M., Baba, T., Hato, M., 2004. Molecular dynamics study on the effects of chain branching on the physical properties of lipid bilayers: 2. permeability. J. Phys. Chem. 108, 9346–9356.

Simon, S.A., Gutknecht, J., 1980. Solubility of carbon dioxide in lipid bilayer membranes and organic solvents. Biochim. Biophys. Acta 596, 352–358.

Subczynski, W., Hopwood, L., Hyde, J., 1992. Is the mammalian cell plasma membrane a barrier to oxygen transport? J. Gen. Physiol. 100, 69–87.

Tajkhorshid, E., Nollert, P., Jensen, M.Ø., Miercke, L.J.W., O'Connell, J., Stroud, R.M., Schulten, K., 2002. Control of the selectivity of the aquaporin water channel family by global orientational tuning. Science 296, 525–530.

Tajkhorshid, E., Aksimentiev, A., Balabin, I., Gao, M., Isralewitz, B., Phillips, J.C., Zhu, K., Schulten, F., 2003. Large scale simulation of protein mechanics and function. In: Richards, F.M., Eisenberg, D.S., Kuriyan, J. (Eds.), Advances in Protein Chemistry, vol. 66. Elsevier Academic Press, New York, pp. 195–247.

Tajkhorshid, E., Cohen, J., Aksimentiev, A., Sotomayor, M., Schulten, K., 2005a. Towards understanding membrane channels. In: Martinac, B., Kuhalski, A. (Eds.), Bacterial Ion Channels and Their Eukaryotic Homologues. ASM Press, Washington, DC, pp. 153–190.

Tajkhorshid, E., Zhu, F., Schulten, K., 2005b. Kinetic theory and simulation of single-channel water transport. In: Yip, S. (Ed.), Handbook of Materials Modeling, Methods and Models, vol. 1. Springer, Netherlands, pp. 1797–1822.

Tamimi, A., Rinker, E.B., Sandall, O.C., 1994. Diffusion coefficients for hydrogen sulfide, carbon dioxide, and nitrous oxide in water over the temperature range 293–368 K. J. Chem. Eng. Data 39, 330–332.

Terashima, I., Ono, K., 2002. Effects of $HgCl_2$ on CO_2 dependence of leaf photosynthesis: Evidence indicating involvement of aquaporins in CO_2 diffusion across the plasma membrane. Plant Cell Physiol. 43, 70–78.

Törnroth-Horsefield, S., Wang, Y., Hedfalk, K., Johanson, U., Karlsson, M., Tajkhorshid, E., Neutze, R., Kjellbom, P., 2006. Structural mechanism of plant aquaporin gating. Nature 439, 688–694.

Uehlein, N., Lovisolo, C., Siefritz, F., Kaldenhoff, R., 2003. The tobacco aquaporin NtAQP1 is a membrane CO_2 pore with physiological functions. Nature 425, 734–737.

Verkman, A., 2002. Does aquaporin-1 pass gas? An opposing view. J. Physiol. 542, 31.

Wang, Y., Schulten, K., Tajkhorshid, E., 2005. What makes an aquaporin a glycerol channel: A comparative study of AqpZ and GlpF. Structure 13, 1107–1118.

Yang, B., Fukuda, N., van Hoek, A., Matthay, M.A., Ma, T., Verkman, A.S., 2000. Carbon dioxide permeability of aquaporin-1 measured in erythrocytes and lung of aquaporin-1 null mice and in reconstituted proteoliposomes. J. Biol. Chem. 275, 2682–2692.

Yool, A.J., Weinstein, A.M., 2002. New roles for old holes: Ion channel function in aquaporin-1. News Physio. Sci. 17, 68–72.

Yu, J., Yool, A.J., Schulten, K., Tajkhorshid, E., 2006. Mechanism of gating and ion conductivity of a possible tetrameric pore in Aquaporin-1. Structure 14, 1411–1423.

Zhu, F., Tajkhorshid, E., Schulten, K., 2001. Molecular dynamics study of aquaporin-1 water channel in a lipid bilayer. FEBS Lett. 504, 212–218.

Zhu, F., Tajkhorshid, E., Schulten, K., 2002. Pressure-induced water transport in membrane channels studied by molecular dynamics. Biophys. J. 83, 154–160.

Zhu, F., Tajkhorshid, E., Schulten, K., 2004. Theory and simulation of water permeation in aquaporin-1. Biophys. J. 86, 50–57.

Relative CO_2/NH_3 selectivities of AQP1, AQP4, AQP5, AmtB, and RhAG

Raif Musa-Aziz[a,b,1,2], Li-Ming Chen[a,b,2], Marc F. Pelletier[a,c], and Walter F. Boron[a,b,1]

[a]Department of Cellular and Molecular Physiology, Yale University School of Medicine, New Haven, CT 06520; [c]Aeromics, LLC, Cleveland, OH 44106; and [b]Department of Physiology and Biophysics, Case Western Reserve University, Cleveland, OH 44106

Communicated by Gerhard Giebisch, Yale University School of Medicine, New Haven, CT, December 30, 2008 (received for review November 18, 2008)

The water channel aquaporin 1 (AQP1) and certain Rh-family members are permeable to CO_2 and NH_3. Here, we use changes in surface pH (pH_S) to assess relative CO_2 vs. NH_3 permeability of *Xenopus* oocytes expressing members of the AQP or Rh family. Exposed to CO_2 or NH_3, AQP1 oocytes exhibit a greater maximal magnitude of pH_S change (ΔpH_S) compared with day-matched controls injected with H_2O or with RNA encoding SGLT1, NKCC2, or PepT1. With CO_2, AQP1 oocytes also have faster time constants for pH_S relaxation (τ_{pH_S}). Thus, AQP1, but not the other proteins, conduct CO_2 and NH_3. Oocytes expressing rat AQP4, rat AQP5, human RhAG, or the bacterial Rh homolog AmtB also exhibit greater $\Delta pH_S(CO_2)$ and faster τ_{pH_S} compared with controls. Oocytes expressing AmtB and RhAG, but not AQP4 or AQP5, exhibit greater $\Delta pH_S(NH_3)$ values. Only AQPs exhibited significant osmotic water permeability (P_f). We computed channel-dependent (*) ΔpH_S or P_f by subtracting values for H_2O oocytes from those of channel-expressing oocytes. For the ratio $\Delta pH_S(CO_2)^*/P_f^*$, the sequence was AQP5 > AQP1 ≅ AQP4. For $\Delta pH_S(CO_2)^*/\Delta pH_S(NH_3)^*$, the sequence was AQP4 ≅ AQP5 > AQP1 > AmtB > RhAG. Thus, each channel exhibits a characteristic ratio for indices of CO_2 vs. NH_3 permeability, demonstrating that, like ion channels, gas channels can exhibit selectivity.

gas channel | oocyte | permeability | signal peptide | surface pH measurement

Gas transport through membranes is of fundamental importance for nutritive transport, photosynthesis, oxidative metabolism, and signaling. For most of the past century, we assumed that gas molecules cross biological membranes merely by diffusing through the lipid phase. This dogma was challenged by 2 observations: (*i*) Apical membranes of gastric-gland cells have no demonstrable permeability to CO_2 or NH_3 (1). (*ii*) Heterologous expression of the water channel aquaporin 1 (AQP1) increases the CO_2 permeability of *Xenopus* oocytes (2). Cooper and Boron (3) and Prasad *et al.* (4) confirmed and extended this observation. Uehlein (5) showed that an AQP plays a physiological role by enhancing CO_2 uptake by plants. Endeward *et al.* (6) demonstrated that AQP1 accounts for ≈60% of the CO_2 permeability of human red blood cells (RBCs). Molecular dynamics simulations suggest that CO_2 can pass through the 4 aquapores of an AQP1 tetramer (7) and especially through the central pore between the 4 monomers (7). Additional data indicate that AQP1 is permeable to nitric oxide (8), and that—when expressed in *Xenopus* oocytes (9, 10) or when reconstituted into planar lipid bilayers (11)—AQP1, AQP3, AQP8, AQP9, and the plant aquaporin TIP2;1 are all permeable to NH_3.

The AmtB/MEP/Rh proteins represent a second family of gas channels (12–15). Early work showed that AmtB and MEP transport NH_3 or NH_4^+, thereby playing a nutritive role in archaea, bacteria, and fungi (16, 17). The crystal structures of the bacterial AmtB (18–20) and Rh50 (21) and the fungal Amt-1 (22) are consistent with the idea that NH_3 passes through a pore in each monomer of the homotrimer. Indeed, reconstituted AmtB conducts NH_3 (14), and RhAG is necessary for NH_3 transport in mammalian RBCs (23). Soupene *et al.* found that Rh1 deficiency impairs the growth of the green alga *C. reinhardtii* (24) and suggested that Rh1 plays a role in CO_2 transport. In RBCs, RhAG accounts for ≈50% of CO_2 transport (25).

In 2006, we introduced an approach (6) to assess CO_2 transport by pushing a blunt microelectrode against the surface of an oocyte, while monitoring surface pH (pH_S). Introducing extracellular CO_2 causes a transient pH_S increase, the maximum magnitude of which (ΔpH_S) is an index of maximal CO_2 influx. Earlier, De Hemptinne and Huguenin (26) had observed such a CO_2-induced transient while monitoring extracellular pH (pH_o) of rat soleus muscle. Moreover, Chesler (27) had found that exposing lamprey neurons to NH_3 causes a transient decreases in pH_o. Here, we exploit CO_2- and NH_3-induced pH_S transients to study the CO_2 vs. NH_3 permeability of 4 channels abundantly expressed in cells that mediate high rates of gas transport: human AQP1 (RBCs; ref. 28), the M23 variant of rat AQP4 (astrocytic endfeet at the blood–brain barrier, ref. 29), rat AQP5 (alveolar type I pneumocytes; ref. 30), and human RhAG (RBCs, ref. 31). We also studied bacterial AmtB. Our results show that all 5 channels are permeable to CO_2, and all but AQP4 and AQP5 are permeable to NH_3. A relative index of CO_2/NH_3 permeability varied widely: AQP4 ≅ AQP5 > > AQP1 > AmtB > RhAG. Thus, as is true for ion channels, gas channels exhibit substantial solute selectivity, which could play an important physiological role in controlling gas fluxes.

Results

pH_S Transients Caused by Applying CO_2 vs. NH_3. Fig. 1*A* illustrates schematically how the influx of CO_2 leads to a fall in $[CO_2]$ near the extracellular surface of the membrane ($[CO_2]_S$), which in turn leads to a rise in pH_S. Fig. 1*B* shows how the influx of NH_3 leads to a fall in pH_S. As described in ref. 6, exposing an AQP1-expressing oocyte to a solution containing 5% CO_2/33 mM HCO_3^- at a constant pH of 7.50 causes a transient rise in pH_S, followed by an exponential decay (Fig. 1*C Left*, green record). After the washout of CO_2 (see *SI Text* and Fig. S3), exposing the same oocyte to 0.5 mM NH_3/NH_4^+ causes a transient fall in pH_S (Fig. 1*C Right*, green record), as noted elsewhere (32). Additional data are consistent with the hypothesis that *Xenopus* oocytes handle NH_3 in an unusual way, sequestering most incoming NH_3 in an intracellular compartment as NH_4^+ (32).

The maximal pH_S transients are much smaller in day-matched oocytes injected with H_2O (orange) or cRNA encoding the Na/glucose cotransporter SGLT1 (black), and are totally lacking

Author contributions: R.M.-A., L.-M.C., M.F.P., and W.F.B. designed research; R.M.-A., L.-M.C., and M.F.P. performed research; R.M.-A. analyzed data; and R.M.-A., L.-M.C., and W.F.B. wrote the paper.

The authors declare no conflict of interest.

[1]To whom correspondence may be addressed. E-mail: raif.aziz@case.edu or walter.boron@case.edu.

[2]R.M.-A. and L.-M.C. contributed equally to this work.

This article contains supporting information online at www.pnas.org/cgi/content/full/0813231106/DCSupplemental.

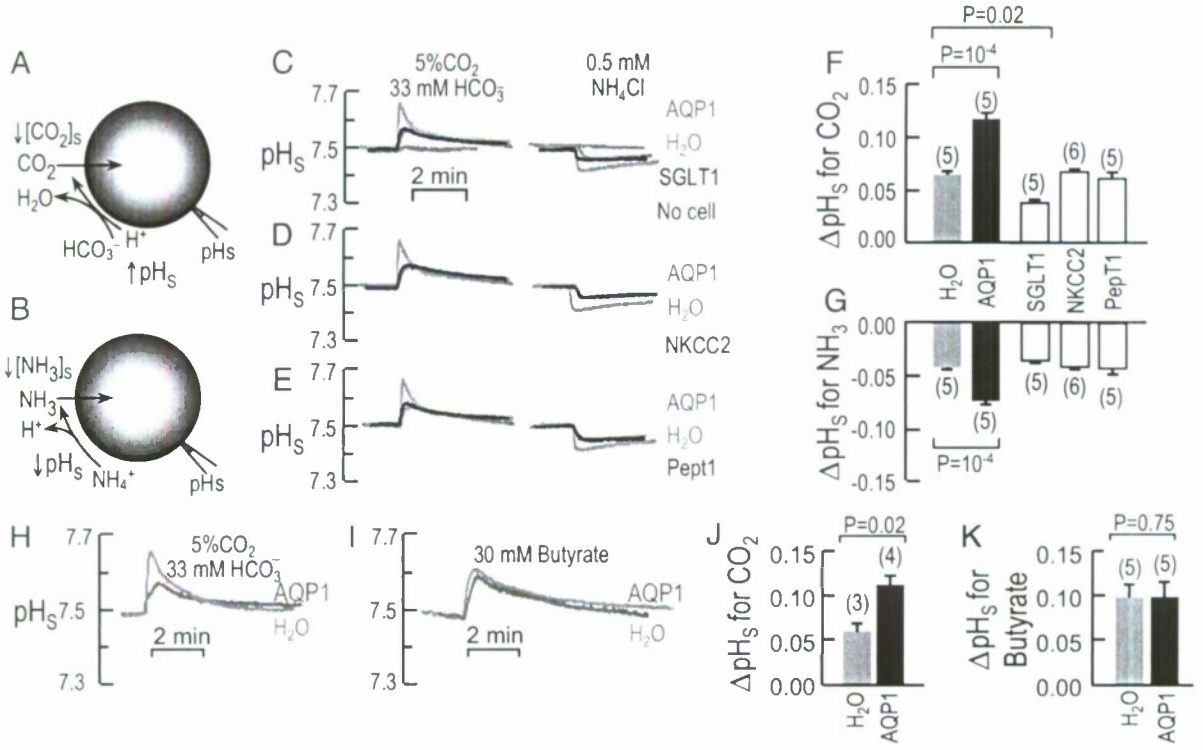

Fig. 1. Basis of surface pH changes. (*A*) CO_2 influx. At the outer surface of the membrane, the CO_2 influx creates a CO_2 deficit. The reaction $HCO_3^- + H^+ \rightarrow CO_2 + H_2O$, in part, replenishes the CO_2, raising pH_S. (*B*) NH_3 influx. The reaction $NH_4^+ \rightarrow NH_3 + H^+$, in part, replenishes NH_3, lowering pH_S. (*C–E*) Representative pH_S transients from oocytes injected with H_2O or expressing AQP1 (record repeated in the 3 images), SGLT1, NKCC2, or PepT1. All data in *C–E* were obtained on the same day, from the same batch of oocytes, exposed first to CO_2/HCO_3^- and then (after CO_2 removal) to NH_3/NH_4^+. Also shown in C are records with no oocyte present. Before and after solution changes, we retracted the pH electrode to the bulk extracellular solution (pH 7.50) for calibration. (*F* and *G*) Summary of extreme excursions of pH_S (ΔpH_S) for CO_2 and NH_3 data. (*H* and *I*) Representative pH_S transients from day-matched H_2O or AQP1 oocytes exposed to CO_2/HCO_3^- or 30 mM butyrate. (*J* and *K*) Summary of ΔpH_S for experiments like those in *H* or *I*. Values are means ± SE, with numbers of oocytes in parentheses. For *F* and *G*, statistical comparison between H_2O-injected controls and other oocytes (separately for CO_2 and NH_3 data) were made using a 1-way ANOVA for 5 groups, followed by Dunnett's multiple comparison. ΔpH_S values for H_2O, NKCC2, and PepT1 do not differ from one other. For *J* and *K*, statistical comparisons were made using unpaired 2-tailed *t* tests.

in the absence of an oocyte (gray). Moreover, oocytes expressing the Na/K/Cl cotransporter NKCC2 or the H/oligopeptide cotransporter PepT1 have ΔpH_S values similar to those of H_2O-injected oocytes (Fig. 1 *D* and *E*).

Fig. 1 *F* and *G* summarize ΔpH_S data for a larger number of experiments like those in Fig. 1 *C–E* and show that ΔpH_S for AQP1 is significantly greater than for all other oocyte groups. As expected, the time constant (τ_{pH_S}) for the decay of pH_S from its peak, an index of the time required for CO_2 to equilibrate across the membrane, has a pattern that is the inverse of that for ΔpH_S (Fig. S1 *A* and *B*). Because of the oocyte's unusual NH_3 handling, the pH_S relaxation during NH_3 exposures is prolonged, precluding the calculation of a τ_{pH_S} for NH_3. In the CO_2 protocol, the smaller ΔpH_S for SGLT1 vs. H_2O oocytes could reflect a decrease in the expression of other proteins or an increase in membrane–protein/lipid ratio.

Given our observations with CO_2, one might ask whether AQP1 also would enhance the flux of a permeant weak acid like butyric acid (33). While confirming that AQP1 increases the ΔpH_S in oocytes exposed to CO_2 (Fig. 1 *H* and *J*), we found that the channel has no effect either on ΔpH_S (Fig. 1 *I* and *K*) or τ_{pH_S} (Fig. S1 *C* and *D*) in oocytes exposed to butyric acid.

In principle, AQP1 could enhance the CO_2-induced pH_S spike in Fig. 1 *C* or *H*, not because AQP1 is a CO_2 channel, but because it has unanticipated carbonic anhydrase (CA) activity and thus catalyzes the extracellular reaction $HCO_3^- + H^+ \rightarrow CO_2 + H_2O$ (see Fig. 1*A*). To test the CA hypothesis, we injected oocytes with cRNA encoding CA IV, coupled via a GPI linkage to the outer surface of the membrane. Increased CA-IV expression causes a graded increase in ΔpH_S (Fig. S2), and we determined the dose of CA-IV cRNA that produces the same ΔpH_S as a typical AQP1 oocyte. Fig. 2 shows that membrane preparations of oocytes injected with this dose of CA-IV cRNA, compared with those from H_2O oocytes, require a much shorter time to achieve a pH endpoint in a CA assay. However, membrane preparations of AQP1 oocytes are indistinguishable from those

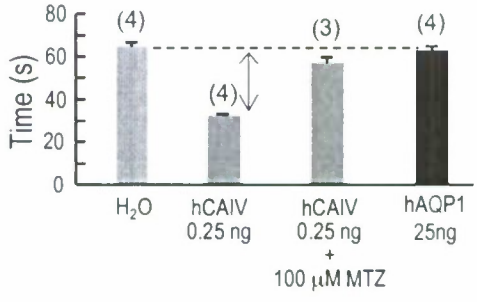

Fig. 2. Carbonic anhydrase activities of *Xenopus* oocytes. CA activity was determined from membrane preparations of 100 oocytes injected with H_2O, 0.25 ng of cRNA encoding hCA IV, or 25 ng of cRNA encoding hAQP1. We divided each membrane preparation into aliquots containing 20 μg of total protein and performed a colorimetric CA assay on each aliquot (see *SI Text*). The sample mixtures containing CA-IV were run ± 100 μM methazolamide (MTZ), a CA inhibitor. Each N refers to a CA assay on 1 aliquot.

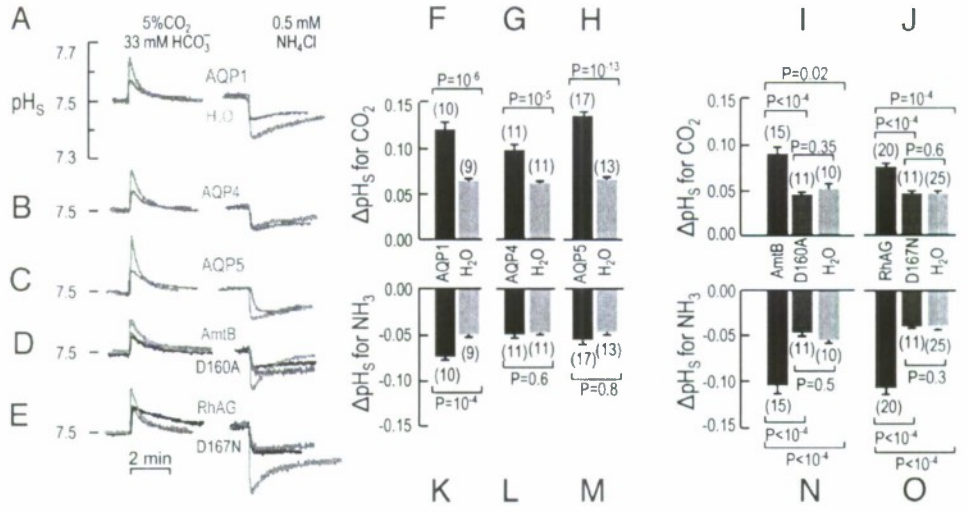

Fig. 3. Surface pH changes caused by CO_2 and NH_3 influx in oocytes expressing gas-channel proteins. (*A–E*) Typical pH_S transients from oocytes injected with H_2O or expressing AQP1, AQP4, AQP5, WT AmtB or its inactive D160A mutant, or WT RhAG or its inactive D167A mutant. The protocol was the same as in Fig. 1. (*F–J*) Summary of extreme excursions of pH_S (ΔpH_S) caused by CO_2 influx. Each image represents mean values for day-matched oocytes. (*K–O*) Summary of ΔpH_S caused by NH_3 influx. Each image (*F–O*) represents mean values for day-matched oocytes. Some H_2O oocytes served as controls in more than 1 panel (total number of H_2O oocytes: 54 for CO_2, 61 for NH_3). Values are means ± SE, with numbers of oocytes in parentheses. For *F–H* and *K–M*, statistical comparisons were made using unpaired 2-tailed *t* tests. For *I* and *J* and *N* and *O*, statistical comparisons were made using 1-way ANOVAs for 3 groups, followed by Student–Newman–Keuls analyses.

of H_2O, allowing us to rule out the CA hypothesis. Thus, on the basis of ΔpH_S and τ_{pH_S} measurements, AQP1, but not SGLT1, NKCC1, and PepT1, acts as a channel for CO_2 and NH_3.

Comparison of AQPs with AmtB and RhAG. Using the same protocol shown in Fig. 1 *C–E*, we systematically examined the effects of sequential exposures to CO_2/HCO_3^- and then NH_3/NH_4^+ on oocytes expressing AQP1, AQP4, AQP5, AmtB, or RhAG. Fig. 3*A* shows again that CO_2 and NH_3 elicit larger pH_S spikes in AQP1 (green) than in day-matched H_2O (orange) oocytes. Both AQP4 (Fig. 3*B*) and AQP5 (Fig. 3*C*) enhance the pH_S spike with CO_2 but not with NH_3. Both AmtB (Fig. 3*D*) and RhAG (Fig. 3*E*) enhance the pH_S spike with CO_2 but are especially effective with NH_3. Asp^{160} is vital for AmtB activity (19, 34), and the homologous Asp^{167} is required by RhAG (35). We found that the inactive D160A mutant of AmtB (34, 36) and the inactive D167N mutant of RhAG (35) are inactive as either CO_2 or NH_3 channels, presumably because the mutations cause major structural changes (35). Figs. S3 and S4 *A* and *D* show full-length experiments similar to those in Fig. 3 *A–E*.

In the above experiments, all AmtB and RhAG constructs were C-terminally tagged with EGFP (enhanced GFP), and fluorescence measurements confirmed trafficking to near the oocyte surface. The tagged and untagged constructs yielded identical results in pH_S assays (Fig. S4).

Fig. 3 *F–J* are analogous to Fig. 1*F*, except that in Fig. 3 *F–J*, we pair each oocyte expressing a WT or mutant channel with its day-matched H_2O-injected control. Each WT protein yields a ΔpH_S that is significantly greater than the H_2O control or (as applicable) the mutant protein. Moreover, the ΔpH_S values of the mutants are not different from the corresponding H_2O oocytes. Fig. 3 *K–O* is a summary of the NH_3 data. The results are comparable to the CO_2 data, except that the magnitudes of ΔpH_S for AQP4 and AQP5 in the NH_3 protocol are not different from those of their corresponding H_2O-injected controls. Fig. S5 shows that the relationship for the τ_{pH_S} values is the inverse of that for the ΔpH_S values in Fig. 3. Thus, each of the proteins, AQP1, AQP4, AQP5, AmtB, and RhAG, is permeable to CO_2. Moreover, AQP1, AmtB, and RhAG, but not AQP4 or AQP5, are permeable to NH_3.

Cleavage of AmtB Signal Peptide by Oocytes. Our AmtB cDNA encodes a signal peptide that *Escherichia coli* naturally cleaves (37), so that the new N terminus is extracellular. The A22K point mutation in AmtB prevents the cleavage in *E. coli*, although the mutant AmtB still forms trimers and is active (37). To verify that *Xenopus* oocytes also cleave the signal peptide, we added a C-terminal His tag to WT AmtB, A22K-AmtB, and an AmtB variant with the signal peptide truncated. Fig. 4 shows Western blots of plasma-membrane preparations from oocytes expressing the 3 constructs. The molecular mass of the major band of WT AmtB is appropriately less than that of A22K-AmtB, but the same as truncated AmtB. Thus, oocytes do indeed cleave the signal peptide of WT AmtB. Densitometry indicates that >90% of the AmtB in oocytes is appropriately cleaved. Additional data reveal that AmtB-His is active as both a CO_2 and an NH_3 channel.

P_f in Oocytes Expressing Different Channels. So that we could relate our CO_2 and NH_3 data to the wealth of information on the osmotic water permeability (P_f) of AQP-expressing oocytes, we determined P_f for each AQP oocyte and its day-matched control from the dataset in Fig. 3. As summarized by the 3 pairs of bars on the left side of Fig. 5, the mean P_f value for each AQP was significantly and substantially greater than the matched controls. We separately assessed P_f for matched oocytes expressing AQP1,

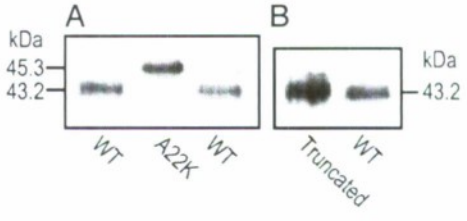

Fig. 4. Western blots testing cleavage of the AmtB signal peptide in *Xenopus* oocytes. (*A*) Wild-type AmtB vs. uncleavable A22K mutant. (*B*) Wild-type AmtB vs. AmtB with truncated signal peptide. Data are representative of 4 similar experiments. All constructs were His tagged at the C terminus and detected with an anti-His antibody.

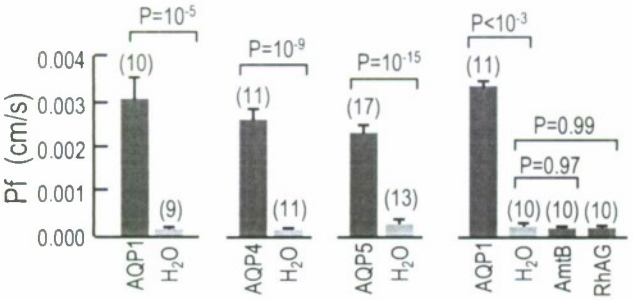

Fig. 5. Osmotic water permeabilities of *Xenopus* oocytes. P_f (cm/s) of oocytes injected with H_2O or cRNA encoding AQP1, AQP4, AQP5, AmtB, or RhAG. Values are means ± SE, with numbers of oocytes in parentheses. Statistical comparison between H_2O vs. AQP oocytes were made using unpaired 2-tailed *t* tests. Statistical comparisons among the 4 groups were made using a 1-way ANOVA, followed by Student–Newman–Keuls analyses.

AmtB, or RhAG vs. day-matched H_2O oocytes. The right side of Fig. 5 shows that only for AQP1 oocytes was the mean P_f value significantly greater than that for H_2O oocytes; the P_f values for H_2O, AmtB, and RhAG oocytes were not significantly different from one another. Thus, despite the hypothesized presence of H_2O in the NH_3 pore of AmtB (20, 22), the 2 Rh proteins do not function as water channels.

Discussion

Channel-Dependent ΔpH_S and P_f Values. Given our experimental design, the magnitude of ΔpH_S is a semiquantitative index of both the flux of, and membrane permeability to, CO_2 or NH_3. For CO_2, the same is true of τ_{pH_S}. Note that the quantitative relationship between ΔpH_S on the one hand and absolute flux or permeability on the other is likely to be different for CO_2 vs. NH_3. The portion of the CO_2-induced ΔpH_S signal that we can ascribe to a particular channel is the difference between the ΔpH_S of each channel-expressing oocyte (e.g., green record in Fig. 3*A*) and the ΔpH_S of its day-matched H_2O-injected control (e.g., orange record in Fig. 3*A*). Fig. 6*A* summarizes these differences, the channel-dependent signal $(\Delta pH_S^*)_{CO2}$, for the CO_2 data, computed oocyte by oocyte. Similarly, Fig. 6*B* summarizes the analogous differences, the channel-specific signal $(\Delta pH_S^*)_{NH3}$, for the NH_3 data. Note that the mean $(\Delta pH_S^*)_{NH3}$ values for AQP4 and AQP5 are not significantly different from zero.

Ratios of Indices of Permeability. Because we do not know the number of AQP molecules at the plasma membrane in each oocyte, it is impossible to normalize our $(\Delta pH_S^*)_{CO2}$ or $(\Delta pH_S^*)_{NH3}$ data to protein abundance. However, for each AQP oocyte, we also have a channel-dependent P_f (P_f^*), summarized in Fig. 6*C*. For each oocyte, we divided $(\Delta pH_S^*)_{CO2}$ or $(\Delta pH_S^*)_{NH3}$ by P_f^*. Fig. 6*D* summarizes these mean values, which represent semiquantitative indices of the CO_2/H_2O or NH_3/H_2O permeability ratios. By a factor of 2, AQP5 has the highest $(\Delta pH_S^*)_{CO2}/P_f^*$, and the values for AQP1 and AQP4 are indistinguishable.

Because we have both $(\Delta pH_S^*)_{CO2}$ and $(\Delta pH_S^*)_{NH3}$ for each of a large number of oocytes, it is also possible to compute the ratio $(\Delta pH_S^*)_{CO2}/(\Delta pH_S^*)_{NH3}$, a relative index of the CO_2/NH_3 permeability ratio, for AQP1, AmtB, and RhAG. Fig. 6*E* summarizes these values. Because $(\Delta pH_S^*)_{NH3}$ for AQP4 and AQP5 do not differ from zero, the ratios for these proteins are theoretically infinite. Thus, among the channels tested, AQP4 and AQP5 have the highest CO_2/NH_3 permeability ratios, followed by AQP1, AmtB, and RhAG. Conversely, RhAG has the highest NH_3/CO_2 permeability ratio (see Fig. S6).

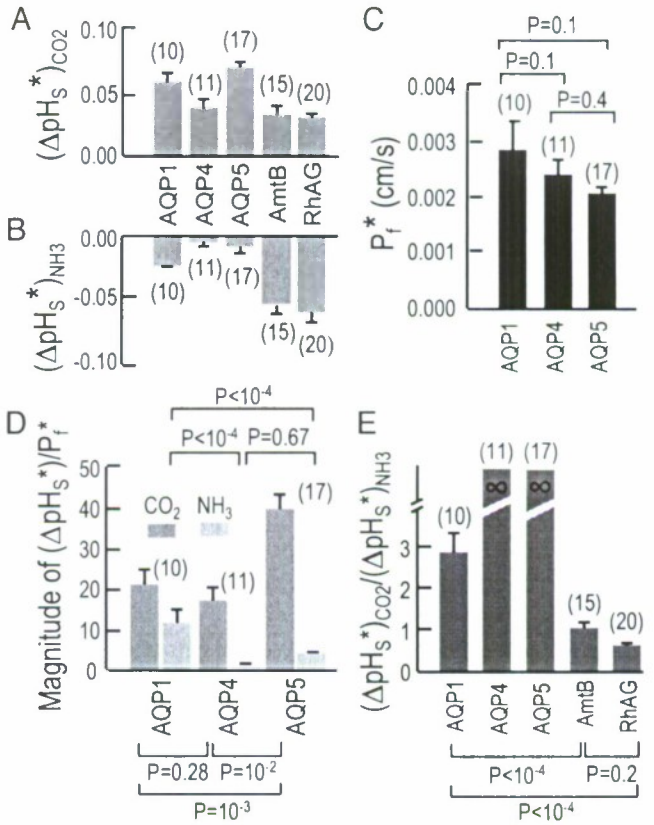

Fig. 6. Comparison of channel-dependent properties. (*A*) Indices of channel-dependent CO_2 permeability. For each ΔpH_S from a channel-expressing oocyte, we subtracted the mean, day-matched ΔpH_S for H_2O oocytes. Bars represent mean subtracted values, the channel-dependent ΔpH_S for CO_2, or $(\Delta pHS^*)_{CO2}$. Note: Oocytes in *A* are the same as those in *B* and *C*. (*B*) Indices of channel-dependent NH_3 permeability. We computed $(\Delta pH_S^*)_{NH3}$ using the same approach as in *A*. (*C*) Channel-dependent water permeabilities. For each P_f from a channel-expressing oocyte, we subtracted the mean, day-matched P_f for H_2O oocytes. Bars represent mean subtracted values, the channel-dependent P_f, or P_f^*. (*D*) Indices of channel-dependent CO_2 and NH_3 permeability, normalized to P_f^*. For each oocyte, we divided $(\Delta pH_S^*)_{CO2}$ and $(\Delta pH_S^*)_{NH3}$ by its P_f^*. (*E*) Indices of gas selectivity. For each oocyte expressing AQP1, AmtB, or RhAG, we divided $(\Delta pH_S^*)_{CO2}$ by $-(\Delta pH_S^*)_{NH3}$. Because $(\Delta pH_S^*)_{NH3}$ was not significantly different from zero for oocytes expressing AQP4 or AQP5, we represent these ratios as "infinity." Statistical comparisons were made using 1-way ANOVAs for 3 groups, followed by Student–Newman–Keuls analyses.

Thus, compared with the AQPs tested, the Rh-like proteins tested are relatively more selective for NH_3, whereas the AQPs are relatively more selective for CO_2.

Significance. Our data demonstrate that channel proteins can exhibit gas selectivity by channel proteins. The basis of the selectivity is probably not the size of the transiting molecules—H_2O, CO_2, and NH_3 have similar minimum diameters—but rather their chemistries and the chemistries of the monomeric pores vs. the pore at the center of the multimers. The electronic configuration of NH_3 is identical to that of H_2O, which moves exclusively through the monomeric aquapores of AQP1. Thus, the hydrophilic NH_3 probably also moves exclusively through the monomeric aquapores of AQP1 and through the monomeric ammonia pores of AmtB and RhAG. The less hydrophilic CO_2, however, could move through the hydrophobic central pores of all 5 channels. NO is also known to move through AQP1 (8), and indirect evidence is consistent with the idea that O_2 moves

through AQP1 (38). We suggest that the hydrophobic NO and O_2 move through the central pores. Crystallographic data show that xenon can enter the central pore of the bacterial Rh50 (21). Moreover, in the case of AQP1, molecular-dynamics simulations show that CO_2 could penetrate the 4 aquapores or, with greater ease, the central pore (7). We hypothesize that the CO_2/NH_3 selectivities that we observe reflect the relative permeabilities of the 2 gases through the monomeric vs. the central pores of the 5 channels we studied.

In a cell like the human RBC, whose plasma-membrane lipid has an intrinsically low gas permeability (6), the gas selectivity of AQP1 and the Rh complex would provide control over dissolved gases crossing the membrane. The NH_3 permeability of AQP1 and RhAG could enhance the ability of RBCs to pick up NH_3 in various tissues (where the NH_3 gradient would favor NH_3 uptake) and then to off-load it in the liver (where the gradient would favor NH_3 efflux from RBCs and uptake by hepatocytes) for NH_3 detoxification. In the hypertonic renal medulla, this NH_3 permeability could reduce the reflection coefficient for NH_3 and thereby reduce cell-volume changes. However, the low NH_3 permeability of AQP4 could protect the brain from rising blood levels of NH_3, while still allowing CO_2, and perhaps NO and O_2, to pass.

Materials and Methods

Molecular Biology. *AQPs.* Human AQP1 cDNA (GenBank accession no. NM_198098), cDNA encoding the rat AQP4/M23 splice variant (GenBank accession no. NM_012825), and human AQP5 cDNA (GenBank accession no. NM_012779) were gifts of Peter Agre (Johns Hopkins University, Baltimore). *AmtB.* We cloned *E. coli* AmtB cDNA (GenBank accession no. ECU40429) by PCR from genomic DNA and subcloned the ~1.3-kb PCR product into the *Xenopus* expression vector pGH19 (39). Using PCR, we created an additional construct in which we replaced the nucleotides encoding the signal sequence (i.e., first 22 residues) with ATG. At the 3′ end of some constructs, we added in-frame cDNA encoding either EGFP (Clontech, ref. 40) or a His tag. *RhAG.* Human RhAG cDNA in pT7T5 (GenBank accession no. NM_000324, a gift of Baya Chérif-Zahar, Université René Descartes, INSERM, Paris) (41) was subcloned into pGH19. We tagged RhAG at its 3′ end with EGFP. *Other cDNAs.* Rabbit NKCC2 (42) was a gift of Biff Forbush (Yale University, New Haven, CT). SGLT1 (43) and PepT1 (44) were gifts of Matthias Hediger (Brigham and Women's Hospital and Harvard Medical School, Boston).

Site-Directed Mutagenesis. We used the QuikChange Site-Directed Mutagenesis Kit (Stratagene), following the manufacturer's instructions.

cRNA Preparation. We generated cRNA using the Message Machine kit (Ambion) and, unless otherwise stated, injected oocytes with 50 nL of 0.5 ng/nL of cRNA or 25 nL of 1 ng/nL of cRNA.

Western Blot Analysis. Plasma-membrane proteins were prepared from oocytes (45), separated on a 13% SDS polyacrylamide gel, blotted on a PVDF membrane, probed with a monoclonal anti-His antibody (Catalog no. 70796–3, Novagen), and detected using ECL plus Western Blotting Detection Reagents (Amersham Biosciences).

Solutions for Physiological Assays. The ND96 solution contained: 96 mM NaCl, 2 mM KCl, 1 mM $MgCl_2$, 1.8 mM $CaCl_2$, and 5 mM Hepes, pH 7.50, osmolality 195 mOsm. For P_f assays, we used a hypotonic ND96 variant (100 mOsm) that contained only 43 mM NaCl. The CO_2/HCO_3^- solution was identical to ND96 except that 33 mM $NaHCO_3$ replaced 33 mM NaCl, and the solution was bubbled with 5% CO_2/balance O_2. The NH_3/NH_4^+ solution was a variant of ND96 in which we replaced 0.5 mM NaCl with 0.5 mM NH_4Cl. The butyrate solution was a variant of ND96 in which we replace 30 mM Na-butyrate with 30 mM NaCl.

Carbonic-Anhydrase Assay. Carbonic-anhydrase activity was assessed in 20 μg of membrane preparation of CA-IV or AQP1 oocytes using a colorimetric technique (46). The assay measures the rate at which the pH of a weakly buffered alkaline solution (imidazole-Tris, 50% CO_2, with p-nitrophenol as indicator at 0 °C), falls in the presence or absence of CA, noted by a color change from yellow to clear, due to the reaction $CO_2 + H_2O \rightarrow HCO_3^- + H^+$.

Measurement of Oocyte Water Permeability. We used a volumetric assay (47, 48) to measure osmotic water permeability (P_f). Briefly, after dropping oocytes into a Petri dish containing the hypotonic solution, we acquired video images every 1–2 s, obtaining the time course of the projection area of the oocyte. Assuming the oocyte to be a sphere, and the true surface area (S) to be 8-fold greater than the idealized area (49), we computed P_f as:

$$P_f = \frac{V_o \cdot \frac{d(V/V_o)}{dt}}{S \cdot \Delta Osm \cdot V_w}$$

where V_o is initial oocyte volume, $d(V/V_o)/dt$ is the maximal fractional rate of volume increase, ΔOsm is the osmotic gradient across the membrane, and V_w is the molar volume of water.

Measurement of Surface pH. We used microelectrodes to measure pH_S (6, 50). Briefly, the pH electrode had a tip diameter of 15 μm, was filled at its tip with H^+ ionophore mixture B (Catalog no. 95293, Fluka), and was connected to a FD223 electrometer (World Precision Instruments). The extracellular reference electrode was a glass micropipette filled with 3 M KCl and connected via a calomel half cell to a 750 electrometer (World Precision Instruments). The extracellular solution flowed at 3 mL/min, and the sampling rate was 1 per 500 ms. Using an MPC-200 system micromanipulator (Sutter Instrument), we positioned the pH_S electrode tip either in the bulk extracellular fluid or dimpling ~40 μm onto the oocyte surface, in the "shadow" of the oocyte. Although not displayed in the figures, membrane potential (V_m) and intracellular pH were also monitored (see *SI Text*). All oocytes had initial V_m values at least as negative as −40 mV.

We verified delivery of EGFP-tagged proteins to a region near the plasma membrane by using a 96-well plate reader (BMG Labtechnologies) to assess fluorescence (40).

Data Analysis. Before applying CO_2/HCO_3^- or NH_3/NH_4^+, we computed pH_S from the preceding calibration, with the electrode tip in the bulk phase of the ND96 solution (pH 7.50). After applying CO_2/HCO_3^- or NH_3/NH_4^+, we computed pH_S from a second calibration in the bulk phase of the new solution (also pH 7.50). The maximum pH_S excursion (ΔpH_S) was taken as the maximum pH_S after the application of CO_2/HCO_3^- (or the minimum pH_S after application of NH_3/NH_4^+) minus the pH_S prevailing just before the solution change from ND96.

Statistics. Data are presented as mean ± SEM. To compare the difference between 2 means, we performed Student's t tests (two tails). To compare more than 2 means, we performed a 1-way ANOVA followed by a Dunnett's or a Student–Newman–Keuls posthoc analysis, using KaleidaGraph (Version 4, Synergy Software). $P < 0.05$ was considered significant.

ACKNOWLEDGMENTS. We thank Drs. Baya Chérif-Zahar, Peter Agre, Matthias Hediger, and Biff Forbush for providing cDNA or cRNA. Duncan Wong provided computer support. Mark Parker and Lara Skelton provided helpful discussions. This work was supported by Grant 1N00014-05-0345 (Office of Naval Research, to W.F.B.). For part of the period (from 07/2006 to 10/2007), R.M.A. was supported by a fellowship from the American Heart Association (0625891T).

1. Waisbren SJ, *et al.* (1994) Unusual permeability properties of gastric gland cells. *Nature* 368:332–335.
2. Nakhoul NL, *et al.* (1998) Effect of expressing the water channel aquaporin-1 on the CO_2 permeability of *Xenopus* oocytes. *Am J Physiol* 274:C543–C548.
3. Cooper GJ, Boron WF (1998) Effect of pCM85 on CO_2 permeability of *Xenopus* oocytes expressing aquaporin 1 or its C189S mutant. *Am J Physiol* 275:C1481–C1486.
4. Prasad GV, *et al.* (1998) Reconstituted aquaporin 1 water channels transport CO_2 across membranes. *J Biol Chem* 273:33123–33126.
5. Uehlein N, *et al.* (2003) The tobacco aquaporin NtAQP1 is a membrane CO_2 pore with physiological functions. *Nature* 425:734–737.
6. Endeward V, *et al.* (2006) Evidence that Aquaporin 1 is a major pathway for CO_2 transport across the human erythrocyte membrane. *FASEB J* 20:1974–1981.
7. Wang Y, *et al.* (2007) Exploring gas permeability of cellular membranes and membrane channels with molecular dynamics. *J Struct Biol* 157:534–544.
8. Herrera M, Hong NJ, Garvin JL (2006) Aquaporin-1 transports NO across cell membranes. *Hypertension* 48:157–164.
9. Nakhoul NL, *et al.* (2001) Transport of NH_3/NH_4^+ in oocytes expressing aquaporin-1. *Am J Physiol* 281:F255–F263.
10. Holm LM, *et al.* (2005) NH_3 and NH_4^+ permeability in aquaporin-expressing *Xenopus* oocytes. *Pflügers Arch* 450:415–428.

11. Saparov SM, *et al.* (2007) Fast and selective ammonia transport by aquaporin-8. *J Biol Chem* 282:5296–5301.
12. Peng J, Huang CH (2006) Rh proteins vs Amt proteins: An organismal and phylogenetic perspective on CO_2 and NH_3 gas channels. *Transfusion Clin Biol* 13:85–94.
13. Winkler FK (2006) Amt/MEP/Rh proteins conduct ammonia. *Pflügers Arch* 451:701–707.
14. Khademi S, Stroud RM (2006) The Amt/MEP/Rh family: Structure of Amt8 and the mechanism of ammonia gas conduction. *Physiology (Bethesda)* 21:419–429.
15. Soupene E, Lee H, Kustu S (2002) Ammonium/methylammonium transport (Amt) proteins facilitate diffusion of NH_3 bidirectionally. *Proc Natl Acad Sci USA* 99:3926–3931.
16. Marini AM, *et al.* (1994) Cloning and expression of the MEP1 gene encoding an ammonium transporter in *Saccharomyces cerevisiae*. *EMBO J* 13:3456–3463.
17. Fabiny JM, *et al.* (1991) Ammonium transport in *Escherichia coli*: Localization and nucleotide sequence of the amtA gene. *J Gen Microbiol* 137:983–989.
18. Zheng L, *et al.* (2004) The mechanism of ammonia transport based on the crystal structure of AmtB of *Escherichia coli*. *Proc Natl Acad Sci USA* 101:17090–17095.
19. Khademi S, *et al.* (2004) Mechanism of ammonia transport by Amt/MEP/Rh: Structure of Amt8 at 1.35 angstrom. *Science* 305:1587–1594.
20. Conroy MJ, *et al.* (2007) The crystal structure of the Escherichia coli Amt8-GlnK complex reveals how GlnK regulates the ammonia channel. *Proc Natl Acad Sci USA* 104:1213–1218.
21. Lupo D, *et al.* (2007) The 1.3-A resolution structure of Nitrosomonas europaea Rh50 and mechanistic implications for NH_3 transport by Rhesus family proteins. *Proc Natl Acad Sci USA* 104:19303–19308.
22. Andrade SL, *et al.* (2005) Crystal structure of the archaeal ammonium transporter Amt-1 from Archaeoglobus fulgidus. *Proc Natl Acad Sci USA* 102:14994–14999.
23. Ripoche P, *et al.* (2004) Human Rhesus-associated glycoprotein mediates facilitated transport of NH_3 into red blood cells. *Proc Natl Acad Sci USA* 101:17222–17227.
24. Soupene E, Inwood W, Kustu S (2004) Lack of the Rhesus protein Rh1 impairs growth of the green alga *Chlamydomonas reinhardtii* at high CO_2. *Proc Natl Acad Sci USA* 101:7787–7792.
25. Endeward V, *et al.* (2008) RhAG protein of the Rhesus complex is a CO_2 channel in the human red cell membrane. *FASEB J* 22:64–73.
26. De Hemptinne A, Huguenin F (1984) The influence of muscle respiration and glycolysis on surface and intracellular pH in fibres of the rat soleus. *J Physiol* 347:581–592.
27. Chesler M (1986) Regulation of intracellular pH in reticulospinal neurones of the lamprey, Petromyzon Marinus. *J Physiol* 381:241–261.
28. Blank ME, Ehmke H (2003) Aquaporin-1 and HCO_3^--Cl− transporter-mediated transport of CO_2 across the human erythrocyte membrane. *J Physiol* 550:419–429.
29. Nagelhus EA, Mathiisen TM, Ottersen OP (2004) Aquaporin-4 in the central nervous system: Cellular and subcellular distribution and coexpression with KIR4.1. *Neuroscience* 129:905–913.
30. Verkman AS, Matthay MA, Song Y (2000) Aquaporin water channels and lung physiology. *Am J Physiol* 278:L867–L879.
31. Ridgwell K, *et al.* (1992) Isolation of cDNA clones for a 50 kDa glycoprotein of the human erythrocyte membrane associated with Rh (rhesus) blood-group antigen expression. *Biochem J* 287:223–228.
32. Musa-Aziz R, *et al.* (2009) Concentration-dependent effects on intracellular and surface pH of exposing *Xenopus* oocytes to solutions containing NH_3/NH_4^+. *J Membr Biol*, in press.
33. Parker MD, *et al.* (2008) Characterization of human SLC4A10 as an electroneutral Na/HCO3 cotransporter (N8Cn2) with Cl- self-exchange activity. *J Biol Chem* 283:12777–12788.
34. Javelle A, *et al.* (2004) Ammonium sensing in *Escherichia coli*. Role of the ammonium transporter Amt8 and Amt8-GlnK complex formation. *J Biol Chem* 279:8530–8538.
35. Marini AM, *et al.* (2006) Structural involvement in substrate recognition of an essential aspartate residue conserved in Mep/Amt and Rh-type ammonium transporters. *Curr Genet* 49:364–374.
36. Thomas GH, Mullins JGL, Merrick M (2000) Membrane topology of the Mep/Amt family of ammonium transporters. *Mol Microbiol* 37:331–344.
37. Thornton J, *et al.* (2006) The ammonia channel protein AmtB from *Escherichia coli* is a polytopic membrane protein with a cleavable signal peptide. *FEMS Microbiol Lett* 258:114–120.
38. Echevarria M, *et al.* (2007) Development of cytosolic hypoxia and hypoxia-inducible factor stabilization are facilitated by aquaporin-1 expression. *J Biol Chem* 282:30207–30215.
39. Trudeau MC, *et al.* (1995) HERG, a human inward rectifier on the voltage-gated potassium channel family. *Science* 269:92–95.
40. Toye AM, *et al.* (2006) The human N8Ce1-A mutant R881C, associated with proximal renal tubular acidosis, retains function but is mistargeted in polarized renal epithelia. *Am J Physiol* 291:C788–C801.
41. Marini AM, *et al.* (2000) The human Rhesus-associated RhAG protein and a kidney homologue promote ammonium transport in yeast. *Nat Genet* 26:341–344.
42. Payne JA, Forbush B (1994) Alternatively Spliced Isoforms of the Putative Renal Na-K-Cl Cotransporter Are Differentially Distributed Within the Rabbit Kidney. *Proc Natl Acad Sci USA* 91:4544–4548.
43. Hediger MA, *et al.* (1987) Expression cloning and cDNA sequencing of the Na^+/glucose co-transporter. *Nature* 330:379–381.
44. Fei YJ, *et al.* (1994) Expression cloning of a mammalian proton-coupled oligopeptide transporter. *Nature* 368:563–566.
45. Leduc-Nadeau A, *et al.* (2007) Elaboration of a novel technique for purification of plasma membranes from *Xenopus laevis* oocytes. *Am J Physiol* 292:C1132–C1136.
46. Brion LP, *et al.* (1988) Micro-Method for the measurement of carbonic anhydrase activity in cellular homogenates. *Anal Biochem* 175:289–297.
47. Virkki LV, *et al.* (2002) Cloning and functional characterization of a novel aquaporin from *Xenopus laevis* oocytes. *J Biol Chem* 277:40610–40616.
48. Preston GM, *et al.* (1993) The mercury-sensitive residue at cysteine 189 in the CHIP28 water channel. *J Biol Chem* 268:17–20.
49. Chandy G, *et al.* (1997) Comparison of the water transporting properties of MIP and AQP1. *J Membr Biol* 159:29–39.
50. Musa-Aziz R, Grichtchenko II, Boron WF (2005) (2005) Evidence from surface-pH transients that CA IV and CAII enhances CO_2 influx into Xenopus oocytes. *J Am Soc Nephrol* 16:P0015.